
Effect of Thermal Ageing and Microstructure
on Fracture Mechanical Behaviour of
Ni-based Alloy Dissimilar Metal Welds

Zaiqing Que¹
Noora Hytönen¹
Yanling Ge¹
Sebastian Lindqvist¹
Andrea Fazi²
Mattias Thuvander²
Pål Efsing^{3,4}

¹ VTT Technical Research Centre of Finland Ltd, PO Box 1000
FI-02044 VTT, Espoo, Finland

² Chalmers University of Technology, Department of Physics
SE-412 96 Göteborg, Sweden

³ Ringhals AB, SE-43285 Väröbacka, Sweden

⁴ Department of Solid Mechanics, Royal Institute of Technology (KTH)
SE-100 44 Stockholm, Sweden

Abstract

DMWs are commonly used to join austenitic and ferritic components in the RCPB and can become potential concerns regarding the structural integrity of the nuclear power SSC. In particular, the knowledge on the local strength mismatch at the LAS/nickel-based alloy weld metal interface upon PWHT and during long-term ageing is lacking. The amount of information available in the open literature on the fracture mechanical and microstructural changes occurring at the fusion boundary after buttering, welding, PWHT and long-term ageing is relative limited and often very case dependent. Understanding the fracture mechanical and microstructural appearance, behaviour and development of the complex DMW fusion boundary is crucial for both the improvement of nuclear component integrity and to ensure safe long-term operation. In this study, a Ringhals SA508/Alloy52 DMW mock-up consisting of Alloy 52 buttering on both sides (representative of Ringhals 3 pressurizer surge nozzle DMW) and a TVO NG DMW mock-up are studied, thus the test materials are representative of actual power plant components. The project promotes the knowledge transfer, improve the nuclear materials and fracture mechanics competence and strengthen the connections and experience exchange between the Nordic research organizations, universities, industries, authorities, and especially the young generation. The project deals with the structural integrity, long-term operation, and ageing management, which are relevant for both present and future nuclear power plants. The technical results provide a basis for assessment of long-term operation for the Finnish and Swedish nuclear power plants for both the operators and the regulatory perspectives. Dissemination through the open seminar, the peer reviewed publications and the oral presentations at the international conferences ensured the knowledge exchange in international and Nordic networks.

Key words

Dissimilar metal weld, Alloy 52, fusion boundary, characterisation, fracture mechanical test

NKS-485
ISBN 978-87-7893-581-6
Electronic report, March 2024
NKS Secretariat
P.O. Box 49
DK - 4000 Roskilde, Denmark
Phone +45 4677 4041
www.nks.org
e-mail nks@nks.org

Effect of Thermal Ageing and Microstructure on Fracture Mechanical Behaviour of Ni-based Alloy Dissimilar Metal Welds

Final Report from the NKS-R FEMMA activity (Contract: AFT/NKS-R(23)134/3)

Zaiqing Que¹, Noora Hytönen¹, Yanling Ge¹, Sebastian Lindqvist¹
Andrea Fazi², Mattias Thuvander²
Pål Efsing^{3,4}

¹ VTT Technical Research Centre of Finland Ltd, PO Box 1000, FI-02044 VTT, Espoo, Finland

² Chalmers University of Technology, Department of Physics, SE-412 96, Göteborg, Sweden

³ Ringhals AB, SE-43285 Väröbacka, Sweden

⁴ Department of Solid Mechanics, Royal Institute of Technology (KTH), SE-100 44 Stockholm, Sweden

Table of contents

	Page
1. Introduction	3
2. Microstructural investigations on FBs of DMWs	4
3. Microstructural assessment using APT	6
4. Discussions	7
5. Conclusions	8
6. References	8

1. Introduction

Dissimilar metal welds (DMWs) are commonly used to join austenitic and ferritic components in the reactor coolant pressure boundary, often using a nickel-based filler metal. DMWs can become potential concerns regarding the structural integrity of the nuclear power systems, structures and components. In particular, the knowledge on the local strength mismatch at the low alloy steel (LAS)/nickel-based alloy weld metal interface upon post-weld heat treatment (PWHT) and during long-term ageing is lacking. The amount of information available in the literature on the fracture mechanical and microstructural changes occurring at the fusion boundary (FB) after buttering, welding, PWHT and long-term ageing is relatively limited and often very case dependent. As a part of the NKS-R program in 2023, VTT, Chalmers University of Technology, and KTH have continued to study the microstructural properties and fracture mechanical performance of an Alloy 52 narrow-gap (NG) DMW, provided by TVO, and an Alloy 52 DMW mock-up consisting of Alloy 52 buttering on both sides, provided by Ringhals.

The project deals with the structural integrity, long-term operation, and ageing management, which are relevant for both present and future nuclear power plants. The technical results provide a basis for the assessment of long-term operation for the Finnish and Swedish nuclear power plants for both the operators and the regulatory perspectives. In 2023, the low toughness specimens from 15 000 h thermally aged TVO mock-up have been investigated. These specimens mostly have a crack propagation at 0.3 mm from the fusion boundary in the LAS HAZ. Some detailed fractography and cross sectional microstructure analysis were performed. High-resolution microstructural characterization by means of SEM electron backscatter diffraction (EBSD) have been performed at the heat-affected zone (especially from 0.5 mm towards the fusion boundary). The grain refinement regions are the local brittle zones, which exhibits low fracture toughness. Atom probe tomography (APT) measurements on the as-received and lab thermally aged conditions of TVO mock-up indicates potential phosphorous segregation during thermal aging.

There are active involvements of young scientists in NKS-FEMMA. The work is mainly executed by two recent MSc graduates Timo Veijola and Alekski Vainionpää and two PhD students Noora Hytönen and Laura Sirkiä. Young scientists/postdocs, Sebastian Linqvist, Andrea Fazi and Armin Halilovic and Pedro Ferreiros are the main working group. Additionally, young engineers and researchers at TVO, KTH, Forsmark, STUK, OKG, Ringhals, Chalmers and VTT are following the progress of the work in the project meetings and seminar/workshop organized by NKS-FEMMA. This enables knowledge retention and transfer to the young generation of researchers at all organizations. Developing and maintaining the knowledge of DMW-related issues is vital for the Nordic nuclear power industry. NKS-FEMMA creates a unique opportunity to keep close contacts between researchers and nuclear industry.

NKS-FEMMA project achieves high standard of academic excellence. Two journal articles from NKS-FEMMA project were published in *Materials Characterization* and *Journal of Nuclear Materials* in 2023 (10.1016/j.jnucmat.2023.154558; 10.1016/j.matchar.2023.112880).

2. Microstructural investigations on FBs of DMWs

The microstructural investigations were performed at the LAS/nickel-based alloy weld metal interface. High-magnification microstructural characterization by means of scanning electron microscopy (SEM)/ electron backscatter diffraction (EBSD), focused ion beam (FIB), wide-angle X-ray scattering (WAXS) and transmission electron microscopy (TEM) were performed at the FB region at VTT. The effect of thermal ageing on the carbon enrichment, and the evolution of the local mismatch during the aging were evaluated.

In this work, the microstructure and carbides' crystal structure, chemistry, morphology and size in the LAS FB carbide precipitation zone (CPZ, normally up to 1.5 μm from FB), carbon depletion zone (CDZ, up to 40 – 50 μm from FB) and HAZ (up to 2 mm from FB) were analysed.

The microhardness profiles of HV1 and HV0.3 across the FB in the TVO narrow gap as-received (NG AR) and TVO narrow gap thermally aged (NG TA) samples are shown in Fig. 1. The microhardness peaks are close to the FB of the LAS side in both materials. The HV1 and HV0.3 profiles are rather similar. It is evident that the NG TA material has a higher microhardness peak (~ 20 HV) than the NG AR material and the position of the peak hardness is closer to the FB in the NG TA material.

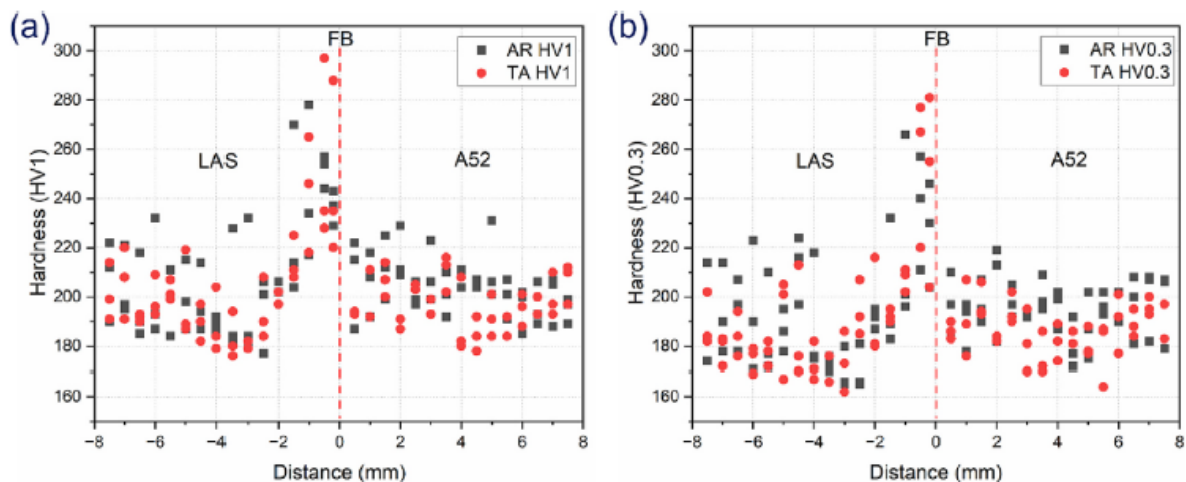


Figure 1: Microhardness profiles of HV1 and HV0.3 across the FB in the NG AR and NG TA samples.

The microstructure and carbide formation at the FB CPZ (0.5–1.5 μm from the FB) were investigated with SEM and TEM. An intensive carbide accumulation area (CPZ) is found in both AR and TA materials due to the high content of the strong carbide-forming element Cr at the FB as shown in Fig. 2. Though the width of the CPZ varies locally along the FB, there is a clear difference in the CPZ width between AR and TA materials. As shown in Fig. 2, the CPZ of the AR and TA materials is up to 500 nm and >1500 nm, respectively. The number of carbides is much lower and the size of the carbides is also smaller in the AR material compared to the TA material. The elemental maps in Fig. 2 reveal that the carbides are (Fe, Cr, Mn) carbides with higher Cr than Mn content. In addition, the NG TA material contains Mo-rich carbides and Cr-rich carbides, which are also found at grain boundaries of Alloy 52.

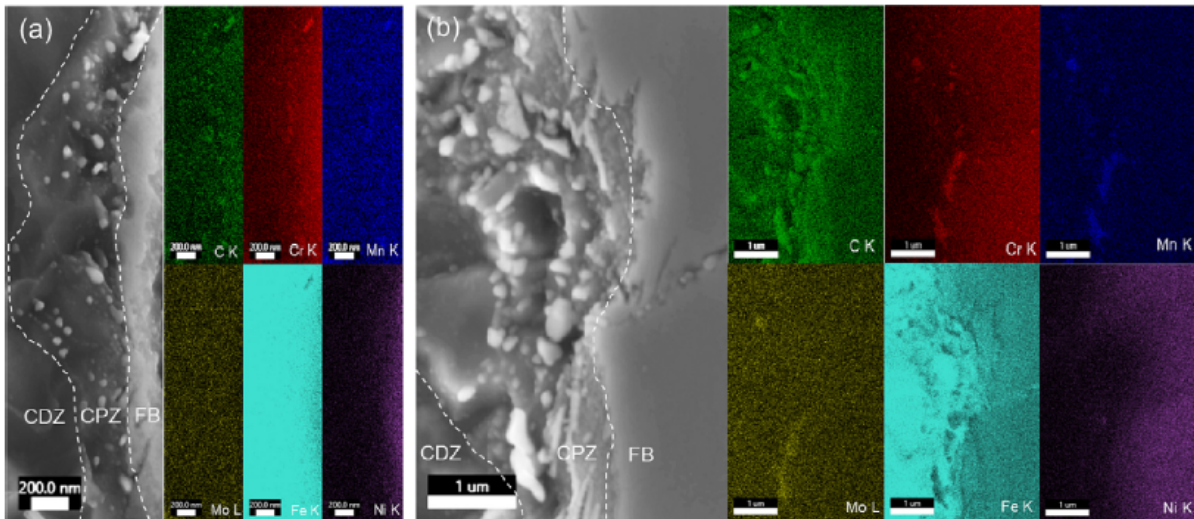


Figure 2. SEM/EDS elemental maps of carbides at the FB of the LAS. (a) NG AR and (b) NG TA.

From the CDZ to the HAZ (outside the CDZ), the carbide population increases dramatically. The microstructure and carbide distribution in the HAZ of the NG AR and the NG TA materials are illustrated in Fig. 3. SEM images show two kinds of grains, i.e. grains with excess carbides and grains lacking apparent carbides. High-resolution TEM reveals that these grains lacking apparent carbides may contain nano-sized carbides. It is worth to note that the fraction of grains devoid of visible carbides in the HAZ is 2–3 times higher in the NG TA material than in the NG AR material. The STEM image of Fig. 3 (d) shows a few long fibre-like carbides aligning in same direction, with the longest one up to 2 μm in length, which is a magnitude longer than in Fig. 3(b). It seems that these long carbides were formed during thermal aging.

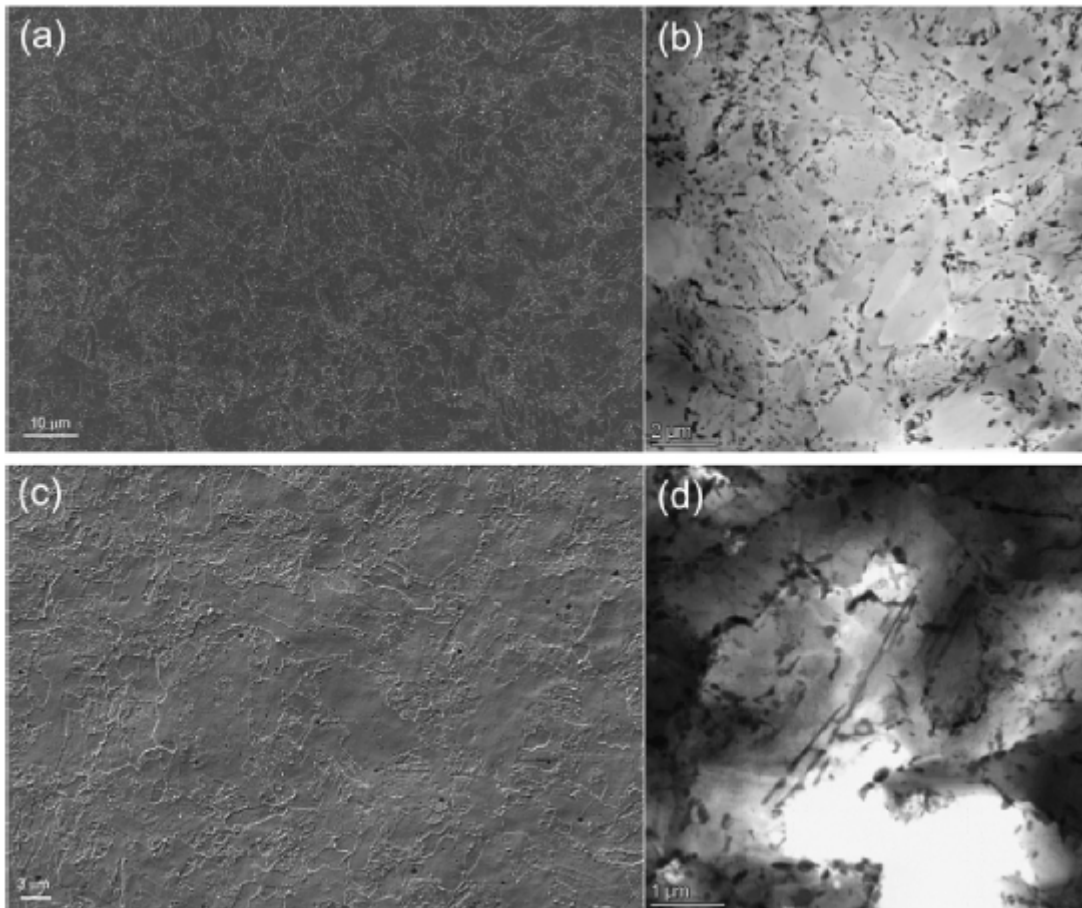


Figure 3. Microstructure and carbide distribution in the HAZ of (a-b) the NG AR and (c-d) the TA material. (a,c) SEM SE images and (b,d) STEM BF images.

3. Microstructural assessment using APT

Atom probe tomography (APT) measurements at Chalmers University of Technology was used to identify the elemental segregation (especially phosphorous) at the boundaries upon ageing, primarily by comparing the phosphorous content of grain boundaries and comparing the non-aged condition to the thermally-aged condition of the TVO mock-up. In Figure 4, representative results of thermally-aged condition are shown. In the non-aged condition, there was no P segregation.

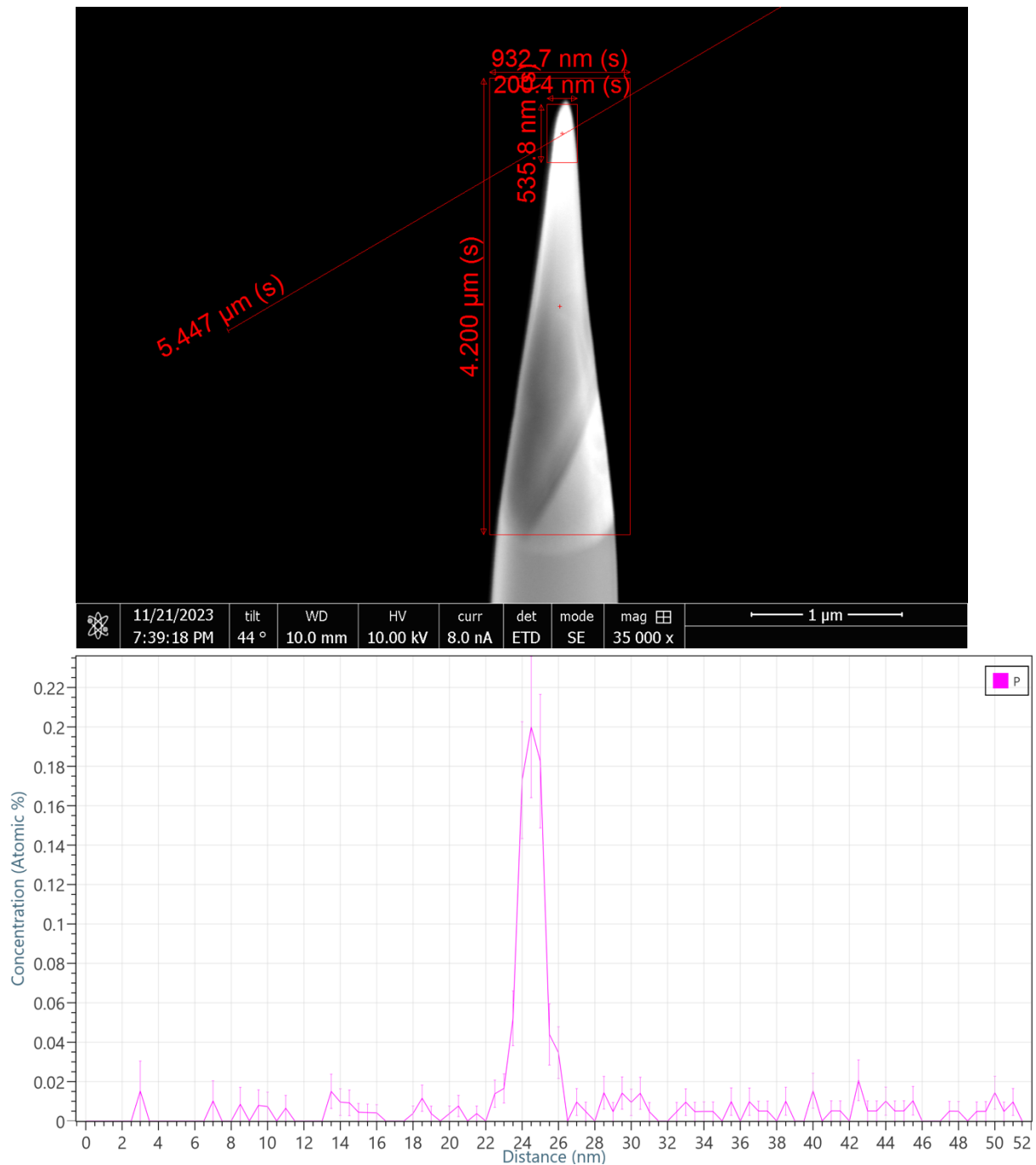


Figure 4. (a) FIB needle for APT analysis containing a grain boundary (b) APT results shows P segregation to grain boundary.

4. Discussions

Long-term thermal aging triples the width of the CPZ. In the CPZ, the number of carbides is much lower and the size of the carbides is also smaller in the AR material than in the TA material. This is in line with the result that the long-term thermal aging increases the microhardness peak close to the FB. Except nano-sized nitrides/carbides at the FB, the dominant carbides in the CPZ are $(\text{Fe}, \text{Cr}, \text{Mn})_3\text{C}$ with size about 50–100 and 100–200 nm in the NG AR and NG TA materials, respectively.

Long-term thermal aging slightly reduces the width of the CDZ. This indicates a continuous diffusion of carbon from the CDZ to the CPZ during thermal aging. Long-term thermal aging coarsens the carbides size in the HAZ (up to a magnitude longer), which corresponds well to the WAXS measurement in the HAZ where higher percentage of carbides was observed in the TA than the AR material. The fraction of carbide-free grains in the HAZ is 2–3 times higher in the NG TA material than in the NG AR material. These grains devoid of visible carbides are formed likely during phase transformation where C partitioning occurred.

As shown in this work, long-term thermal aging leads to moderate changes in the microstructure and carbides in the FB, CPZ, CDZ and HAZ regions in the NG DMW. The peak hardness of the NG DMW was reported to coincide with the position of carbon peak values, which is in line with the microhardness measurement carried out at two different loads and the quantitative analysis of C concentration across the FB by WDS. In this work higher microhardness peak closer to the FB and wider CPZ/narrower CDZ in the TA material were observed.

The APT results suggest that in the studied DMW mock-up with low bulk phosphorus there can be significant phosphorus segregation observed at grain boundary after thermal aging. Therefore, the resultant microstructural changes related to thermal aging are carbides coarsening and P segregation.

5. Conclusions

Long-term thermal aging increases the microhardness peak (~20 HV) close to the FB and triples the width of the CPZ. In the CPZ, the number of carbides is much lower and the size of the carbides is smaller in the AR material than in the TA material.

Long-term thermal aging coarsens the carbide size in the HAZ. The length of the carbide can be a magnitude longer after aging. The fraction of grains devoid of visible carbides in the HAZ is 2–3 times higher in the NG TA material than in the NG AR material.

After thermal aging, the higher microhardness mismatch at the FB, the larger/denser carbides in the CPZ and the coarsened carbides and higher fraction of carbide-free grains in the HAZ may lead to local brittle zones and could cause low fracture toughness.

There is evidence of a significant phosphorus segregation to grain boundaries in HAZ due to thermal aging.

6. References

- Y. Ge, Z. Que, K. Lindgren, H. Noora, M. Thuvander, Effect of thermal aging on microstructure and carbides of SA508/Alloy 52 dissimilar metal weld, *Materials Characterization* 200(2023):112880.
- N. Hytönen, Y. Ge, Z. Que, S. Lindqvist, et al., Study of Fusion Boundary Microstructure and Local Mismatch of SA508/Alloy 52 Dissimilar Metal Weld with Buttering, *Journal of Nuclear Materials* 583(1):154558.
- S. Lindqvist, Z. Que, P. Nevasmaa and N. Hytönen, “The effect of thermal aging on fracture properties of a narrow-gap Alloy 52 dissimilar metal weld,” *Engineering Fracture Mechanics*, 2023, DOI: 10.1016/j.engfracmech.2023.109056.
- Lindqvist, S., Hytönen, N., Sirkiä, L., Arffman, P., Lydman, J., Ge, Y., Nevasmaa, P. & Que, Z., “Fracture in the Ductile-To-Brittle Transition Region of A Narrow-Gap

Alloy 52 and Alloy 52 Dissimilar Metal Weld With Battering,” ASME PVP, Nov 2022, doi: 10.1115/PVP2022-80690.

- N. Hytönen, Y. Ge, Z. Que, S. Lindqvist, J. Lydman, U. Ehrnstén, P. Rautala, I. Virkkunen and P. Efsing, “Effect of Microstructure on Mechanical Behaviour of Ni-base Alloy Dissimilar Metal Welds,” The 20th International Conference on Environmental Degradation of Materials in Nuclear Power Systems-Water Reactor meeting, ED2021-17104. 2022, Colorado, USA.
- N. Hytönen, Z. Que, S. Lindqvist, J. Lydman, Y. Ge, I. Virkkunen, U. Ehrnstén, P. Rautala, P. Efsing, B. Forssgren, Fusion Boundary Microstructure and Fracture Behaviour of a narrow-gap Alloy 52 Dissimilar Metal Weld and an Alloy 52 Dissimilar Metal Weld with Battering, International Symposium Contribution of Materials Investigations and Operating Experience to LWRs’ Safety, Performance and Reliability, FONTEVRAUD 10, September 2022, Avignon, France.

Acknowledgements

NKS conveys its gratitude to all organizations and persons who by means of financial support or contributions in kind have made the work presented in this report possible.

The authors wish to express their gratitude for the funding and support from Ringhals AB, OKG AB, Teollisuuden Voima Oyj and VTT Technical Research Centre of Finland within the FEMMA+ (Forum for the Effect of Thermal Ageing and Microstructure on Mechanical and EAC Behaviour of Ni-based Alloy Dissimilar Metal Welds Plus) research project. The authors also thank NKS for funding the NKS-FEMMA (AFT/NKS-R(23)134/3) project. The authors would like to thank P. Arffman, J. Lydman, A. Nurmela and L. Sirkiä for the experimental contributions. The authors would like to thank U. Ehrnstén, B. Forssgren, H. Reinvall and H. Hänninen for suggestions and discussions.

Disclaimer

The views expressed in this document remain the responsibility of the author(s) and do not necessarily reflect those of NKS. In particular, neither NKS nor any other organisation or body supporting NKS activities can be held responsible for the material presented in this report.

Title	Effect of Thermal Ageing and Microstructure on Fracture Mechanical Behaviour of Ni-based Alloy Dissimilar Metal Welds
Author(s)	Zaiqing Que ¹ , Noora Hytönen ¹ , Yanling Ge ¹ , Sebastian Lindqvist ¹ Andrea Fazi ² , Mattias Thuvander ² Pål Efsing ^{3,4}
Affiliation(s)	¹ VTT Technical Research Centre of Finland Ltd, PO Box 1000, FI-02044 VTT, Espoo, Finland ² Chalmers University of Technology, Department of Physics, SE-412 96, Göteborg, Sweden ³ Ringhals AB, SE-43285 Väröbacka, Sweden ⁴ Department of Solid Mechanics, Royal Institute of Technology (KTH), SE-100 44 Stockholm, Sweden
ISBN	978-87-7893-581-6
Date	March 2024
Project	NKS-R / FEMMA activity (Contract: AFT/NKS-R(23)134/3)
No. of pages	12
No. of tables	0
No. of illustrations	4
No. of references	6
Abstract max. 2000 characters	DMWs are commonly used to join austenitic and ferritic components in the RCPB and can become potential concerns regarding the structural integrity of the nuclear power SSC. In particular, the knowledge on the local strength mismatch at the LAS/nickel-based alloy weld metal interface upon PWHT and during long-term ageing is lacking. The amount of information available in the open literature on the fracture mechanical and microstructural changes occurring at the fusion boundary after buttering, welding, PWHT and long-term ageing is relative limited and often very case dependent. Understanding the fracture mechanical and microstructural appearance, behaviour and development of the complex DMW fusion boundary is crucial for both the improvement of nuclear component integrity and to ensure safe long-term operation. In this study, a Ringhals SA508/Alloy52 DMW mock-up consisting of Alloy 52 buttering on both sides (representative of Ringhals 3 pressurizer surge nozzle DMW) and a TVO NG DMW mock-up are studied, thus the test materials are representative of actual power plant components. The project promotes the knowledge transfer, improve the nuclear materials and fracture mechanics competence and strengthen the connections and experience exchange between the Nordic research organizations, universities, industries, authorities, and especially the young generation. The project deals with the structural integrity, long-term operation, and ageing management, which are relevant for both present and future

nuclear power plants. The technical results provide a basis for assessment of long-term operation for the Finnish and Swedish nuclear power plants for both the operators and the regulatory perspectives. Dissemination through the open seminar, the peer reviewed publications and the oral presentations at the international conferences ensured the knowledge exchange in international and Nordic networks.

Key words

Dissimilar metal weld, Alloy 52, fusion boundary, characterisation, fracture mechanical test



Contents lists available at ScienceDirect

Journal of Nuclear Materials

journal homepage: www.elsevier.com/locate/jnucmat

Study of fusion boundary microstructure and local mismatch of SA508/ alloy 52 dissimilar metal weld with buttering

N. Hytönen^a, Y. Ge^a, Z. Que^{a,*}, S. Lindqvist^a, P. Nevasmaa^a, I. Virkkunen^b, P. Efsing^{c,d}

^a Nuclear Reactor Materials, VTT Technical Research Centre of Finland, Kivimiehentie 3 FI-02044 VTT, Finland

^b Department of Mechanical Engineering, School of Engineering, Aalto University, Espoo 02150, Finland

^c Ringhals AB, Våröbacka 435 85, Sweden

^d Department of Solid Mechanics, Royal Institute of Technology (KTH), Stockholm SE-100 44, Sweden

H I G H L I G H T

- Double-sided buttered A52 dissimilar metal weld (DMW)
- First of a kind in Europe and representative of real nuclear component
- The fusion boundaries (FBs) of SA508/Alloy 52 buttering were investigated
- Crystal structure, microstructure, elemental diffusion and hardness were correlated
- The FB types affect the local strength mismatch and brittle fracture crack path

A R T I C L E I N F O

Keywords:

Dissimilar metal weld
Alloy 52
Fusion boundary
Characterization
Buttering

A B S T R A C T

A SA508/Alloy 52 dissimilar metal weld (DMW) mock-up with double-sided Alloy 52 butterings, which is fully representative of Ringhals pressurizer surge nozzle DMW repair solution, was studied. The microstructure, crystal structure, elemental diffusion, carbide formation and macro-, micro- and nano-hardness of the SA508/nickel-base Alloy 52 buttering fusion boundary (FB) were investigated. Three types of FBs were analyzed, *i.e.*, narrow FB (~80–85% of whole FB), tempered martensitic transition region (~15%) and wide partially mixed zone (~1–2%). The different FB types were induced by the local heat flow and respective elementary diffusion, which significantly influence the local hardness mismatch across the DMW interface and the local brittle fracture behavior.

1. Introduction

Dissimilar metal welds (DMWs) are commonly used for joining austenitic and ferritic components in the reactor coolant pressure boundary, typically using a nickel-based filler metal [1]. However, due to the difference in crystal structure between body-centered cubic (BCC) bainitic reactor pressure vessel steel and face-centered cubic (FCC) austenitic weld metal, a crystallographic mismatch occurs at the fusion boundary (FB) and creates a significant chemical composition gradient, particularly in carbon and chromium, at the dissimilar metal interface. As a result, a complex microstructure and a physical and mechanical properties mismatch (*e.g.* corrosion and strength) form at the interface [2–4]. Furthermore, the dissimilarity of metal at the FB can cause residual stresses due to the thermal mismatch during weld solidification

and subsequent cooling [5]. The complex DMW interface contains various microstructural regions including heat-affected zone (HAZ), carbon-depleted zone (CDZ), carbon build-up area at FB, partially-mixed zone (PMZ) and carbide precipitation zone [6,7].

DMWs can pose potential risks to the structural integrity of the nuclear power systems, structures and components [8–10]. However, information on the microstructural and fracture mechanical changes that occur at the FB following buttering, welding, and post-weld heat treatment (PWHT) is limited and highly dependent on individual cases [11]. In particular, knowledge about the local strength mismatch at the interface between low alloy steel (LAS) and Ni-based alloy weld metal during PWHT and long-term aging is lacking [7,12]. Accurately characterizing the local mechanical behaviors of the different materials constituting the DMW is challenging [13,14]. As such, the influence of

* Corresponding author.

E-mail address: zaiqing.que@vtt.fi (Z. Que).

<https://doi.org/10.1016/j.jnucmat.2023.154558>

Received 15 January 2023; Received in revised form 2 April 2023; Accepted 2 June 2023

Available online 3 June 2023

0022-3115/© 2023 The Author(s). Published by Elsevier B.V. This is an open access article under the CC BY license (<http://creativecommons.org/licenses/by/4.0/>).

FB microstructure on DMW performance has become an increasingly important topic in the nuclear power community [14–16].

Despite numerous studies conducted, several critical questions remain unanswered. The two-sided Alloy 52 buttering welding technique, followed by PWHT, exhibits different microstructures at the weld FBs compared to other welding techniques, such as narrow-gap (NG) weld without buttering [17–19]. Limited data are available regarding the behavior of DMWs manufactured using high-Cr Ni-based Alloy 52 weld metal [20], which replaces the earlier used Alloy 182/82 weld metals based on wrought Alloy 600 composition [15]. Although Alloy 52 has higher resistance to environmentally-assisted cracking (EAC) than Alloy 182 [21], the electrochemical potential gap and the resultant galvanic corrosion susceptibility of Alloy 52/LAS is higher than that of Alloy 182/LAS [22]. It is critical to understand the effect of welding techniques and materials on the detailed microstructures at the FBs and local mechanical properties for assessing and enhancing nuclear component integrity and developing repair welding solutions to ensure safe long-term operation of nuclear power plants (NPPs) [23,24]. Furthermore, the segregation of impurity elements during heat treatment and aging, such as phosphorus segregation in the HAZ [18,25], and carbide diffusion to the type-II boundaries, coupled with residual stresses and strains at the interface, are known to increase susceptibility to cracking and stress corrosion cracking (SCC) [26,27]. The roles played by FB structures and types in promoting or reducing weld-related cracking are yet to be fully understood [28].

The welding techniques and parameters utilized in DMW studies in most research programs differ from those employed in actual NPPs, which can lead to significant variations in microstructure and mechanical properties [29,30]. Thus, a comprehensive investigation into the microstructure of the FB and the local mismatch of NPP-relevant DMW mock-ups is necessary. In this study, a Ringhals SA508/Alloy 52 DMW mock-up consisting of Alloy 52 buttering on both sides of an Alloy 52 V-groove weld was studied, which fully represents a repair technology solution of actual NPP components. The two-sided Alloy 52 buttering

welding technique applied was first of a kind in Europe. The FB of SA508/Alloy 52 buttering is the most critical component for the DMW's integrity, and therefore, it was the focus of this work. The microstructure, crystal structure, carbide evolution, elemental diffusion and macro-, micro- and nano-hardness of the bainitic SA508/austenitic Ni-base Alloy 52 buttering FB were investigated. The findings are crucial for comprehending the fracture mechanical behavior and cracking susceptibility of DMWs.

2. Experimental methods and materials

2.1. Materials

The DMW investigated is a mock-up provided by Ringhals (representative of Ringhals 3 pressurizer surge nozzle DMW repair solution), consisting of nozzle material SA508M Grade 2 Class 1, Ni-based Alloy 52 buttering weld, Alloy 52 V-groove weld, Alloy 52 buttering weld, joined to the austenitic stainless steel 316LN safe-end. The inner surface of the nozzle LAS is clad with stainless steel 308 L. A diagram of the DMW structure is presented in Fig. 1. The LAS side with buttering weld was subjected to PWHT at 615 °C for 1 hour and 17 min with heating and cooling rates of 55 °C/h from 300 °C. The V-groove weld and stainless steel side buttering were performed in a work-shop afterwards. The buttering welds were made in a transverse orientation, while the V-groove weld in a longitudinal orientation. The welding parameters are listed in Table 1. The chemical compositions of each material in the DMW were confirmed with glow-discharge optical emission spectroscopy (GD-OES) and are presented in Table 2.

2.2. Microstructural characterization

The metallographic microstructure was evaluated using light optical microscopy (LOM) after etching the specimen. The LAS was etched with Nital 3% and the Alloy 52 with aqua regia (HNO₃ + HCl + glycerol). The

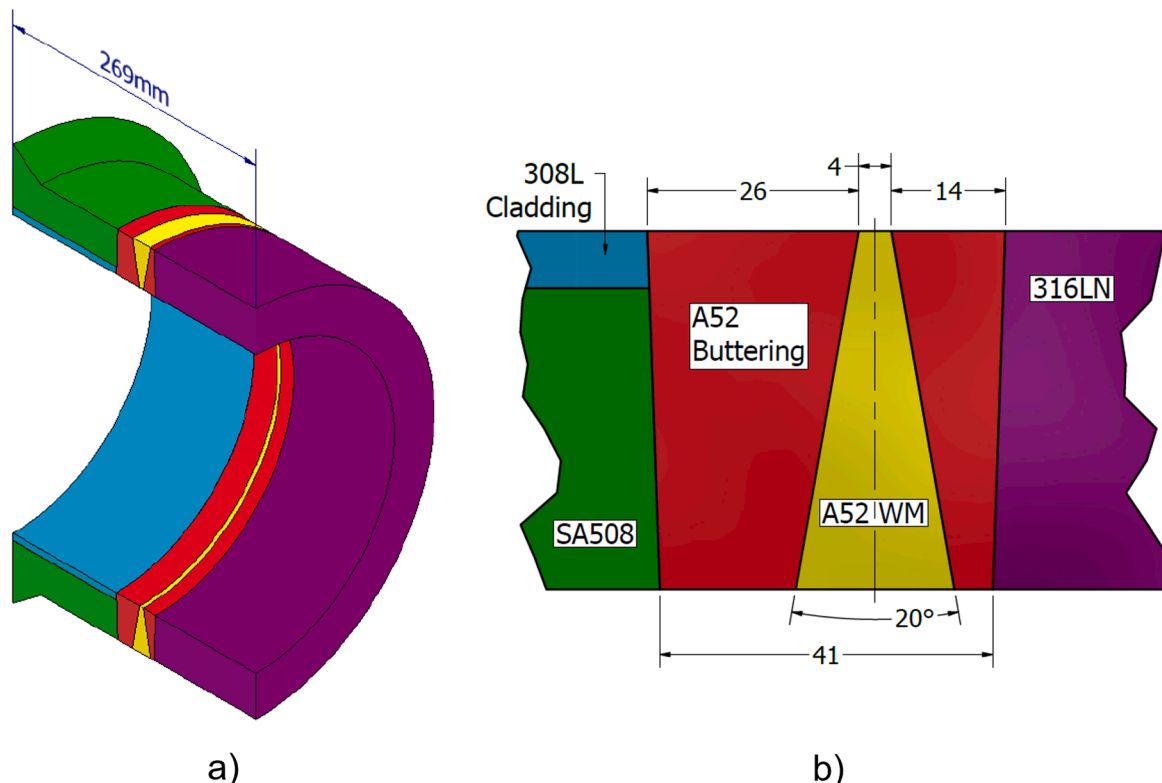


Fig. 1. The illustrative figure showing (a) the location of the weld in the surge nozzle safe-end and (b) the DMW structure. All dimensions are in millimeters.

Table 1
Welding parameters for the investigated DMW.

Welding process	Mechanized Gas Tungsten Arc Welding
Welding position	"Horizontal" - PC
Wire diameter	0.9 mm
Shielding gas	Argon
Type of current	DC
Interpass temperature (max)	100 °C
Heat input	0.67–1.49 kJ/mm

specimens for electron microscopy, nanoindentation and X-ray diffraction (XRD) measurement were mechanically polished with diamond suspension to 0.25 μm, followed by a final surface finish prepared with Buehler VibroMet vibratory polisher machine using MasterMet 2 non-crystallizing amorphous 0.02 μm colloidal silica suspension for 45 min.

Scanning electron microscope (SEM), electron backscatter diffraction (EBSD) and energy dispersive X-ray spectroscopy (EDS) were applied for microstructural characterization of the FBs. A Zeiss Crossbeam 540 equipped with a solid-state four-quadrant backscatter detector (BSD) and an EDAX Hikari Plus EBSD detector was used. The near-surface FB microstructure was investigated using SEM secondary electrons (SE) and backscattered electrons (BSE) imaging techniques. BSE imaging was conducted at an acceleration voltage of 15 keV with a working distance (WD) of 6–7 mm and a probe current 1.5–3.0 nA. EBSD mapping was conducted at an acceleration voltage of 15 keV and a WD of 13–15 mm with 70° tilting and a probe current of 1.5 nA. The EBSD phase maps, inverse polar figures (IPF), Kernel average misorientation (KAM) maps by TSL OIM Analysis 8 software. To reduce the interaction volume between incident electrons and matrix, the EDS line scan with an accelerating voltage of 5 keV and a probe current of 1.5 nA was applied to obtain local chemical differences across the FB from LAS to the weld with a measurement step size of 200 nm.

Transmission electron microscope (TEM) was used to characterize

Table 2

Chemical composition of the LAS nozzle and Ni-based weld metals materials provided by Ringhals. The GD-OES analysis was applied to verify the chemical compositions in SA508 and Alloy 52 buttering weld.

	wt%													
SA508M Gr.2 Cl1	C	Cr	Mo	Ni	Mn	Si	P	S	Al	Ti	Cu	V	Fe	
Nozzle	0.20	0.35	0.63	0.87	0.91	0.23	0.008	0.004	0.019	–	0.05	0.01	Bal.	
GD-OES	0.23	0.36	0.75	0.93	0.98	0.25	0.015	0.004	–	0.002	0.05	0.009	96.4	
Alloy 52	C	Cr	Mo	Ni	Mn	Si	P	S	Al	Ti	Cu	Nb+Ta	Fe	
Buttering	0.029	28.94	<0.01	Bal.	0.29	0.16	<0.003	<0.0005	0.73	0.5	<0.1	<0.002	9.2	
GD-OES	0.034	30.24	<0.02	57.0	0.37	0.15	<0.003	<0.0005	0.79	0.7	<0.2	–	10.6	

the carbides. The specimen was cut by electrical discharge machining (EDM) to a thickness of ~0.5 mm and mechanically thinned to ~100 μm. The final thinning was carried out by twin jet electropolishing using a Struers TenuPol-5 electropolisher with an environmentally friendly salt-based electrolyte. The electrolyte consists of 1 M concentration of NaCl in ethylene glycol and 200 ml ethanol. Scanning TEM (STEM) high-angle annular dark-field (HAADF) and bright-field (BF) images and chemical information of carbides were acquired on FEI Talos F200X STEM equipped with Super-X EDS system operating at 200 kV.

2.3. Macro-, micro- and nano-hardness measurements

A representative DMW cross-sectional specimen was prepared with EDM and polished to 0.25 μm finish for the macro- and micro-hardness measurements. After the hardness measurement, the specimen was etched to reveal the microstructure and indent locations in the DMW (Fig. 2). The Vickers macro- and micro-hardness measurements with loads of 10 kg (HV10), 1 kg (HV1) and 0.3 kg (HV0.3) across the FB were performed, using Struers DuraScan-80 hardness measurement device. The indentation spacing of HV10 was 0.75 mm in the HAZ and region close to the FB, and 2 mm in other regions. The indentation spacing of HV1 and HV0.3 was maintained at 0.5 mm. As shown in Fig. 2, four lines of HV10 were measured and indicated as L1, L2, L3, and L4. L1 was closest to the outer surface, L2 was closest to the inner surface with the cladding, L3 was in the middle of the wall thickness, and L4 below the cladding HAZ characterizing the near inner surface hardness across the SA508/Alloy 52 FB. HV1 and HV0.3 were measured across the FB in the middle of the wall thickness, adjacent to the HV10 L3 measurement line.

Nanoindentation maps were measured with Anton Paar UNHT, using a Berkovich diamond tip indenter. The detailed parameters for nanoindentation are given in Table 3. The nanoindentation mappings encompass a distance of ~120 μm in the SA508 side (over the CDZ) and ~50 μm in the Alloy 52 buttering side, as measured from the FB. The

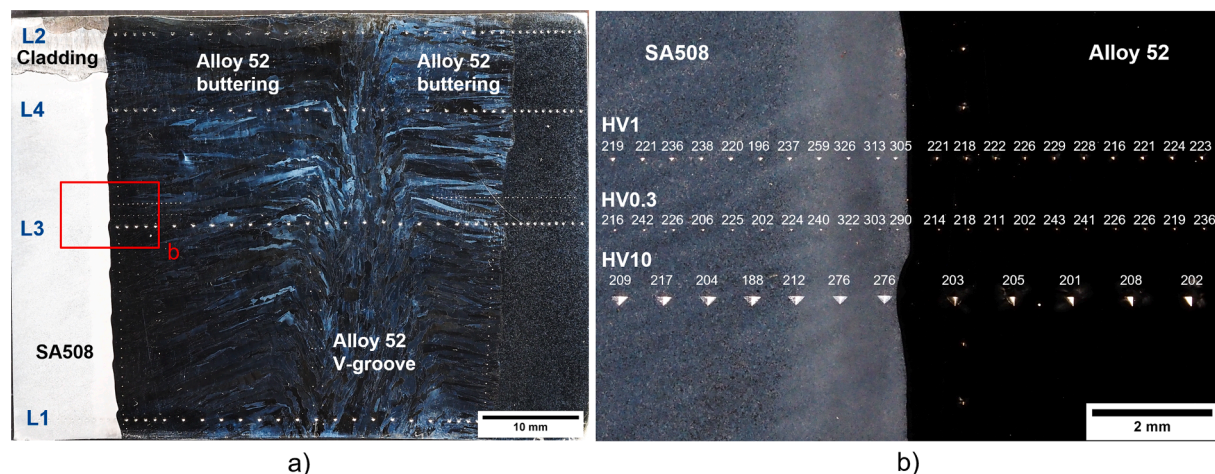


Fig. 2. (a) Macrostructure of the etched DMW and HV10 macro-hardness measurement lines L1-L4. (b) The micro-hardness measurement lines HV1 and HV0.3 in the middle of the wall thickness of DMW (next to the HV10 L3 line).

Table 3
Nanoindentation measurement parameters.

Constant load	1.5 mN (max load)
Loading rate	7.5 mN/min
Step size	5 μm / 2.5 μm
Average indent depth (h _m)	~101 nm

step size in the vicinity of the FB is 2.5 μm, while it is 5 μm in the remaining mapping area. The line spacing is consistently 5 μm.

2.4. XRD measurements

The different phases present in the FB region, *i.e.*, BCC SA508, FCC Alloy 52 and BCC tempered martensite, were studied with XRD. A set of high-resolution reciprocal space maps (RSM) was collected from LAS to Ni-based alloy across the FB with Rigaku SmartLab diffractometer. The parallel beam size of about 200–250 μm was used with a 0.2 mm collimator on the incident beam and a two-dimensional (2D) detector without optics on the diffracted beam path.

In addition, wide-angle X-ray scattering (WAXS) was performed with a Xenoxs Xéuss 3.0 system. Selected TEM foils were also studied with WAXS in transmission mode with a Mo tube of 300 μm beam size. The 2D WAXS patterns were integrated and converted into 1D profiles, which were further refined using the MAUD program.

3. Results

3.1. DMW macro- and microstructure

The macrostructure of the entire DMW is shown in Fig. 2 displays the macrostructure of the entire, where the LAS, cladding, buttering and V-groove welds are indicated. Hardness measurements reveal variations in microstructural features across the FB from weld to HAZ, the LAS matrix and stainless steel cladding. Fig. 3(a) presents macro-hardness measurements (HV10) using four lines, namely L1-L4, as indicated in Fig. 2 (a). The L2 line, which is the closest to the inner surface, exhibits the hardness profile across the FB of stainless steel cladding/Alloy 52, showing only a slight increase in hardness adjacent to the FB. The macro-hardness across the FB of SA508/Alloy 52 buttering is measured by L1, L3 and L4. The hardness peak with a value of ~280 HV10 is found in the HAZ adjacent to the FB on the SA508 side. Beyond ~2.5 mm from the FB in the SA508 side, the macro-hardness is relatively uniform at an average of ~210 HV10. On the weld side, the macro-hardness values

decrease until 1–2 mm from the FB. The macro-hardness in the buttering weld is comparable to that of the SA508 side but with a higher scatter due to the microstructure of the buttering weld beads. The hardness curves in the weld side between lines L1 and L2-L4 differ significantly, with the hardness curve near the outer surface showing an almost opposite trend of macro-hardness compared to the hardness in the mid-thickness or near the inner surface. The deviation in the hardness curves in the weld indicates the presence of internal strains in the V-groove root (L2) and buttering root (L1).

Fig. 3(b) displays the micro-hardness profiles of HV1 and HV0.3. The micro-hardness indents are located in the middle of the wall thickness across the FB of SA508/Alloy 52 buttering, as indicated in Fig. 2(b). The profiles exhibit micro-hardness peaks (320 HV1/HV0.3) in the HAZ approximately 1 mm from the FB. At a greater distance from the FB, the micro-hardness remains relatively constant (~220 HV1/HV0.3) for both SA508 and Alloy 52. The micro-hardness measurements suggest that the SA508 HAZ extends approximately 2 mm in width.

The microstructure of the FB of SA508/Alloy 52 buttering and its surrounding regions on both sides was investigated with the etched metallographic specimen. As shown in Fig. 4(a), the HAZ appears as a dark region adjacent to the FB, while ghost lines are visible as dark lines distributed throughout the bainitic SA508 material. The macro- and micro-hardness measurements indicate that the degree of macro-segregation is mild, as the ghost lines do not cause any significant macroscale deviation in the hardness values. Furthermore, the HAZ width is estimated to be approximately 2.3 mm, which is consistent with the hardness measurement results. Another etching solution was used to study the weld microstructure, specifically the weld beads in the buttering orientation, as shown in Fig. 4(b). The austenitic Ni-grains exhibit dendritic substructure and grow transversely across the weld beads. These grains are decorated with darker vertical micro-segregation areas at the intersection of the weld beads.

3.2. FB types

The microstructure of the SA508/Alloy 52 buttering FB was investigated using LOM (with SA508 side being etched) and SEM-BSE. Three different types of FB microstructures were identified, *i.e.*, i) narrow FB, ii) tempered martensitic transition region and iii) wide PMZ, as shown in Fig. 5. The SEM-BSE analysis covered approximately 18 mm of FB where the majority of the FB was found to be narrow without any distinctive microstructure (Fig. 5(a-b)), which was defined as type-A and occupied ~80–85% of the FB. The type-A boundary area was narrow (<1 μm wide), where the microstructure changes from BCC to FCC without any

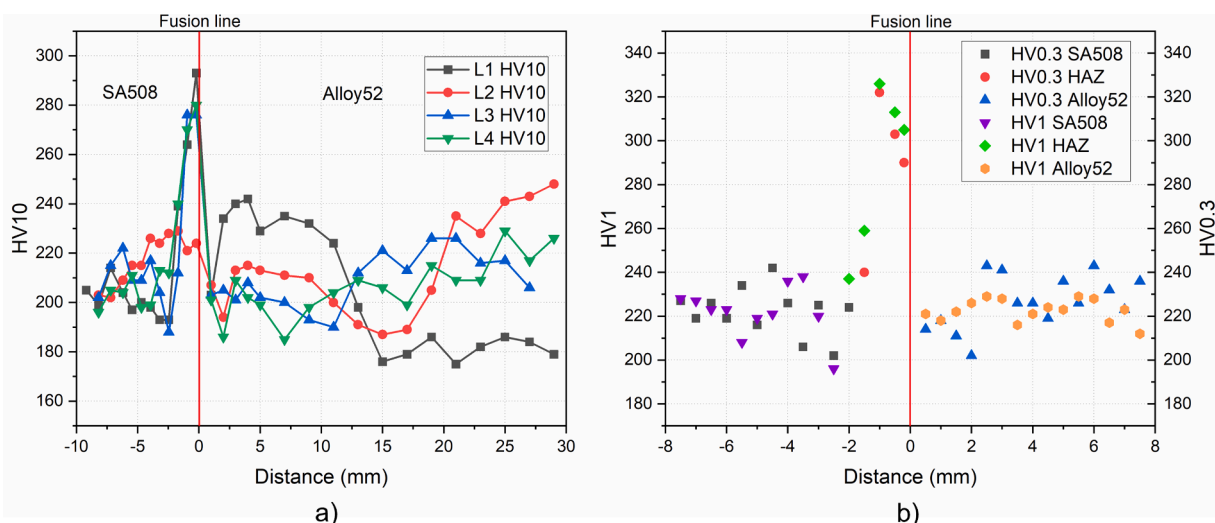


Fig. 3. (a) Macro-hardness HV10 results across the FB from the measurement lines L1-L4. (b) Micro-hardness HV1 and HV0.3 results across the FB.

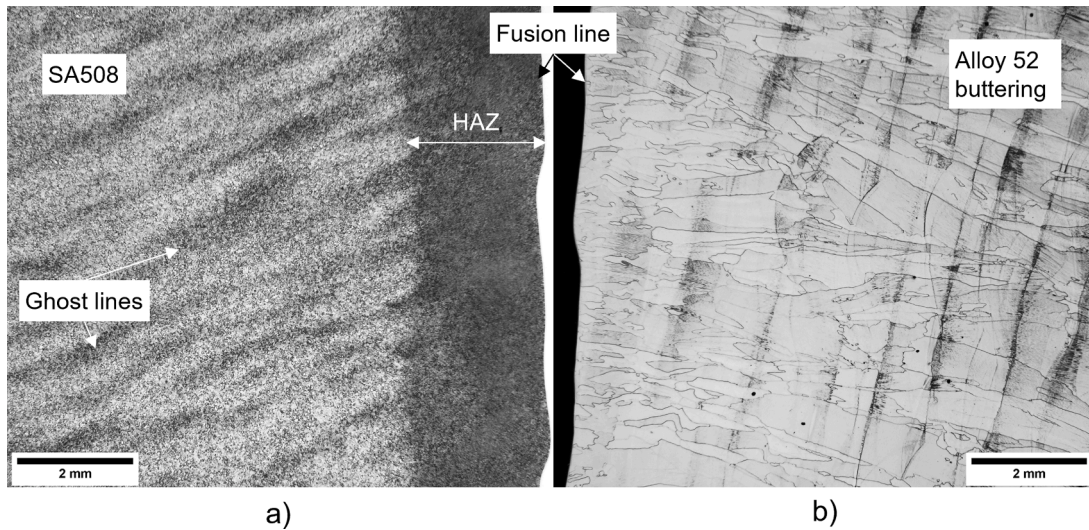


Fig. 4. Etched metallographic specimens showing (a) microstructure of the HAZ and ghost lines in SA508 and (b) weld beads of the Alloy 52 buttering weld.

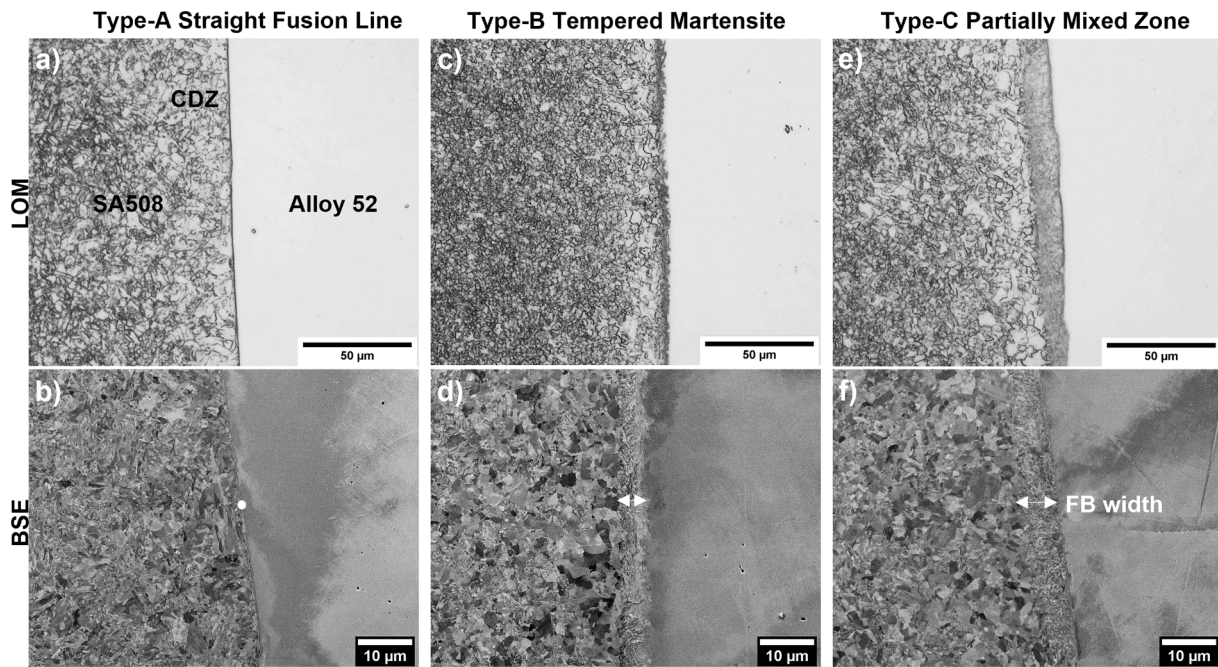


Fig. 5. Three types of FB microstructures (a-b) type-A straight FB, (c-d) type-B tempered martensite and (e-f) type-C PMZ. CDZ width appear more light color adjacent to the FB in (a, b, c) optical images and FB widths are marked in (b, d, f) SEM-BSE images.

visible distinctive transition zone. The second most common boundary type observed was the feathery-like tempered martensitic microstructure, defined as type-B, which had a width of up to $\sim 8 \mu\text{m}$ (Fig. 5(c, d)) and occupied up to $\sim 15\%$ of the FB. In optical imaging, the type-B FB appeared as a dark region with fine lath-like acicular microstructure and the weld side interface was not very distinct due to the lath-like microstructure at the FB. The third FB microstructure type was the wide PMZ (Fig. 5(e, f)), which had a width of up to $\sim 25 \mu\text{m}$ and was the least common, found only at a few locations. It was defined as type-C, occupying only $\sim 1\text{--}2\%$ of the FB. The type-C FB region appeared light in color under LOM and there was a distinct and well-defined boundary for the transition zone, which was different from the type-B FB. As shown in Fig. 5, the three types of FBs appeared to associate with different levels of grain coarsening and widths of CDZ in the LAS HAZ, indicating a difference in the local heat flow and elemental diffusion

between the FB types. The CDZ and grain size evolution adjacent to the FB were illustrated in Fig. 6. The carbon depletion appeared as empty ferrite grains in the coarse-grained region with a relatively small grain size of $\sim 4 \mu\text{m}$. The CDZ width is approximately $30 \mu\text{m}$ at the location of a type-A FB. Beyond the CDZ, the grain size decreased towards $\sim 1 \mu\text{m}$ size and the carbide content increased.

The present study focuses on investigating the specific features of type-B and type-C FBs, which are believed to cause local changes in properties and play a crucial role in maintaining the integrity of DMWs. In order to explore the microstructures of these FBs, various analytical techniques such as SEM-BSE imaging, EBSD, EDS, nanoindentation and XRD analysis were employed. Nanoindentation mappings were performed to reveal the influence of FB types B and C on the nano-hardness mismatch across the local DMW interfaces. The nano-hardness mapping and statistical data points with the average value are shown in Fig. 7.

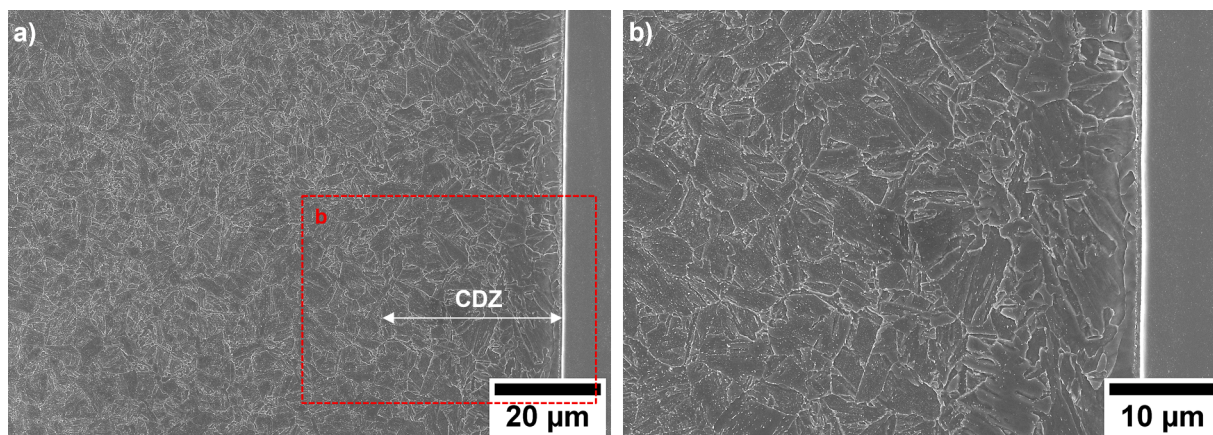


Fig. 6. (a) HAZ and (b) CDZ at a type-A FB. The grain size is $\sim 4 \mu\text{m}$ adjacent to the FB with carbon depletion. From $\sim 30 \mu\text{m}$ from the FB beyond the CDZ, the grain size decreases closer to $\sim 1 \mu\text{m}$.

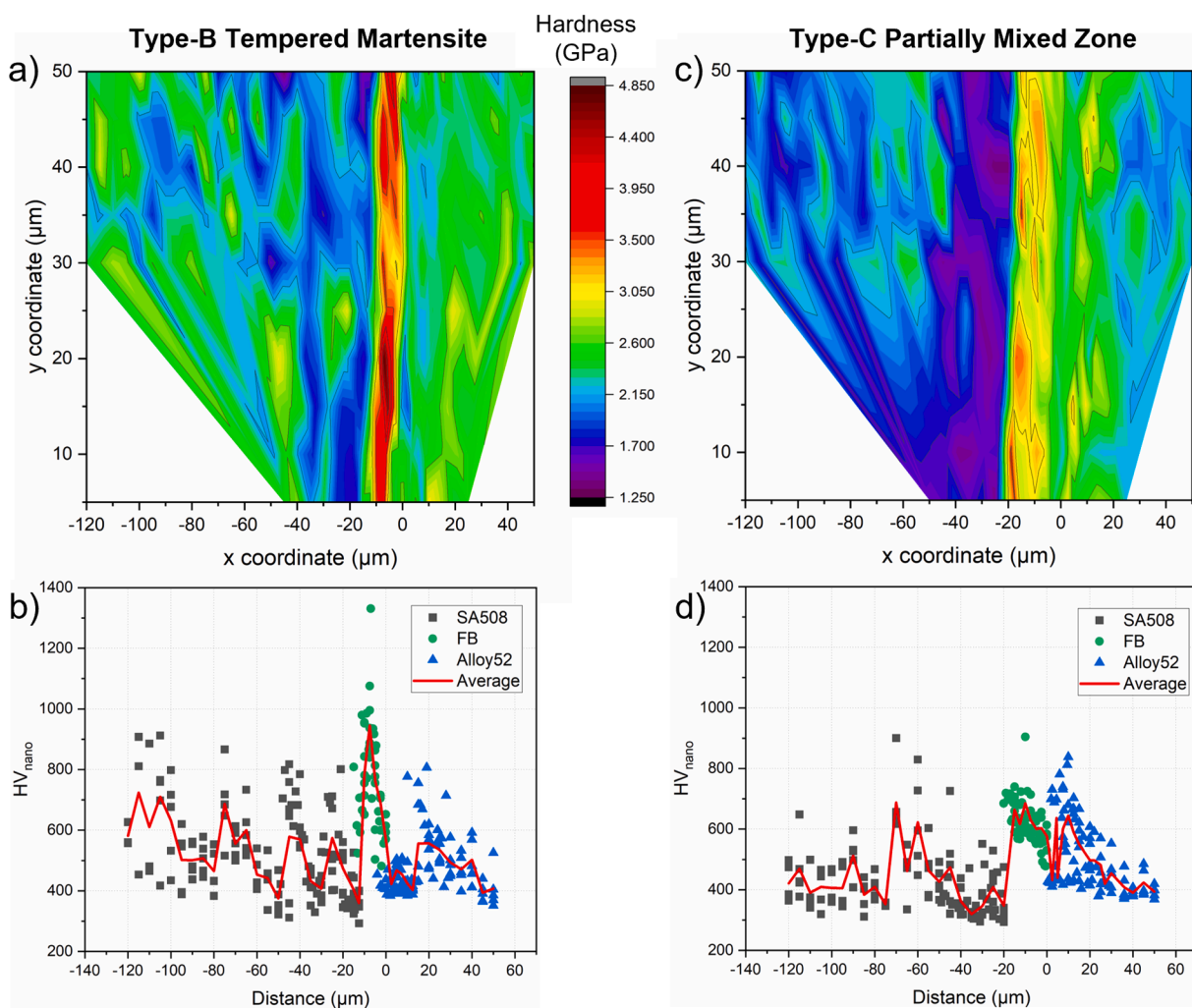


Fig. 7. Nanoindentation results for the (a-b) type-B tempered martensite and (c-d) type-C PMZ FBs. The type-B tempered martensite FB exhibits a nano-hardness peak in the FB.

The mappings in Fig. 7(a,c) visually illustrate the variations in the properties across the two different FBs. The nanoindentation data revealed a conspicuous peak in the nano-hardness at the type-B FB area. The adjacent LAS side to the FB, however, did not show any significant softening due to carbon depletion. In the type-C FB, only a mild nano-

hardness peak was observed for the PMZ FB, which appeared higher due to the contrast to the lower hardness level of the LAS side region adjacent to the FB. This $\sim 30 \mu\text{m}$ region with low nano-hardness in the LAS is identified as CDZ. The overall hardness level for the type-C FB appeared lower with less scatter in Fig. 7(d) compared to the type-B FB

in Fig. 7(b). Contradictorily, a low bound nano-hardness region of ~ 10 μm was observed on the Alloy 52 buttering side in the type-B FB in Fig. 7(b), which was not observed in the type-C FB in Fig. 7(d).

SEM-BSE, EBSD and EDS were applied to analyze the microstructures of the nano-indented regions of types B and C FB. The BSE images in Figs. 8(a–c) and 9(a–c) reveal the microstructures of the type-B and the type-C boundaries, respectively. The corresponding EBSD maps, including the IPF map and phase map with high-angle grain boundaries (15° – 62.7°) and KAM analysis, are shown in Figs. 8(d–f) and 9(d–f). The type-B boundary, with a width of 8 μm , exhibited a lath-like acicular grain microstructure. The laths, with a length of 2–8 μm and a diameter of 200–600 nm, grew towards the weld buttering in the heat flow direction, presumably starting from the favorably oriented fine grains at the bainitic HAZ. The interface between type-B FB and the Alloy 52 buttering weld metal was characterized by a wavy, feathery-like boundary. The type-B FB was dominated by the BCC phase in the phase map and the feathery-like structure was associated with tempered martensitic microstructure. The type-C PMZ FB in Fig. 9 exhibited a straight FB to the Alloy 52 buttering weld metal but with a distinct region of mixed phases of BCC and FCC in the transition region, which was approximately 25 μm wide.

A semi-quantitative analysis of the chemical composition using EDS line scan was conducted across the type-B and the type-C FBs. The location of the line scans was identified in the Figs. 8(a) and 9(a) for the type-B and the type-C FBs, respectively. The EDS results displayed in Fig. 10 indicate the profiles of the major alloy elements of Fe, Ni, Cr and Mn. An increase in Fe content and a decrease in Ni and Cr contents were observed closer to the FB, leading to the formation of a dilution zone from the buttering weld metal side to the FB. The change in the chemical composition across the type-B tempered martensite FB exhibited an almost linear profile for Fe and Ni concentrations, which are the primary constituents of SA508 and Alloy 52, respectively. In contrast, a drastic change in the concentrations of alloying elements was observed from SA508 to PMZ and from PMZ to Alloy 52 with sharp changes in the profile across the type-C FB. The chemical composition of the alloying elements within the type-C PMZ was found to be nearly constant, with approximately 75 wt% of Fe, 15 wt% of Ni and 5 wt% of Cr.

The tempered martensite FB and the surrounding area as depicted in

Fig. 8 were studied using high-resolution XRD with a fine beam size of 200–250 μm , aiming to verify the existence of tempered martensitic phase and determine its crystal structure, *i.e.*, whether it is BCC or body-centered tetragonal (BCT). By measuring from the fully BCC area (LAS) to the fully FCC area (weld metal), the FB was located by reaching 50% BCC of the strongest peak intensity. The first RSM at the FB in Fig. 11(a) revealed two prominent BCC rings (110 and 200) and one strong FCC 111 peak along with one minor FCC 111 peak. These peaks corresponded to the microstructure observed in Fig. 8(d) with randomly orientated small bainitic LAS grains and two large FCC grains. Two additional maps shown in Fig. 11(b–c) were collected on the FCC side to maximize the diffraction from the tempered martensite. These maps were taken from two adjacent locations along the FB to minimize the diffraction from the LAS matrix, as only a very weak BCC 110 ring was visible. The ring patterns in all three maps matched the cubic structure and no splitting was observed in the 110 and 200 rings, indicating the absence of a tetragonal crystal structure. Notably, the BCC 110 plane spacing continuously increased with distance from the FB, indicating that the BCC phase near the FB was under residual compressive stress, which could be attributed to the martensite transformation.

Fig. 12(b) displays the integrated peaks of FCC 111 and BCC 110 from Fig. 11(a). The half widths at full maximum of these two peaks were compared and it was found that the BCC 110 peak was significantly broader than the FCC 111 peak. This observation suggests that BCC 110 belongs to the tempered martensite phase with a high density of lattice defects. As can be seen in Fig. 12(a), the grain size of the tempered martensite phase is ~ 1 μm , which should not cause any detectable broadening. The Kikuchi pattern from one large tempered martensite grain from the type-B FB is depicted in Fig. 12(c) whereas a perfect Kikuchi pattern from the LAS matrix far from the FB is presented in Fig. 12(d) for comparison purposes. The Kikuchi pattern for the tempered martensitic grain appears blurred and diffused compared to the well-defined sharp lines of the Kikuchi pattern of the LAS matrix, indicating the presence of internal distortion and lattice defects in the tempered martensitic grain.

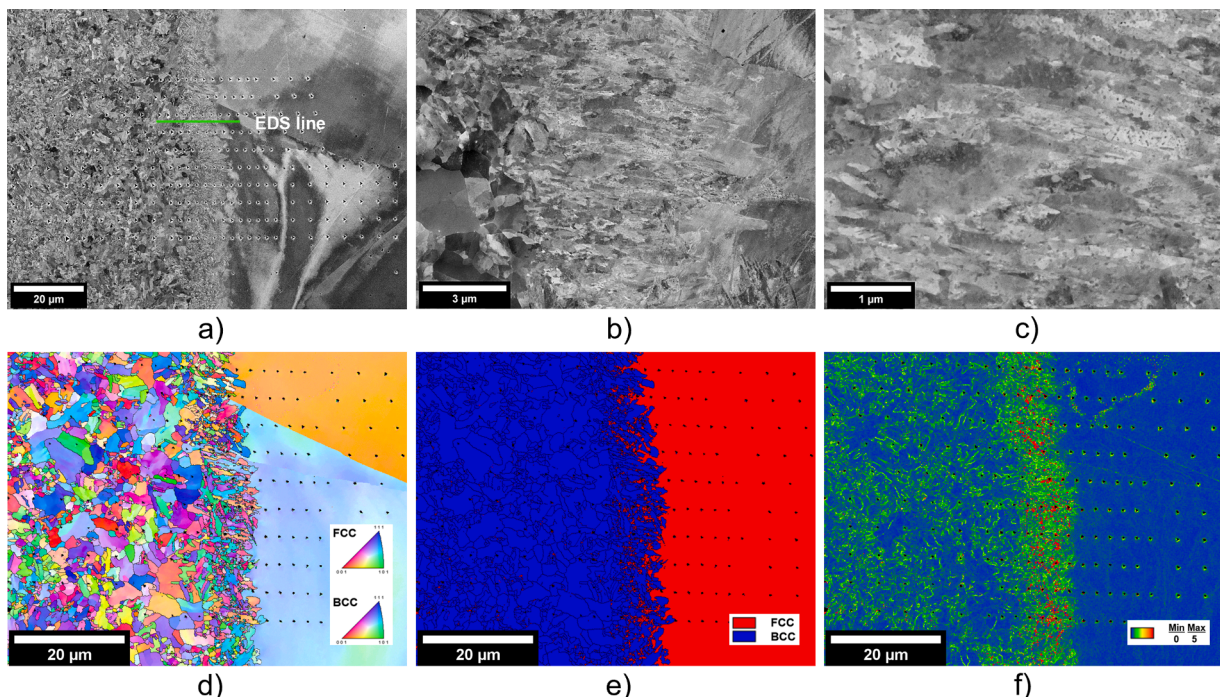


Fig. 8. FB investigation on type-B tempered martensite. (a–c) SEM-BSE, (d) IPF, (e) phase map and (f) KAM mapping. EBSD mapping step size is 0.10 μm .

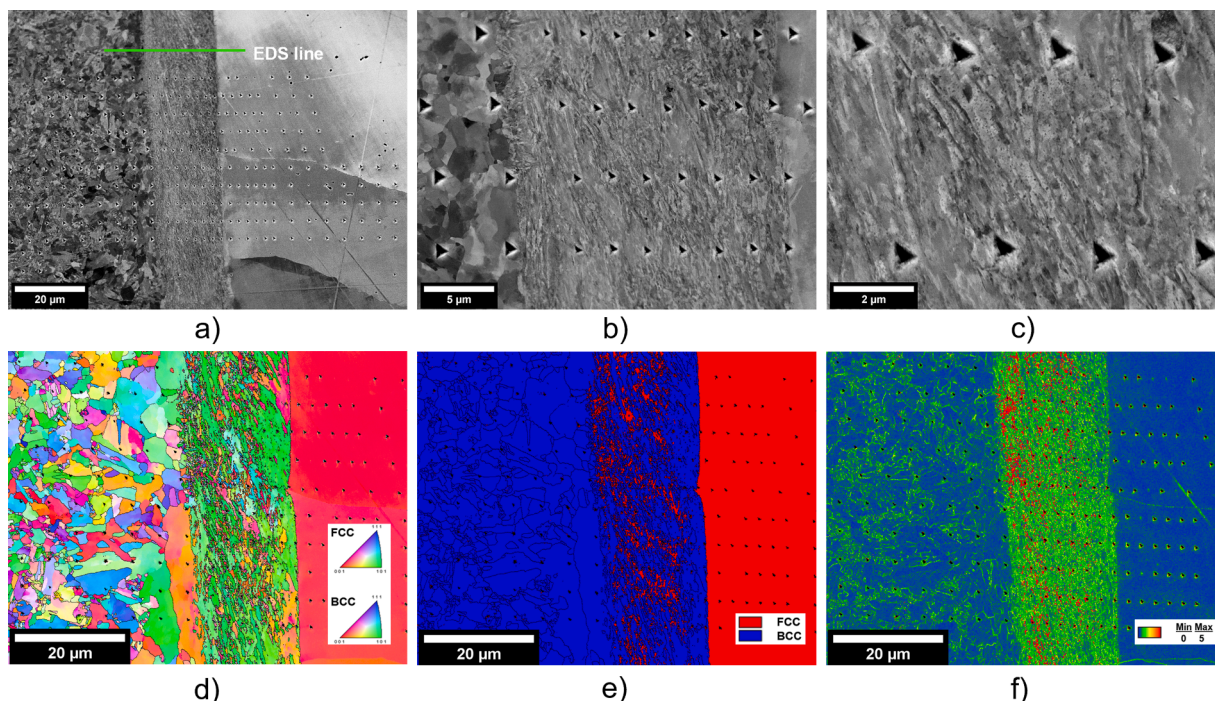


Fig. 9. FB investigation on type-C PMZ. (a-c) SEM-BSE, (d) IPF, (e) phase map and (f) KAM mapping. EBSD mapping step size is 0.03 μm.

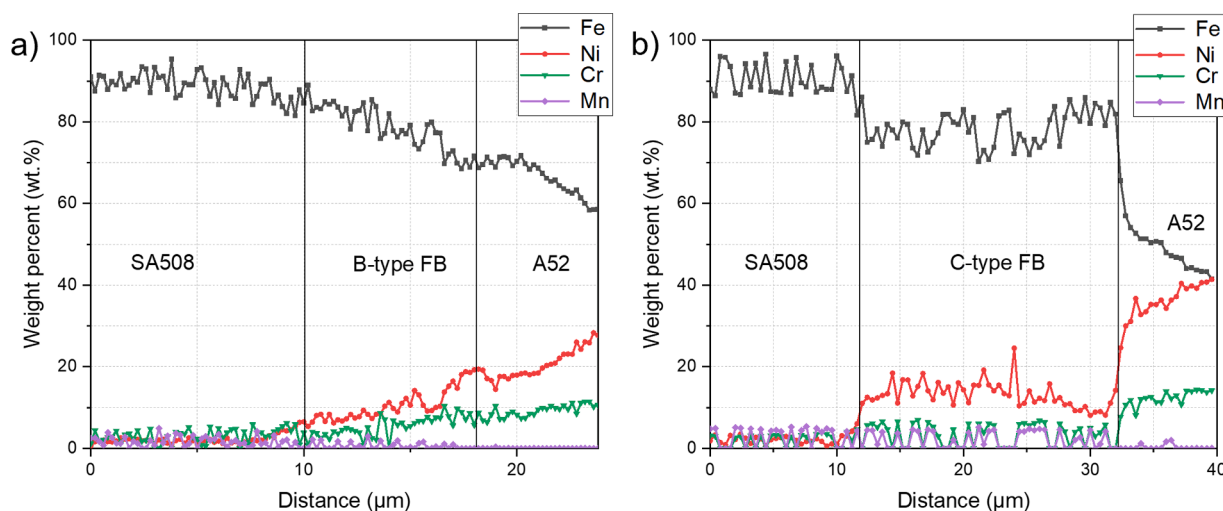


Fig. 10. EDS line scans across the FBs of (a) type-B tempered martensite and (b) type-C PMZ.

3.3. Carbide analysis

A qualitative investigation of carbides was conducted using SEM-EBSD imaging at various distances for the type-B and type-C FBs in the LAS HAZ and in the Alloy 52 weld. The analysis close to the type-B FB in Fig. 13(a) shows tempered martensitic microstructure with a comparatively high concentration of intragranular carbides. At a distance of ~35 μm from the FB on the LAS side (Fig. 13(b)), the carbide concentration decreases significantly in the CDZ. The concentration of carbides increases in the HAZ and beyond the CDZ, where the carbides are both intra- and intergranular. As seen in Fig. 13(c), on the weld side, with a distance of ~40 μm from the FB, only a few carbides are present in the grain boundary. However, with a distance of 100 μm from the FB (Fig. 13(d)), a relatively large cluster of intergranular carbides is observed at the junction of a weld grain boundary.

In Fig. 13(e), the density and size (~50 nm) of carbides observed in a

type-C PMZ FB are comparable to those of the tempered martensitic FB. The width of CDZ depicted in Fig. 13(f) for the type-C FB is greater than that of type-B FB. In Fig. 13(g), the CDZ transitions to the HAZ at a distance of ~48 μm from the FB for a type-C FB. The distribution of carbides in the type-C FB is more clustered with regions of depletion, while in the CDZ transition of a type-B FB shown in Fig. 13(b), the carbide distribution is more uniform, but at a lower density. On the weld side, intergranular carbides consisting of ~300 nm long lamellas are revealed at a distance of 13 μm from the PMZ FB, as shown in Fig. 13(h). In a type-I boundary resulting from the epitaxial growth of grains in the FB region [20] adjacent to the FB, the carbide density is higher near the FB compared to a typical weld grain boundary.

STEM images and elemental maps presented in Fig. 14 revealed the presence of two types of carbides within the LAS HAZ. The predominant carbides are Fe- and Mn-rich with a small amount of Cr, having round morphology with a size ranging from a few nm to over 100 nm. These

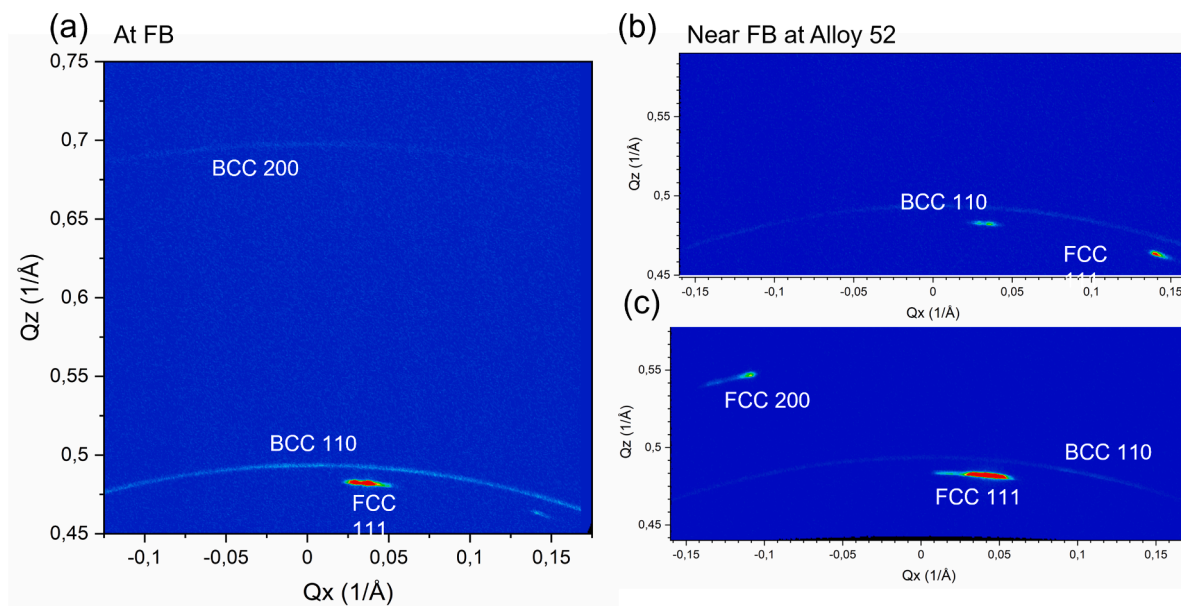


Fig. 11. Reciprocal space mapping on type-B FB at the tempered martensite area. (a) At the FB; (b) at the Alloy 52 side about 120 μm to the FB; (c) at the Alloy 52 side about 120 μm to the FB and 500 μm above the measured place in (b).

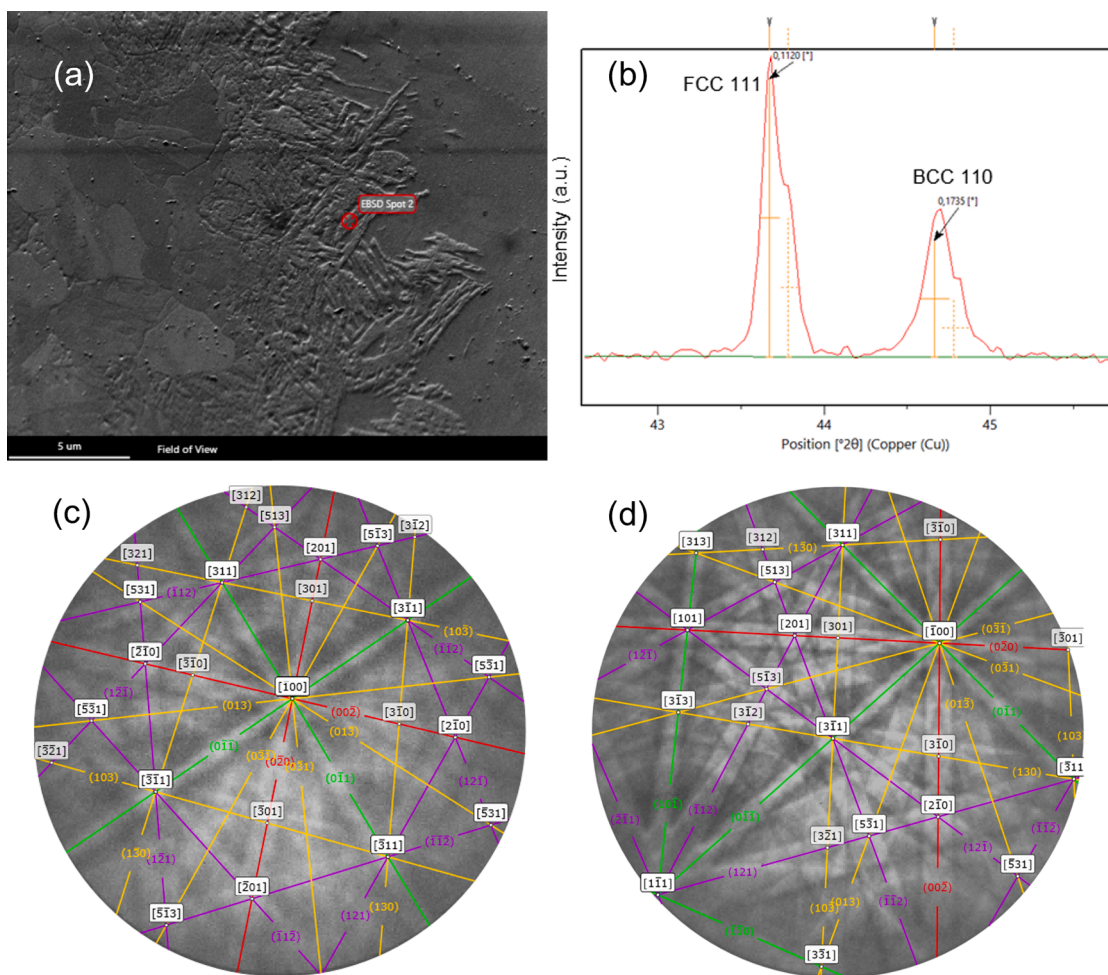


Fig. 12. (a) SE image of type-B FB with tempered martensite. (b) Integrated XRD peaks from Fig. 10(a). (c) Kikuchi pattern from spot marked in (a). (d) Kikuchi pattern of the BCC LAS matrix far from the FB.

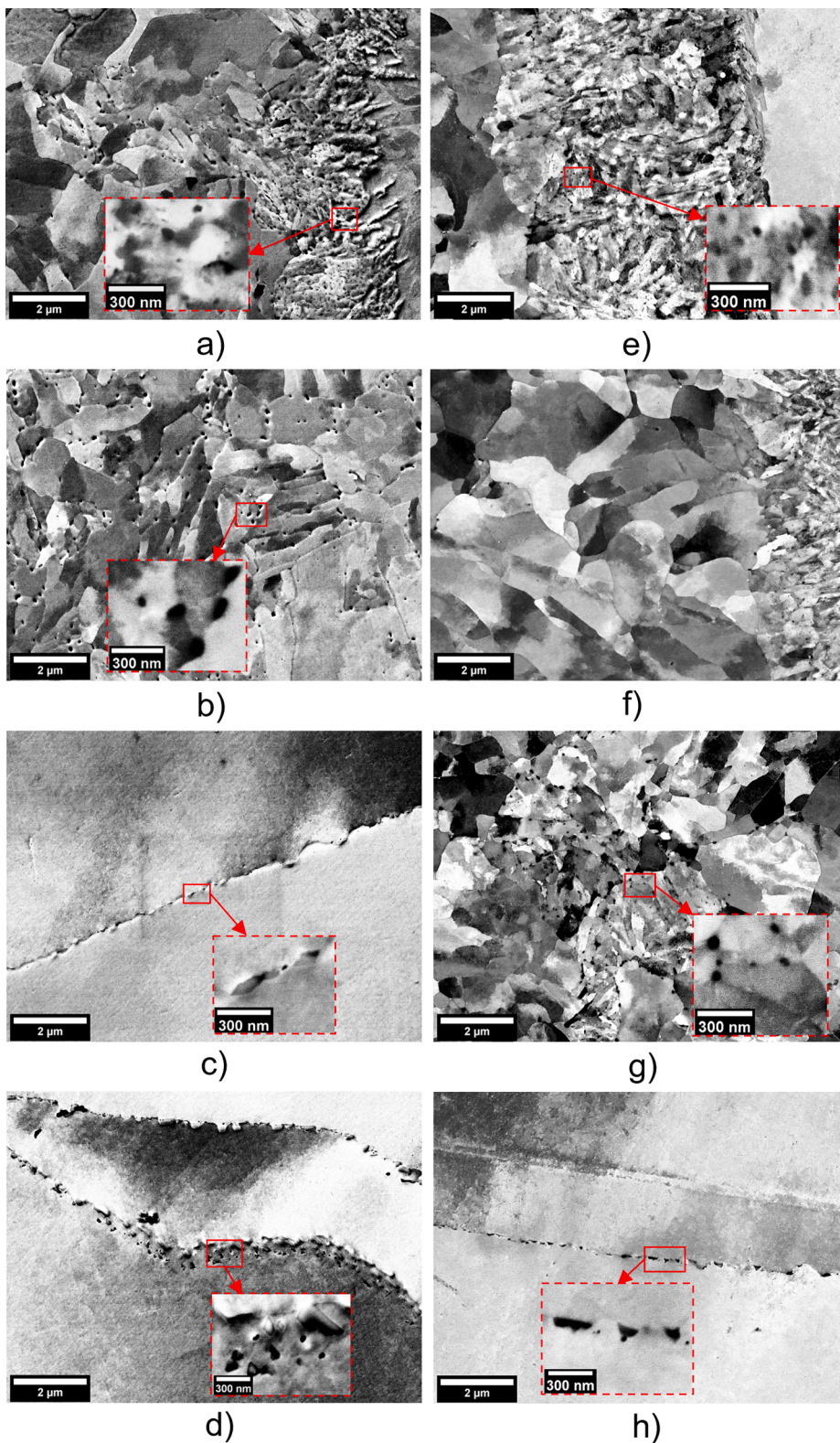


Fig. 13. Carbide evolution across the (a-d) type-B and (e-h) type-C FBs. Analysis from locations in the LAS HAZ with distances of (a) 6 μm (close to FB) and (b) 36 μm (in CDZ transition zone) from the type-B FB, and (e) at the PMZ FB, (f) at 8 μm (in CDZ), and (g) at 48 μm (in HAZ) from the type-C FB. Analysis from locations in the Alloy 52 weld with distances of (c) 40 μm and (d) 100 μm from the type-B FB and (h) at 13 μm from the type-C FB. For all analysis from locations in the LAS HAZ, FB is at the right side of the images whereas from locations in the Alloy 52 weld, FB at the left side of the images.

carbides are distributed both along the grain boundaries and within the grains. Additionally, a second category of carbides, enriched in Mo, has been observed, which are primarily of small size ranging from a few nm to a few tens of nm. Analogous to the (Fe, Mn, Cr) carbides, these Mo-rich carbides can be both inter- and intragranular. The concentration of Cr within the (Fe, Mn, Cr) carbides is considerably lower than that of Mn content. In contrast, the content of Mn and Cr in the Mo-rich carbide

is nearly equivalent. The normalized at% profiles of C, Cr, Mn and Mo are illustrated in Fig. 14, allowing for a comparison of the relative concentrations in the two carbide types.

The Rietveld refinement result of the WAXS patterns observed in the HAZ is presented in Fig. 15. The patterns can be indexed as BCC phase (the major reflections), M_3C carbides and Mo_2C carbides. In the investigated sample, the M_3C carbides (*i.e.* (Fe, Mn, Cr) carbides) and the

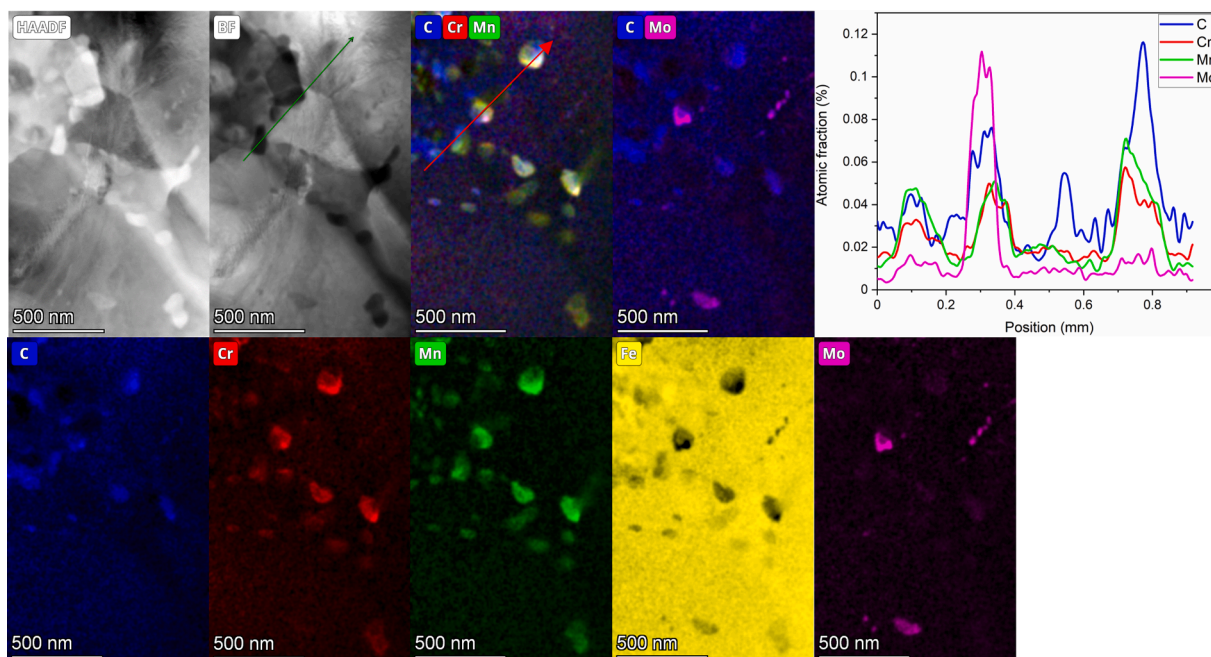


Fig. 14. STEM images (HAADF and BF) and elemental maps of carbides in SA508 at $\sim 83 \mu\text{m}$ distance from the FB. The peaks represent the elemental evolution along the arrow marked in C—Cr—Mn map.

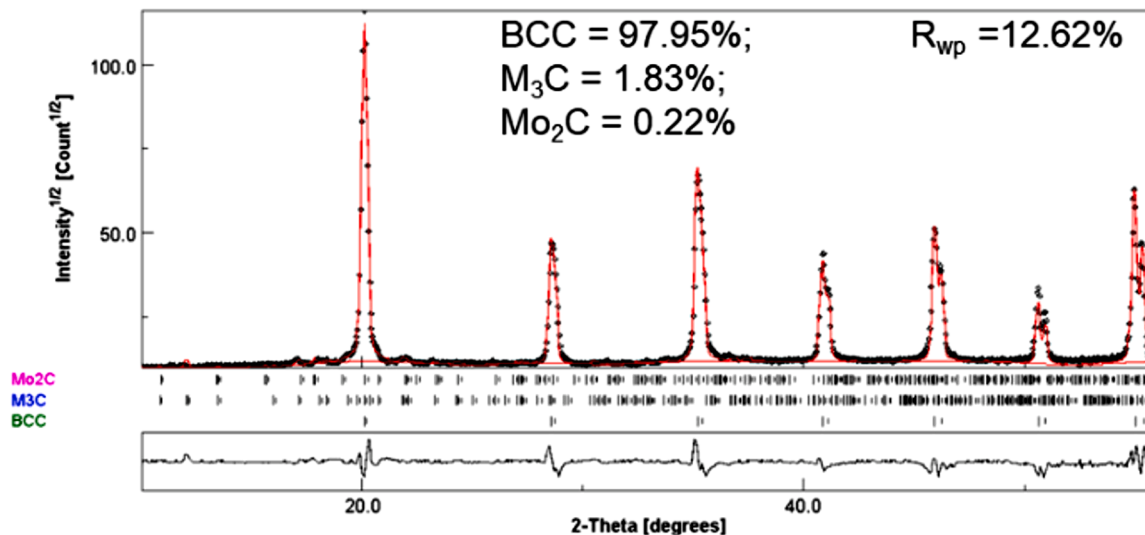


Fig. 15. WAXS patterns from the LAS HAZ.

Mo₂C carbides (*i.e.* Mo-riched carbide) have a volume fraction of 1.83% and 0.22%, respectively, which are consistent with TEM results.

4. Discussion

4.1. Fusion boundary microstructure and mismatch

A DMW with double-sided buttering and a V-groove weld between the bainitic LAS and austenitic stainless steel safe-end was investigated. The focus of this study was on the FB of the SA508 LAS/Alloy 52 buttering. The FBs studied were classified into three types based on their microstructural features and the width of the transition zone. The metallurgical and mechanical mismatch of the different FB types were analyzed. During the multi-pass welding, a low local heat input was found to improve the toughness properties by reducing the cooling rate

and minimizing the HAZ grain coarsening [31]. Moreover, the subsequent beads may have a slight variation in chemical composition (*e.g.* C or Cr contents) compared to the first beads at the interface due to the mixing of the weld pool with the matrix by forming swirls and dilution zones, which causes some variations in the FB microstructure.

The three types of FB microstructures were found to associate with varying FB widths, chemical dilution, width of the CDZ and carbide density in the LAS HAZ, indicating variations in local heat flow and cooling profiles. Type-B FB constituted approximately 15% of the analyzed FB whereas only 1–2% of the FB was categorized as type-C FB. The type-B FB is likely a result of re-melting of metals during multi-pass welding, followed by rapid cooling that led to the formation of martensite microstructure, which was tempered by subsequent weld beads.

The low nano-hardness of the Alloy 52 buttering ($\sim 10 \mu\text{m}$) can be

attributed to a relatively high local heat input, resulting in carbon diffusion across the transition zone. Nanoindentation measurements revealed that type-B FB with tempered martensite phase showed a peak in nano-hardness. In contrast, no significant peak in nano-hardness was observed in the type-C PMZ. The nano-hardness peak associated with the hardened microstructure, *i.e.*, tempered martensite, results in a stronger strength mismatch between the weld and LAS than in the type-C FB. The PMZ is distinct in the indentation map presented in Fig. 7(c). However, the absence of an evident nano-hardness peak in Fig. 7(d) and the nearly constant chemical composition of alloying elements at the PMZ relates to a stronger mixing of materials and a different solidification structure with lower cooling rate compared to the type-B FB.

The microstructure observed in the Type-C PMZ is similar to that often seen in swirls that form during welding when the turbulent weld pool enters the base material and partially melted metal solidifies. However, the welding orientation and technique effectively inhibit swirl formation in the investigated buttered weld.

A high local heat input, *e.g.* between two weld beads, results in an increase in Gibbs free energy and a stronger elemental diffusion, leading to dilution between the buttering weld and the LAS [15]. These findings are consistent with the results in this work. Furthermore, a lower bound nano-hardness of ~ 30 μm in the LAS CDZ was observed in type-C FB, but not in type-B FB, revealing the effect of annealing and stress relief during the buttering process on the LAS side. Higher internal stresses are left in the LAS side in the tempered martensitic FB and the division between the tempered martensite and PMZ is supported by the EBSD analysis and the EDS line scan. The mixing of BCC and FCC phases and chemical compositions in the PMZ is relatively more significant compared to the type-B FB. Similar elemental dilution curves have been reported by Hou et al. [5] and Wang et al. [32]. The relatively high C content in the LAS side lowers the starting temperature of martensite transformation. The local heat input and rapid cooling rate, along with carbide precipitations at the FB, create a favorable system for a diffusion-less process of martensite formation [6]. Carbon migration from the LAS to the weld side and dissolution of primary carbides enhances the carbon equivalent near the interface at high austenitizing temperatures, enhancing hardenability and martensite formation [16]. Chen et al. reported that a gradual change of the alloy elements' contents across the FB may result in the formation of martensite at the FB, whereas a sharp change will not lead to martensite formation [33]. The orientation relationship between the weld metal and the formed martensite is described by a Kurdjumov-Sachs (K-S) relationship [33]. The formation of martensite is mainly controlled by the diffusion of the alloy elements and residual stress resulting from welding [2]. The tetragonality of martensite is lost in this study due to tempering and the tempered martensite FB showed a BCC structure in the XRD analysis. If the carbon content in the FB is below 0.18 wt%, tempered martensite is reported to have a cubic crystal structure, which has been confirmed experimentally by Liu et al. [34], and is in agreement with the current observation. Furthermore, all bands in type-B FB Kikuchi pattern were diffused compared to the sharp Kikuchi bands in the LAS metal matrix, indicating lower band contrast or coincidence index values due to distortion at the type-B FB. This finding correlates with high residual strains and high density of dislocations in the tempered martensite phase.

4.2. Effect of microstructure and mismatch

A comprehensive understanding of metallurgical boundaries, phases and properties at FB regions can lead to a more reliable assessment of the structural integrity of DMW joints. However, existing codes do not mandate such knowledge [35]. This chapter discusses the effect of FB microstructure and mismatch on the structural integrity of DMWs. In the present study, the macro- and micro-hardness peak were discovered in the LAS HAZ adjacent to the FB, while the nano-hardness peak was observed within the FB, specifically for the type-B FB. Nevertheless, in a study on SA508/Alloy 52 NG DMW mock-up without buttering, the

nano-hardness peak was reported to be located in the weld metal side [1], at an interface lacking any distinct FB microstructure, *i.e.*, similar to type-A. The nano-hardness for the NG-DMW aligns well with the position of carbon peak value [3,7]. In comparison to the current weld with buttering, the difference in nano-hardness mismatch may be attributed to differences in the welding technique and parameters, welding orientation and duration of PWHT, causing differences in microstructure and elemental diffusion at the FB. The welding parameters significantly impact the solidification, cooling rate, internal stresses and mixing of metals, which influence the formation of a solidification microstructure at the FB. The orientation of the buttering weld is perpendicular to the typical V-groove or NG weld [36]. During the long PWHT of up to 24 h in the NG mock-up, more carbon in the LAS side diffused from the CDZ to the weld metal side [1]. As the currently investigated buttered mock-up was subjected to relatively short PWHT, the carbon accumulation is mainly concentrated at the FBs. Adjacent to the hardness peak is a region of decreased hardness due to the carbon depletion, *i.e.*, a soft zone.

The mismatch in local mechanical properties in the FBs play a critical role in determining the local fracture resistance and susceptibility to cracking of DMW [12]. In previous studies [37,38], it has been observed that there are abrupt deviations in the path of cracks initiated in DMWs, which occur due to the mismatch in mechanical strength and local microstructures. Nevasmaa et al. [37] suggested that increased strength mismatch results in lowered fracture resistance in regions close to the interface between the LAS and the Alloy 52 weld of DMW. This reduction in fracture resistance was attributed to the increased metallurgical constraint and crack (growth) driving force, accentuated by the high local mismatch state and inherent local inhomogeneity of the near-interface regions [37]. Under conditions of high local strength mismatch, the strength and toughness properties of neighboring microstructures become increasingly important and can dictate the overall fracture behavior of a DMW.

The present study investigated the fracture behavior of DMW using single edge-notched bend specimens (5 mm thick and 10 mm wide) in the temperature range of -130 $^{\circ}\text{C}$ to -180 $^{\circ}\text{C}$. Preliminary study of fracture surfaces and cross-sections of brittle fracture toughness specimens was performed for analyzing the role of FB microstructure in fracture path deviation. A horizontal cross-section of a specimen with the notch nominally placed at 0.3 mm from the FB in the HAZ and a variety of FB microstructures is revealed in Fig. 16. A LOM image after etching (Fig. 16(a)) showed a white dilution zone in the middle along the FB that extended into a swirl. The horizontal cross-section was prepared near the brittle fracture crack initiation site, where the crack propagated mainly along the FB and in the HAZ. It was observed that the weld bead solidification and FB microstructures had an effect on the crack path. The fracture behavior was found to vary depending on the FB microstructure. When a swirl or a distinct type-B FB microstructure (Fig. 16(b,c)) was present, the fracture deviated into the HAZ. However, when a type-A FB microstructure (Fig. 16(d)) was present, the crack propagated very close to or along the FB. Further investigations are ongoing to investigate the effect of carbides on the fracture behavior (as brittle fracture primary initiator), how the local tempered martensite influences the interface toughness and whether the HAZ is weakened due to elemental diffusion. It was concluded that the varying FB microstructure made the brittle fracture path propagation less predictable.

Martensite at the FB has been reported to correlate with the formation of type-II boundaries, which are known to be prone to cracking or FB debonding [39]. The allotropic transformation in the base metal has been reported to result in the evolution of type-II boundaries that are parallel to the FB [20]. Wang et al. studied the microstructure and fracture behavior of a buttered and a V-groove DMW of SA508 and Alloy 52 [12,30]. They observed a larger area of lath martensite at the base material/weld interface due to a high heat input, along with significant type-I and type-II boundaries on the weld side adjacent to the interface [12,30]. Type-II boundaries were also observed in both buttering and

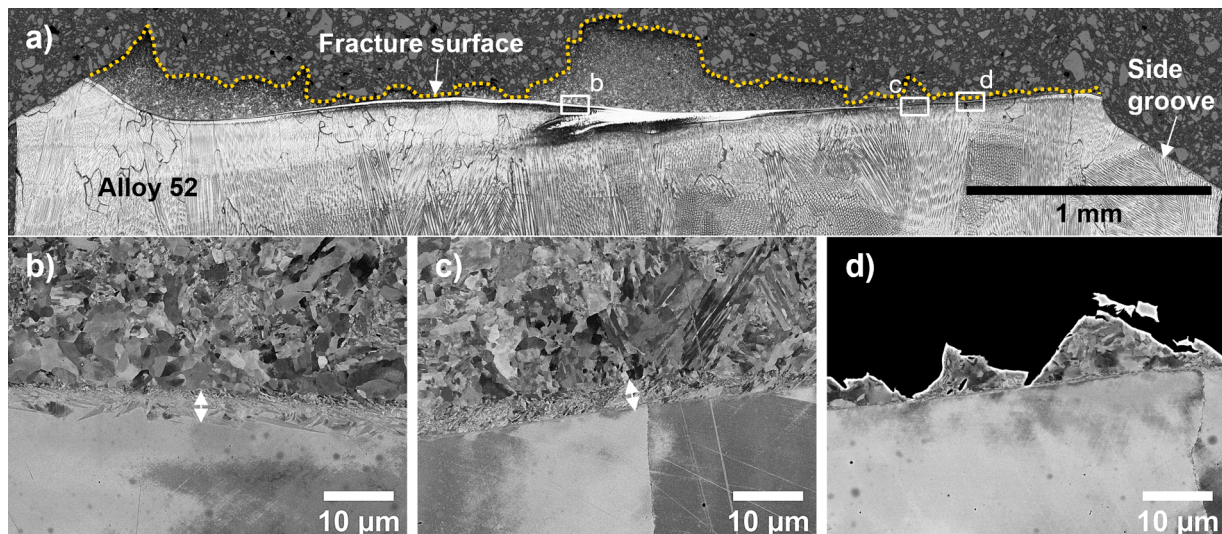


Fig. 16. Horizontal cross-section of a fracture toughness specimen with pre-crack notch at 0.3 mm from the FB, (a) LOM image after etching shows a swirl in the middle and deviating fracture path in the LAS HAZ (yellow line), (b, c) tempered martensite microstructure at the FB with fracture deviated away from the FB, (d) no distinct FB microstructure and fracture along the FB.

NG welds, which was linked to the evolution of the weld pass structure [3,6]. Ming et al. also reported that a high heat input and long high-temperature duration welding process can promote the elemental diffusion, grain boundary migration, and the formation of type-I and type-II boundaries, resulting in a wider CDZ and decreased cracking resistance [17]. However, in the present study, no type-II boundaries and negligible amount of type-I boundaries were observed in the buttering weld side, even along the tempered martensitic FBs. This absence of type-II boundaries reduces the risk of SCC or impurity segregation during aging, potentially enhancing the structural integrity of the LAS/buttering weld interface [21].

The susceptibility of weld metals to ductility dip cracking (DDC) is a significant concern in welding, as it can negatively impact the lifetime and reliability of key components [26]. DDC occurs when intergranular solid-state cracking forms between migrated grain boundaries due to sufficient activation energy during multi-pass welding and reduced ductility in the temperature range of 0.5–0.8 of the melting point [40]. However, no DDC was observed in the investigated DMW. This could be attributed to the use of double-sided buttering technique with specific parameters, which reduces the susceptibility to DDC.

5. Conclusions

This work investigates the microstructure, crystal structure, elemental diffusion, carbide formation and hardness mismatch of the interface of ferritic SA508/austenitic Ni-base Alloy 52 buttering in a double-sided buttered DMW mock-up. The mock-up, provided by Ringhals, is the first-of-a-kind in Europe and fully representative of an actual power plant component.

- Three types of FBs were analyzed: a type-A narrow FB (~80–85% of whole FB and with a width <math><1\ \mu\text{m}</math>), a type-B feathery-like tempered martensitic FB with fine lath-like microstructure (~15% of whole FB and with a width of up to 8 $\mu\text{m}</math>) and a type-C wide PMZ FB (~1–2% of whole FB and with a width of up to 25 $\mu\text{m}</math>). The width of CDZ and coarse-grained region adjacent to the FB depends on the FB type. The width of CDZ ranges from ~20 $\mu\text{m}</math> to ~50 $\mu\text{m}</math>. The widest CDZ was observed for type-C FB and the narrowest for type-B FB.$$$$
- The macro- and micro-hardness peak was found in the LAS HAZ while the nano-hardness peak was observed within the FB, particularly for the type-B FB. The high cooling rate and carbide precipitations at the type-B FB contribute to the nano-hardness peak

with the presence of tempered martensite at the transition zone, resulting in a significant strength mismatch between the weld and LAS. On the other hand, the relatively high local heat input induced diffusion at the type-C PMZ FB promotes the mixing of BCC and FCC phases and grain coarsening in LAS adjacent to the FB, resulting in low-level nano-hardness in Alloy 52 buttering and nearly constant chemical composition in the PMZ.

- XRD analysis revealed the presence of BCC and FCC crystal structures at the LAS and weld metal interface of type-B FB, but no tetragonal martensite phase was observed. The relative volume fraction of martensite at the FB is low and likely lost its tetragonality due to tempering.
- Carbide density and distribution vary with the distance from the FB in the LAS side, with the highest density at the FB and significantly reduced density in the CDZ adjacent to the FB. Beyond the CDZ and ~100 $\mu\text{m}</math> into the HAZ, the carbide density increases again to that of the regular distribution of carbides in a LAS bainitic microstructure. Main carbides found at FBs are M_3C ((Fe, Mn, Cr) carbides) and Mo_2C carbides.$
- The FB microstructure appears to have an effect on brittle fracture crack path, as the crack deviates into the LAS HAZ with a swirl or type-B tempered martensitic FB, while with a type-A narrow FB, the crack propagates along or adjacent to the FB.

Data availability

The data that support the findings of this study are available from the corresponding author upon reasonable request.

CRediT authorship contribution statement

N. Hytönen: Conceptualization, Data curation, Formal analysis, Investigation, Methodology, Writing – original draft, Writing – review & editing. **Y. Ge:** Data curation, Formal analysis, Investigation, Methodology, Writing – original draft. **Z. Que:** Conceptualization, Funding acquisition, Data curation, Formal analysis, Investigation, Methodology, Project administration, Resources, Supervision, Writing – original draft, Writing – review & editing. **S. Lindqvist:** Investigation, Writing – review & editing. **P. Nevasmaa:** Investigation, Writing – review & editing. **I. Virkkunen:** Resources, Supervision, Writing – review & editing. **P. Efsing:** Conceptualization, Project administration, Resources, Supervision, Writing – review & editing.

Declaration of Competing Interest

The authors declare that they have no known competing financial interests or personal relationships that could have appeared to influence the work reported in this paper.

Acknowledgments

The authors wish to express their gratitude for the funding and support from Ringhals AB, OKG AB, Teollisuuden Voima Oyj and VTT Technical Research centre of Finland within the FEMMA (Forum for the Effect of Thermal Ageing and Microstructure on Mechanical and EAC Behavior of Ni-based Alloy Dissimilar Metal Welds) research project. The authors also thank NKS for funding the NKS-FEMMA (AFT/NKS-R (22)134/4) project. The authors would like to thank P. Arffman, J. Lydman, A. Nurmela and L. Sirkiä for the experimental contributions. The authors would like to thank U. Ehrnsten, B. Forssgren, H. Reinwall and H. Hänninen for suggestions and discussions.

References

- M. Ahonen, S. Lindqvist, T. Sarikka, R. Mougnot, E. Leskelä, J. Lydman, U. Ehrnsten, P. Nevasmaa, T. Seppänen, P. Arffman, H. Hänninen, Thermal ageing and mechanical performance of narrow-gap dissimilar metal welds, *VTT Technol.* 333 (2018).
- Z. Chen, Y. Lu, TEM Observation of Martensite Layer at the Weld Interface of an A508III to Inconel 82 Dissimilar Metal Weld Joint, *Metall. Mater. Trans. A* 46A (2015) 5494–5498.
- M. Ahonen, R. Mougnot, T. Sarikka, S. Lindqvist, Z. Que, U. Ehrnsten, I. Virkkunen, H. Hänninen, Effect of thermal ageing at 400°C on the microstructure of ferrite-austenite interface of Nickel-base alloy narrow-gap dissimilar metal weld, *Metals* 10 (2020).
- J. Parker, G. Stratford, Characterisation of microstructures in nickel based transition joints, *J. Mater. Sci.* 35 (2000) 4099–4107.
- J. Hou, Q. Peng, Y. Takeda, J. Kuniya, T. Shoji, J. Wang, E.H. Han, W. Ke, Microstructure and mechanical property of the fusion boundary region in an Alloy 182-low alloy steel dissimilar weld joint, *J. Mater. Sci.* 45 (2010) 5332–5338.
- W.C. Chung, J.Y. Huang, L.W. Tsay, C. Chen, Microstructure and stress corrosion cracking behaviour of the metal in alloy 52-A508 dissimilar welds, *Mater. Trans.* 52 (1) (2011) 12–19.
- A. Akhatova, F. Robaut, M. Verdier, M. Yescas, F. Roch, C. Tassin, H. Landeghem, Microstructural and mechanical investigation of the near fusion boundary region in thermally aged 18MND5 /alloy 52 narrow-gap dissimilar metal weld, *Mater. Sci. Eng. A* 788 (139592) (2020).
- P. Efsing, B. Forssgren, R. Kilian, Root cause failure analysis of defected J-groove welds in steam generator drainage nozzles, in: *Proceedings of the Twelfth International Conference on Environmental Degradation of Materials in Nuclear Power Systems-Water Reactors*, 2005.
- J. Janssen, K. Norrgard, J. Lagerstrom, G. Embring, C. Jansson and P. Efsing, "Structural assessment of defected nozzle to safe-end welds in Ringhals-3 and -4," in *Proc. Fontevraud V Intl. Symp.*, 2000.
- P. Efsing, J. Lagerström, Analysis of a defected dissimilar metal weld in a PWR power plant, in: *Proceedings of the 10th International Conference on Nuclear Engineering*, 2002.
- S. Yoo, K. Choi, C. Bahn, S. Ki, J. Kim, J. Kim, Effects of thermal aging on the microstructure of Type-II boundaries in dissimilar metal weld joints, *J. Nucl. Mater.* 459 (2015) 5–12.
- H. Wang, G. Wang, F. Xuan, C. Liu, S. Tu, Local mechanical properties of a dissimilar metal welded joint in nuclear power systems, *Mater. Sci. Eng. A* 568 (2013) 108–117.
- A. Blouin, S. Chapuliot, S. Marie, C. Niclaes, J. Bergheau, Brittle fracture analysis of Dissimilar Metal Welds, *Eng. Fract. Mech.* 131 (2014) 58–73.
- S. Lindqvist, N. Hytönen, L. Sirkiä, P. Arffman, J. Lydman, Y. Ge, P. Nevasmaa, Z. Que, Fracture in the Ductile-To-Brittle Transition Region of A Narrow-Gap Alloy 52 and Alloy 52 Dissimilar Metal Weld With Battering, *ASME 2022 Pressure Vessels, Las, Vegas, US, 2022*, <https://doi.org/10.1115/PVP2022-80690>.
- Z. Chen, Y. Lu, X. Ding, T. Shoji, Microstructural and hardness investigations on a dissimilar metal weld between low alloy steel and Alloy 82 weld metal, *Mater. Charact.* 121 (2016) 166–174.
- K. Ravikiran, H. Mehtani, K. Sivaprasad, M. Prasad, S. Kumar, P. Singh, M. Ghosh, Influence of nickel-based battering material on welded joint between SA508 low alloy steel and 304LN stainless steel, *Int. J. Press. Vessels Pip.* 195 (104576) (2022).
- H. Ming, J. Wang, E. Han, Comparative study of microstructure and properties of low-alloy-steel/nickel-based-alloy interfaces in dissimilar metal weld joints prepared by different GTAW methods, *Mater. Charact.* 139 (2018) 186–196.
- P. Joly, M. Yescas, E. Keim, Fracture toughness in the ductile-brittle transition and thermal ageing behavior of decarburized heat affected zone of Alloy 52 dissimilar metal welds of nuclear components, in: *Proceedings of the ASME-2014 Pressure Vessel and Piping Conference*, Anaheim, California, USA, 2014.
- N. Hytönen, Z. Que, S. Lindqvist, J. Lydman, Y. Ge, I. Virkkunen, U. Ehrnsten, P. Rautala, P. Efsing, B. Forssgren, Fusion boundary microstructure and fracture behaviour of a narrow-gap alloy 52 dissimilar metal weld and an alloy 52 dissimilar metal weld with battering, in: *Proceedings of the International Symposium Contribution of Materials Investigations and Operating Experience to LWRs' Safety, Performance and Reliability*, Fontevraud, Avignon, France 10, 2022.
- L. Dong, Y. Zhang, Y. Han, Q. Peng, E. Han, Environmentally assisted cracking in the fusion boundary region of a SA508/Alloy 52M dissimilar metal weld joint in simulated primary pressurized water reactor environments, *Corros. Sci.* 190 (109668) (2021).
- J. Gao, J. Tan, Z. Zhang, M. Jiao, X. Wu, L. Tang, Y. Huang, Effects of welding columnar grain orientation and strain rate on corrosion fatigue behavior of Alloy 52/52M weld metal in high-temperature water, *Corros. Sci.* 180 (109196) (2021).
- K. Choi, S. Yoo, S. Kim, T. Kim, J. Ham, J. Lee, J. Kim, Microstructural evolution and corrosion behaviour of thermally aged dissimilar metal welds of low-alloy steel and nickel-based alloy, *Corros. Sci.* 153 (2019) 138–149.
- Y. Ge, Z. Que, K. Lindgren, N. Hytönen, M. Thuvander, Effect of thermal aging on microstructure and carbides of SA508/Alloy 52 dissimilar metal weld, *Materials Characterization* 200 (2023) 112880.
- H. Wang, G. Wang, F. Xuan, S. Tu, Fracture mechanism of a dissimilar metal welded joint in nuclear power plant, *Eng. Fail. Anal.* 28 (2013) 134–148.
- Z. Zhai, H. Abe, Y. Miyahara, Y. Watanabe, Effects of phosphorus segregation on stress corrosion cracking in the heat-affected zone of a dissimilar metal joint between a Ni-base alloy and a low alloy steel, *Corros. Sci.* 92 (2015) 32–42.
- J. Gao, J. Tan, M. Jiao, X. Wu, L. Tang, Y. Huang, Role of welding residual strain and ductility dip cracking on corrosion fatigue behavior of Alloy 52/52M dissimilar metal weld in borated and lithiated high-temperature water, *J. Mater. Sci. Technol.* 42 (2020) 163–174.
- J. Kim, K. Choi, C. Bahn, J.H. K, *In situ* Raman spectroscopic analysis of surface oxide films on Ni-base alloy/low alloy steel dissimilar metal weld interfaces in high-temperature water, *J. Nucl. Mater.* 449 (2014) 181–187.
- T. Nelson, J. Lippold, M. Mills, Nature and evolution of the fusion boundary in ferritic-austenitic dissimilar weld metals, Part 1: nucleation and growth, *Weld. Res.* (1999) 329–337.
- J. Kim, S. Kim, K. Choi, C. Bahn, I. Hwang, J. Kim, *In-situ* investigation of thermal aging effect on oxide formation in Ni-base alloy/low alloy steel dissimilar metal weld interfaces, *Corros. Sci.* 86 (2014) 295–303.
- G. Wang, H. Wang, F. Xuan, S. Tu, C. Liu, Local fracture properties and dissimilar metal integrity in nuclear power plants, *Front. Mech. Eng.* 8 (2013) 283–290.
- S. Kou, *Welding Metallurgy*, 2nd ed., John Wiley & Sons, Inc., 2003.
- S. Wang, J. Ding, H. Ming, Z. Zhang, J. Wang, Characterization of low alloy ferritic steel-Ni base alloy dissimilar metal weld interface by SPM techniques, SEM/EDS, TEM/EDS and SVET, *Mater. Charact.* 100 (2015) 50–60.
- Z. Chen, B. Zhao, T. Liu, Y. Lu, T. Shoji, Oxidation behavior of the dilution zone of a dissimilar metal weld between low alloy steel and alloy 82 in high temperature water, *Mater. Charact.* 155 (109816) (2019).
- X. Liu, F. Zhong, J. Zhang, M. Zhang, M. Kang, Z. Guo, Lattice-parameter variation with carbon content of martensite I. X-ray diffraction experimental study, *Phys. Rev. B* 52 (1995) 9970–9978.
- D. Rathod, S. Pandey, P. Singh, S. Kumar, Microstructure-dependent fracture toughness (JIC) variations in dissimilar pipe welds for pressure vessel system of nuclear plants, *J. Nucl. Mater.* 493 (2017) 412e425.
- N. Hytönen, Y. Ge, Z. Que, S. Lindqvist, J. Lydman, U. Ehrnsten, P. Rautala, I. Virkkunen, P. Efsing, Effect of microstructure on mechanical behavior of Ni-base alloy dissimilar metal welds, in: *Proceeding of the 20th International Conference on Environmental Degradation of Materials in Nuclear Power Systems-Water Reactor meeting*, Colorado, USA, 2022. ED2021-17104.
- P. Nevasmaa, P. Holmström, P. Karjalainen-Roikonen, T. Sarikka, M. Ahonen, R. Mougnot, U. Ehrnsten, A. Brederholm, P. Aaltonen, H. Hänninen, Fracture mechanical characterisation of ferrite-austenite dissimilar metal welds (DMWs) for elevated temperature service in view of metallurgical mismatch, in: *Proceeding of the International Conference on Life Management and Maintenance for Power Plants*, Helsinki, 2013.
- S. Lindqvist, Z. Que, P. Nevasmaa, N. Hytönen, The effect of thermal aging on fracture properties of a narrow-gap Alloy 52 dissimilar metal weld, *Eng. Fract. Mech.* 281 (2023) 109056.
- T.W. Nelson, J.C. Lippold, M.J. Mills, Nature and evolution of the fusion boundary in ferritic-austenitic dissimilar weld metals, Part 2: on-cooling transformations, *Weld. J.* 79 (2000) 267–277.
- H. Liang, C. Wang, Z. Wu, Corrosion behavior of alloy 52M and 52MSS weld surfacing, *Int. J. Press. Vessels Pip.* 191 (104356) (2021).



Effect of thermal aging on microstructure and carbides of SA508/Alloy 52 dissimilar metal weld

Y. Ge^a, Z. Que^{a,*}, K. Lindgren^b, N. Hytönen^a, M. Thuvander^b

^a Advanced Materials for Nuclear Energy, VTT Technical Research Centre of Finland, Kivimiehentie 3, FI-02044 VTT, Finland

^b Microstructure Physics, Department of Physics, Chalmers University of Technology, Göteborg 412 96, Sweden

ARTICLE INFO

Keywords:

Dissimilar metal welds
Thermal aging
Alloy 52
Carbides
Narrow gap

ABSTRACT

A narrow-gap SA508/Alloy 52 dissimilar metal weld (DMW) mock-up, fully representative of an actual nuclear component, was investigated in this work. The microstructure and carbides formed in the low alloy steel fusion boundary (FB) and heat affected zone (HAZ) can act as brittle fracture initiators and could influence the brittle fracture behavior. However, the amount of information available in the open literature on the microstructural changes and carbide formation in DMW occurring upon post-weld heat treatment and long-term thermal aging is very limited. The microstructure and carbide type, morphology and size in the carbide precipitation zone (CPZ, up to 1.5 μm from FB), carbon depletion zone (CDZ, up to 40–50 μm from FB) and HAZ (up to 2 mm from FB) of the plant-relevant DMW in post-weld heat-treated and thermally-aged (400 °C for 15,000 h, corresponding to 90 years of operation) conditions were analyzed with analytical electron microscopy, wide-angle X-ray scattering and atom probe tomography. Long-term thermal aging increases the microhardness peak close to the FB, triples the width of the CPZ and coarsens the carbide size in the HAZ (up to a magnitude). There is no evidence of a significant phosphorus segregation to grain boundaries due to thermal aging.

1. Introduction

Dissimilar metal welds (DMWs) are commonly used to join austenitic and ferritic/bainitic components in the nuclear reactor coolant pressure boundary with a Ni-based filler metal [1] [2] [3]. The crystallographic difference and the chemical composition gradient (specifically C and Cr) at the fusion interface between the bainitic reactor pressure vessel steel and the austenitic weld metal results in a complex fusion boundary (FB) microstructure and a mismatch of corrosion and strength at the interfaces [4] [5] [6] [7]. DMWs are critically influencing the structural integrity of the nuclear power systems, structures and components [8] [9] [10].

The carbides formed at the FB and in the low alloy steel (LAS) heat affected zone (HAZ) can act as brittle fracture initiators and thus the type, morphology and size of carbides significantly influence the brittle fracture behavior [11]. In addition, hardness mismatch at the DMW FB was governed by the change of precipitate morphology and size due to dislocation cutting or bowing phenomena [12]. However, the amount of information available in the open literature on the microstructural changes and carbide formation occurring at the FB upon post-weld heat treatment (PWHT) and during long-term thermal aging is very limited

[3] [13] [14] [15]. Furthermore, the segregation of impurity elements (e.g. phosphorus) during heat treatment and aging and carbon diffusion from LAS to Alloy 52, are known to increase susceptibility to cracking and stress corrosion cracking [16] [17]. Moreover, the narrow-gap (NG) weld without buttering and subsequent PWHT exhibits different microstructures at the FB and HAZ compared to Alloy 52 buttering welding technique [18] [19]. Understanding the effects of long-term thermal aging on the detailed FB microstructures and carbide formation are crucial for the integrity evaluation and safe long-term operation of nuclear components with NG DMW [20] [21].

Lindqvist et al. [22] [23] reported that for NG SA508/Alloy 52 DMW, when the notch of the fracture toughness T_0 test is placed in the HAZ near the FB, the brittle fracture crack deviates to the FB after initiation and propagates along the FB in most cases. However, if the notch has a distance to the FB ≥ 0.3 mm, the crack does not deviate to the FB and has a crack path parallel to the FB, which ends up with very low fracture toughness. This work reveals that the investigation of brittle fracture behavior and the knowledge of microstructure and carbide formation in both near FB region and HAZ are important in respective of structural integrity.

In this work, the microstructure and carbides' crystal structure,

* Corresponding author.

E-mail address: zaiqing.que@vtt.fi (Z. Que).

<https://doi.org/10.1016/j.matchar.2023.112880>

Received 13 January 2023; Received in revised form 18 March 2023; Accepted 31 March 2023

Available online 5 April 2023

1044-5803/© 2023 The Authors. Published by Elsevier Inc. This is an open access article under the CC BY license (<http://creativecommons.org/licenses/by/4.0/>).

chemistry, morphology and size in the LAS FB carbide precipitation zone (CPZ, normally up to 1.5 μm from FB), carbon depletion zone (CDZ, up to 40–50 μm from FB) and HAZ (up to 2 mm from FB) were analyzed. Advanced characterization including analytical electron microscopy, wide-angle X-ray scattering (WAXS) and atom probe tomography (APT) were applied. The effects of long-term thermal aging on the microstructures and carbide formation and the fracture mechanical behavior are discussed.

2. Experimental methods and materials

2.1. Materials

In this study, a 1:1 scale DMW safe-end mock-up fully representative of an actual component in a Finnish nuclear power plant is investigated [24] [25]. The figure of the structure of the DMW mock-up investigated in this study is presented in Fig. 1. The technical details of the DMW mock-up are given in Table 1. The chemical compositions of the materials are given in Table 2.

The mock-up is a NG DMW full-scale pipe mock-up provided by TVO. It consists of an Alloy 52 (UNS N06052) NG weld joining SA508 nozzle and stainless steel AISI 316LN safe-end. The inner surface of the LAS wall has a 308L stainless steel cladding. The mock-up is welded one bead per layer and is ~ 9 mm wide and ~ 94 mm thick. The welding was performed in circumferential direction and the weld was post weld heat-treated at 550 $^{\circ}\text{C}$ for 15 h and 610 $^{\circ}\text{C}$ for 7 h. The investigated conditions are as-received post weld heat-treated condition (“NG AR”) and the thermally aged condition after 15,000 h at 400 $^{\circ}\text{C}$ (“NG TA”). This thermal aging corresponds to 90 years of nuclear power plant operation, when the P segregation at grain boundaries is considered as the main aging mechanism [19].

2.2. Microstructural characterization

The Vickers micro-hardness measurements with loads of 1 kg (HV1) and 0.3 kg (HV0.3) across the FB were performed using a Struers DuraScan-80 device.

Table 1

Technical details of the NG mock-up investigated.

	NG mock-up
Nozzle	SA508 gr.2
Cladding	SS308L/309 L
Weld	Alloy 52 narrow-gap
Safe-end	AISI 316LN
PWHT	17 h at 550 $^{\circ}\text{C}$ + 7 h at 610 $^{\circ}\text{C}$
Welding method	TIG welding
Conditions	PWHT or thermally aged at 400 $^{\circ}\text{C}$ for 15,000 h

The specimens were cut by electrical discharge machining to a thickness of ~ 0.5 mm and mechanically thinned from both sides to ~ 100 μm . The final thinning was carried out by twin jet electropolishing using a Struers TenuPol-5 electropolisher with an electrolyte consisting of 1 M concentration of NaCl in ethylene glycol and 200–400 mL ethanol. Some thin foils were further ion milled to obtain a thin area near the FB by Gatan Precision Ion Polishing System (PIPS, model 691).

Transmission electron microscopy (TEM) was used to characterize the carbides. Scanning TEM (STEM) high-angle annular dark-field (HAADF) and bright-field (BF) images and chemical information of carbides were acquired on FEI Talos F200X STEM equipped with Super-X EDS system operating at 200 kV. A Zeiss Crossbeam 540 scanning electron microscope (SEM) equipped with an energy dispersive X-ray spectroscopy (EDS) system was used for baseline microstructural characterization for all TEM foils.

WAXS was performed with a Xenoxs Xéus 3.0 system with Mo tube. Selected TEM foils were also studied with WAXS in transmission mode with a Mo tube of 700 μm beam size. The measured area is located at the HAZ. The 2D WAXS patterns are integrated and converted into 1D profiles and refined with MAUD program [26].

The APT specimens were electropolished using a standard two-step method. A LEAP 3000X HR with a detection efficiency of 37% was used for the APT analysis. The pulse frequency was 200 kHz, the pulse fraction was 20%, and the temperature 70 K. For the reconstruction and analysis, IVAS 3.6 was used. Care was taken for the analysis of the P content. P evaporated mostly as P^{2+} and P^{3+} . P^{+} was also included in the

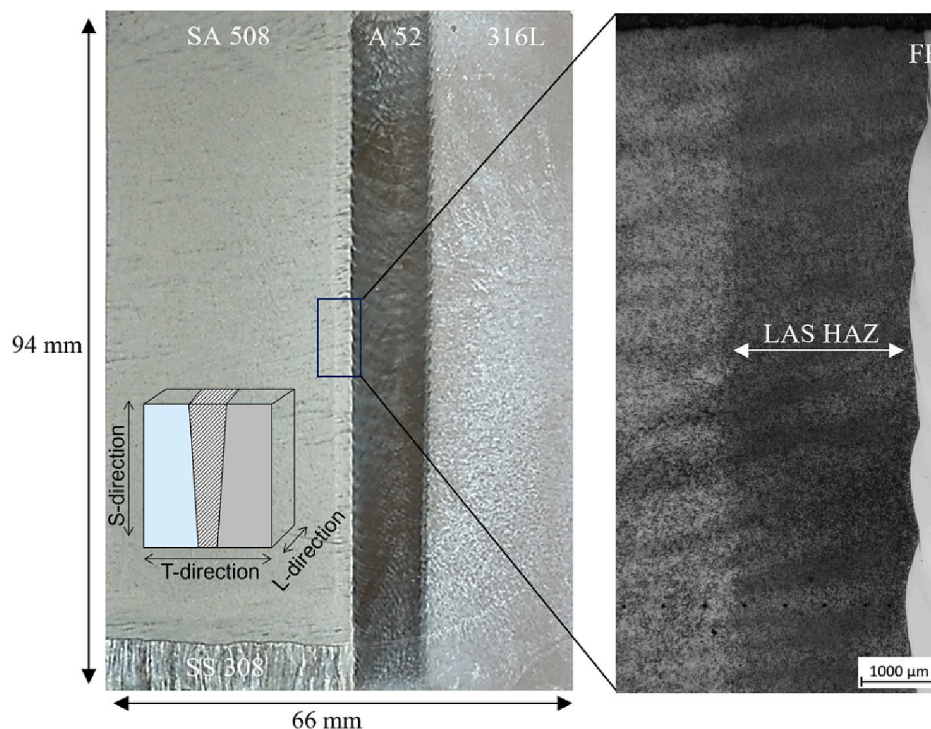


Fig. 1. NG welded dissimilar joint of the investigated mock-up.

Table 2

Chemical composition of the mock-up LAS nozzle material and Alloy 52 weld in weight%.

	C	Cr	Mo	Ni	Mn	Si	P	S	Al	Ti	Cu	V	Fe
SA508	0.18	0.12	0.49	0.78	1.49	0.19	0.005	0.001	0.02	0.002	0.06	–	Bal.
Alloy 52	0.023	29.93	<0.01	Bal.	0.26	0.15	<0.005	0.0007	0.66	0.54	<0.01	–	10.4

deconvolution of peaks as it overlaps with Ni^{2+} . It was found to not give a significant contribution to the P content.

3. Results

3.1. DMW general microstructure and microhardness

The microhardness profiles of HV1 and HV0.3 across the FB in the NG AR and NG TA samples are shown in Fig. 2. The microhardness peaks are close to the FB of the LAS side in both materials. The HV1 and HV0.3 profiles are rather similar. It is evident that the NG TA material has a higher microhardness peak (~ 20 HV) than the NG AR material and the position of the peak hardness is closer to the FB in the NG TA material.

As shown in Fig. 3, the general microstructure and precipitations of the FB CPZ (0.5–1.5 μm from FB), CDZ (40–50 μm from FB) and HAZ (up to 2 mm from FB) of SA508/Alloy 52 were investigated using TEM foils with SEM. At the FB of the LAS side, a fine CPZ about a few hundred nanometer wide was formed (more discussion in Chapter 3.2). It is noted the fine carbides in the CDZ (more discussion in Chapter 3.3) are mostly located in small grains whereas large grains are almost carbide free. In the HAZ (more discussion in Chapter 3.4), the grain size is further decreased with increased distance to the FB and the carbide distribution tends to be more homogeneous. Carbides are formed both at grain boundaries and within grains in the HAZ. A moderate difference in the microstructure in the CDZ and HAZ was observed in the AR and TA materials. The width of CDZ is slightly narrower for the TA material than the AR material and the grain size shows a larger variation in the CDZ of the AR material. The reduction of the width of the CDZ implies a continuous diffusion of C from the CDZ to the CPZ during long-term thermal aging.

3.2. CPZ microstructure and carbide analysis

The microstructure and carbide formation at the FB CPZ (0.5–1.5 μm from the FB) were investigated with SEM and TEM. An intensive carbide accumulation area (CPZ) is found in both AR and TA materials due to the high content of the strong carbide-forming element Cr at the FB as shown in Fig. 4. Though the width of the CPZ varies locally along the FB,

there is a clear difference in the CPZ width between AR and TA materials. As shown in Fig. 4, the CPZ of the AR and TA materials is up to 500 nm and >1500 nm, respectively. The number of carbides is much lower and the size of the carbides is also smaller in the AR material compared to the TA material. The elemental maps in Fig. 4 reveal that the carbides are (Fe, Cr, Mn) carbides with higher Cr than Mn content. In addition, the NG TA material contains Mo-rich carbides and Cr-rich carbides, which are also found at grain boundaries of Alloy 52.

TEM BF images and elemental maps in Fig. 5 reveal the carbides at the FB between LAS and Alloy 52 in the NG AR material. The FB is determined in the image by selected area electron diffraction (SAED) patterns, which show LAS with body centered cubic (BCC) lattice at the left side and Alloy 52 with face center cubic (FCC) lattice at the right side. Near the FB, the BCC grains are columnar with a similar orientation. Nanometer-sized Cr nitrides (≤ 30 nm) with both rod shape and round shape were found in the columnar grains next to the FB at the LAS side. The Mo content in these nitrides is also slightly higher than in the matrix. Enriched Ni and Mn islands are found inside the BCC phase at the FB. Moreover, the Ni and Mn elements were found to segregate at the FBs and boundaries of islands as illustrated in the line profile of Fig. 5 (d). Except these island areas, the Ni and Cr contents continuously decrease with increasing distance from the FB. In this imaged area only one (Fe, Cr, Mn) carbide of about 40 nm size is found at the lower left corner with higher Cr content than the Mn content. It is noted that a quite high dislocation density is observed in both the FCC and BCC phases near the FB. The SAED pattern in Fig. 5(c) is from one (Fe, Cr, Mn) carbide, where weak reflections can be indexed with M_3C type carbide along zone axis $[11\bar{1}]$ and strong reflections from surrounding BCC grains that are close to the (111) zone axis.

The FB CPZ microstructure revealed by TEM is in good agreement with the SEM observations in Fig. 4. The nanometer-sized Cr nitride accumulated area extends about 100 nm and locally up to 300 nm from the FB. Carbides, rich in Fe, Cr and Mn, dominate in the region about 200–500 nm from the FB together with additional nanometer-sized nitrides and carbides. Therefore, the CPZ is about 400–500 nm wide between the FB and the CDZ in the NG AR material.

The Cr content in the (Fe, Cr, Mn) $_3\text{C}$ carbides continues to decrease as the Cr concentration decreases in the matrix with increasing distance

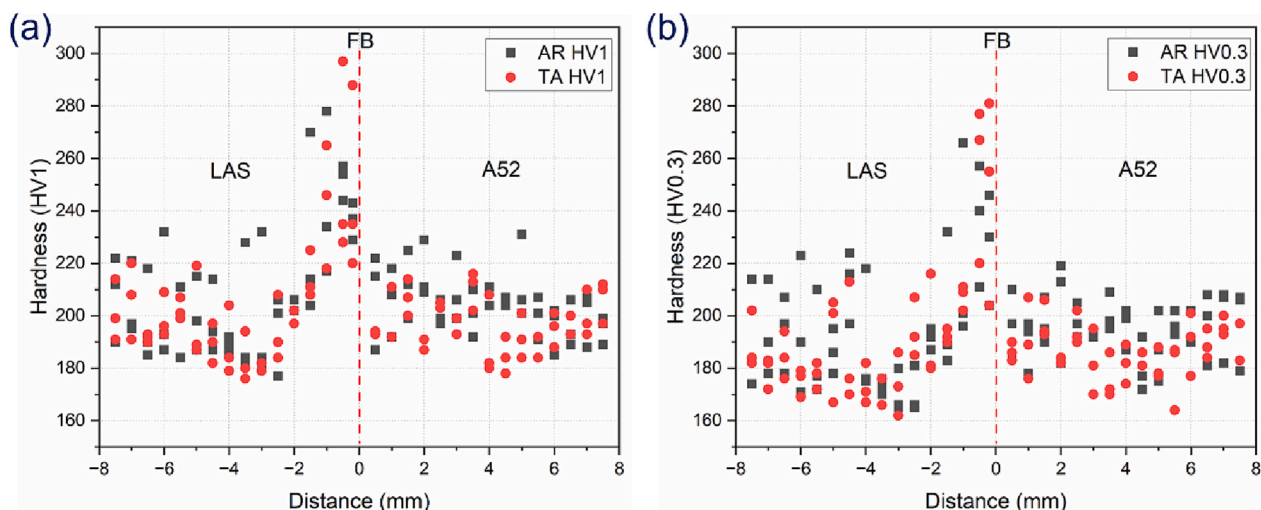


Fig. 2. Microhardness profiles of HV1 and HV0.3 across the FB in the NG AR and NG TA samples.

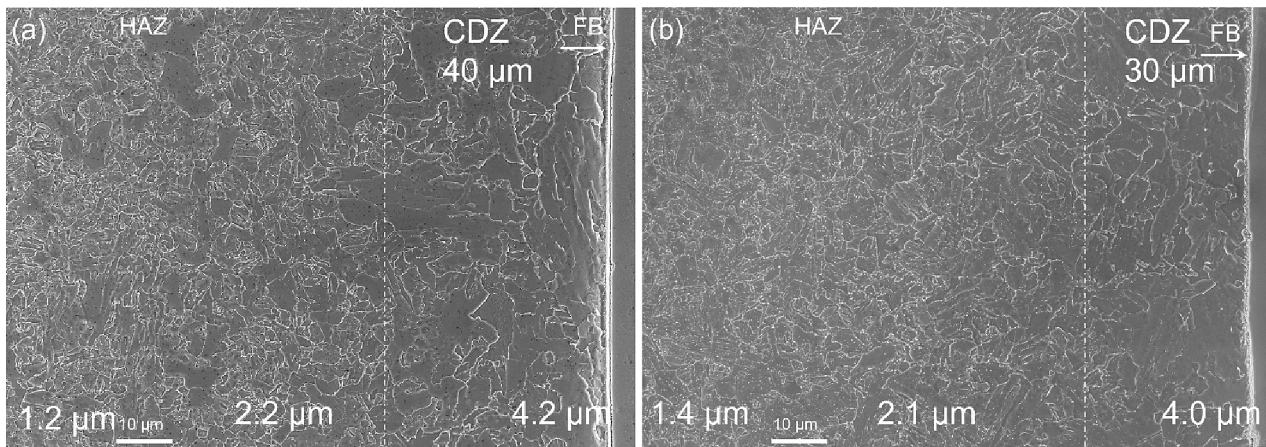


Fig. 3. SEM images (using secondary electrons (SEs)) show the grain size distribution and CDZ width in the LAS. (a) NG AR and (b) NG TA.

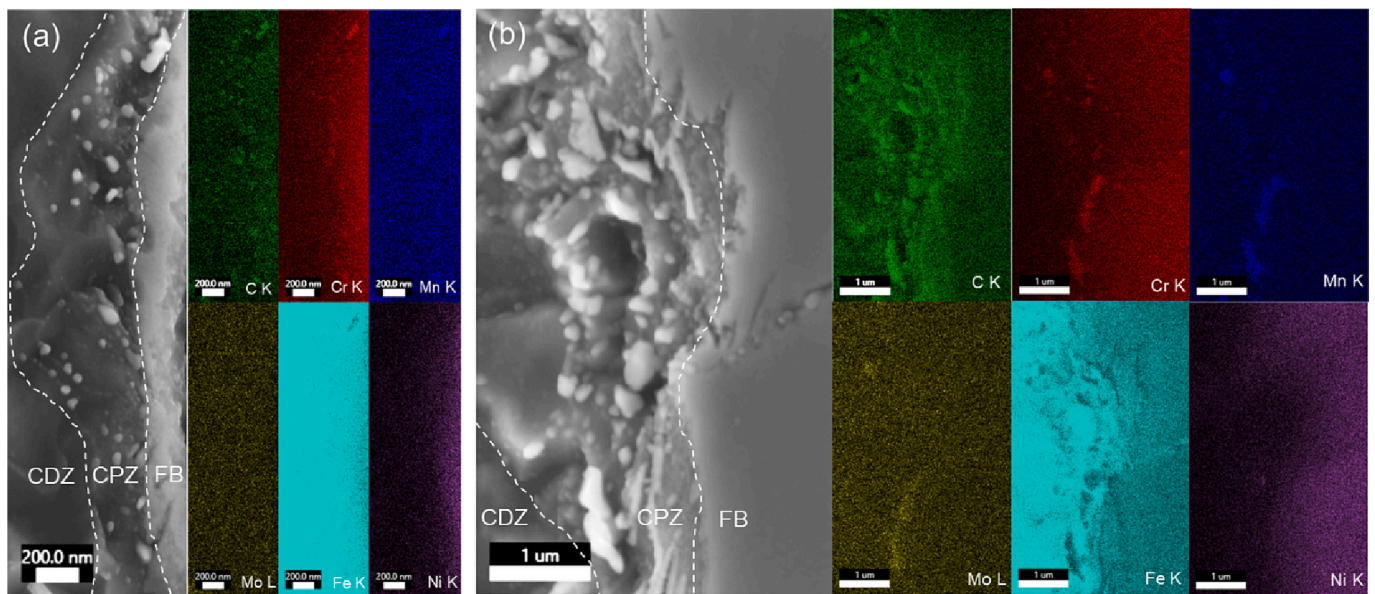


Fig. 4. SEM/EDS elemental maps of carbides at the FB of the LAS. (a) NG AR and (b) NG TA.

from the FB. The microstructure and the carbides at the interface of the CPZ and CDZ are shown in Fig. 6(b). Except a few nano-sized nitrides, carbides are almost invisible in the neighbor CDZ grains. The majority of these carbides are relatively large with a size range of 50–100 nm. A SAED pattern with a large selected-area aperture confirms that these carbides are M_3C type of θ phase (*i.e.*, cementite). The Cr concentration is higher than the Mn in almost all carbides next to the FB as seen in Fig. 5, whereas the carbides next to the CDZ have a slightly higher Mn content than Cr, see Fig. 6. The Cr/Mn ratio of the carbides at the interface between the CPZ and CDZ is normally very close to the Cr/Mn ratio in the surrounding matrix. However, it has been observed that when the Cr/Mn ratio is lower than 1.5 in the matrix, carbides with Cr/Mn ratio below 1 can be formed. This can be seen from the extracted line profile that crosses through a Cr nitride, a high Cr/Mn ratio (>1) carbide and a low Cr/Mn ratio (<1) carbide. Tiny nano-particles about a few nm containing mainly Ti are also visible in this area. The number of Mo-rich carbides along the interface between the CPZ and CDZ is notably higher than at the FB.

Nano-particles are also found at the FB in the NG TA material, as shown in Fig. 7. In contrast to the NG AR material, these nano-particles are carbides instead of nitrides. As shown in the N elemental map in Fig. 7(b), only noisy background counts were detected. Moreover, these

carbides belong to Cr-rich and Mn-rich carbides, respectively. The combined maps and line profiles reveal that the compositions are different in these two kinds of carbides. The Mn-rich carbides contain a small Ni content whereas the Cr-rich carbides contain a small amount of Mo. Ni and Mn are clearly segregated at the FB. The SAED pattern along $[113]$ zone axis of the BCC phase shows two additional spots located at $1/3$ and $2/3$ of the BCC reflection $1^{-}21$. The DF image from $1/3$ $1^{-}21$ confirms that the two extra spots are from nano-carbides. It can be indexed as M_3C θ carbides according to Bargaryatskii's orientation relationship [27] between θ and α , *i.e.* $[001]_{\theta} \parallel [011]_{\alpha}$ and $(010)_{\theta} \parallel (211)_{\alpha}$. According to this orientation relationship, for BCC $[113]$ zone axis, the M_3C is close to $[102]$ zone axis with a 3.4° deviation, resulting in only one systematic row along the 010^* direction under this diffraction condition. In other words, in this particular orientation, $[102]_{\theta}$ is about 3.4° away from $[113]_{\alpha}$ and $(060)_{\theta} \parallel (1^{-}21)_{\alpha}$. Similar to the NG AR material, Ti-rich nano-particles with about a few nm size are visible in both BCC and FCC phases. The density of nanometer-sized carbides decreases gradually with increasing distance from the FB. The area containing accumulated nanometer-sized carbides extends >1 μm from the FB in the NG TA material, which is much wider than in the NG AR material.

The CPZ normally extends to around 1.5 μm from the FB in the NG

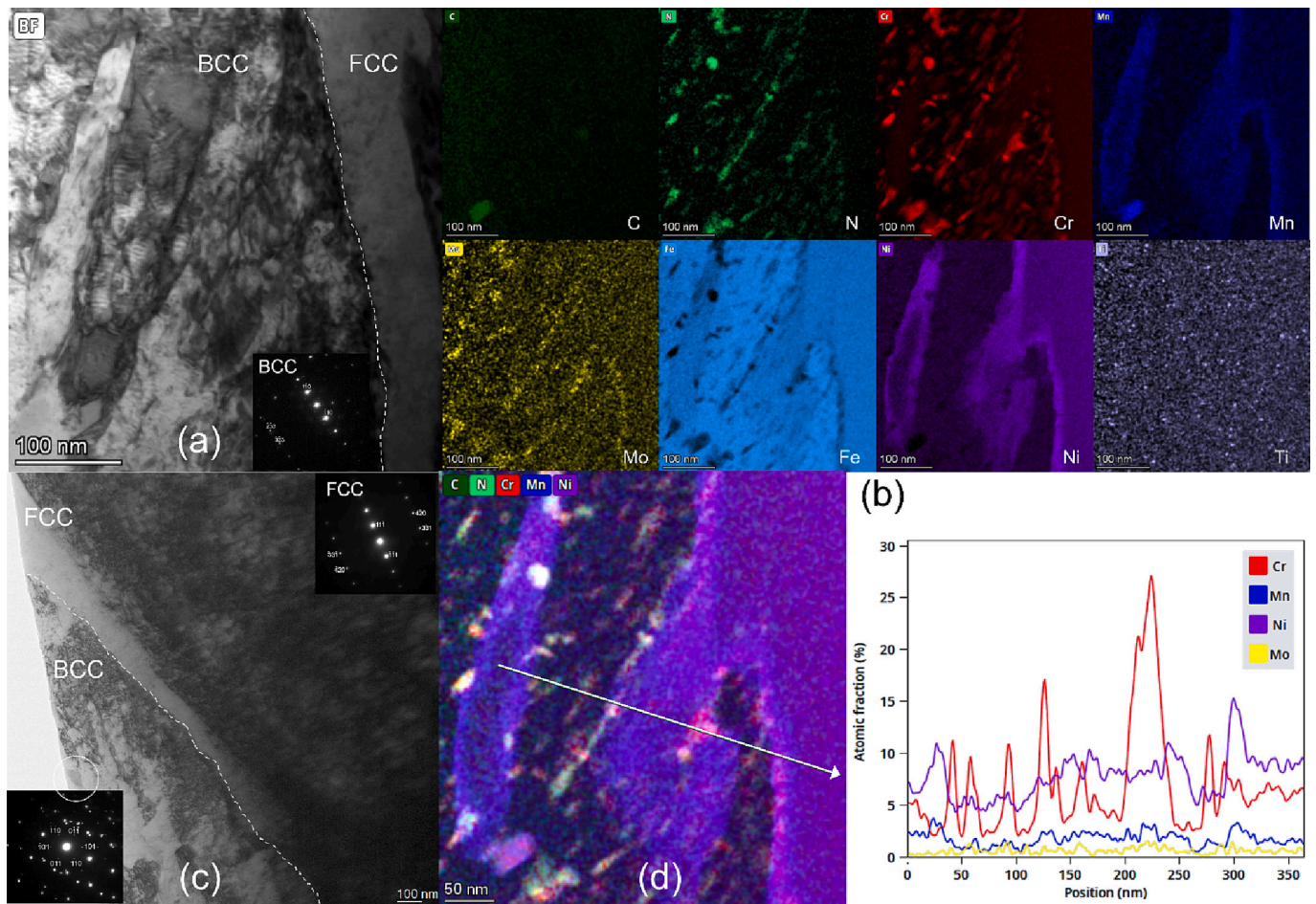


Fig. 5. Carbides at the FB in the NG AR material. (a) STEM BF image and (b) the corresponding elemental maps; (c) TEM BF image and SAED pattern of one large carbide of M_3C type along zone axis $[11\bar{1}]$; (d) Combined carbides and nitrides maps and extracted line profile reveal elemental variation across the FB and nano-sized particles.

TA material. However, when the tempered martensite type of FB was formed instead of a narrow fusion line (as in most cases), the CPZ can be as wide as about $11\ \mu\text{m}$, as revealed by Fig. 8. At the interface of the CPZ and CDZ (next to the tempered martensite type of the FB), the number of carbides significantly decreased and almost disappear in the neighbor CDZ grains, as shown in Fig. 9. Tempered martensite laths with high dislocation density are aligned approximately parallel to the interface in Fig. 9. The tempered martensite laths are full of carbides with higher Cr content than Mn. The dominated carbides in the CPZ are $(Fe, Cr, Mn)_3C$ carbides of M_3C type. However, at the interface of the CPZ and CDZ, the Mn content in the carbides becomes higher than the Cr content and the Cr/Mn ratio in matrix is about 1.5. Nitrides are not found at the interface of the CPZ and CDZ. However, the N map illustrates that the nanometer-sized nitrides formed together with carbides at lath boundaries in the CPZ. Ni-rich particles are also observed in carbides especially at lath boundaries. It is noted that Mo carbides start to form at the interface between the CPZ and CDZ.

3.3. CDZ microstructure and carbide analysis

Fig. 3 and Fig. 4 show that no apparent carbides are visible in the CDZ in SEM images. Due to the limited resolution of SEM, it only indicates that no carbides with size larger than $100\ \text{nm}$ are present. TEM examination of the CDZ area reveals that there are carbides in the CDZ but with much lower density and smaller size compared with carbides near the FB. In contrast to the difference in width of the CDZ, the carbide distribution in the CDZ in the NG AR and NG TA materials is quite

similar, as shown in Fig. 10 and Fig. 11, respectively. In Fig. 10(b) and Fig. 11(b), the observed carbides are mostly Mo carbides with few (Fe, Mn, Cr) carbides located at grain boundaries. It is worth noting that $(Fe, Cr, Mn)_3C$ carbides dominate in the CPZ where the Cr content is higher than that of Mn. However, for the $(Fe, Mn, Cr)_3C$ carbides in the CDZ, the Mn content is much higher than that of Cr. The line profile of the carbides shows that the Cr content in the carbides is just slightly higher than in the matrix. The size of $(Fe, Mn, Cr)_3C$ carbides in the CDZ are normally $\leq 50\ \text{nm}$ and the size of the Mo carbides is mostly only a few nanometers.

3.4. HAZ microstructure and carbide analysis

From the CDZ to the HAZ (outside the CDZ), the carbide population increases dramatically. The microstructure and carbide distribution in the HAZ of the NG AR and the NG TA materials are illustrated in Fig. 12. SEM images show two kinds of grains, *i.e.* grains with excess carbides and grains lacking apparent carbides. High-resolution TEM reveals that these grains lacking apparent carbides may contain nano-sized carbides. It is worth to note that the fraction of grains devoid of visible carbides in the HAZ is 2–3 times higher in the NG TA material than in the NG AR material. The STEM image of Fig. 12(d) shows a few long fiber-like carbides aligning in same direction, with the longest one up to $2\ \mu\text{m}$ in length, which is a magnitude longer than in Fig. 12(b). It seems that these long carbides were formed during thermal aging.

The TEM-EDS elemental maps in Fig. 13 illustrate the morphology and distribution of carbides in the HAZ of the NG AR material, where

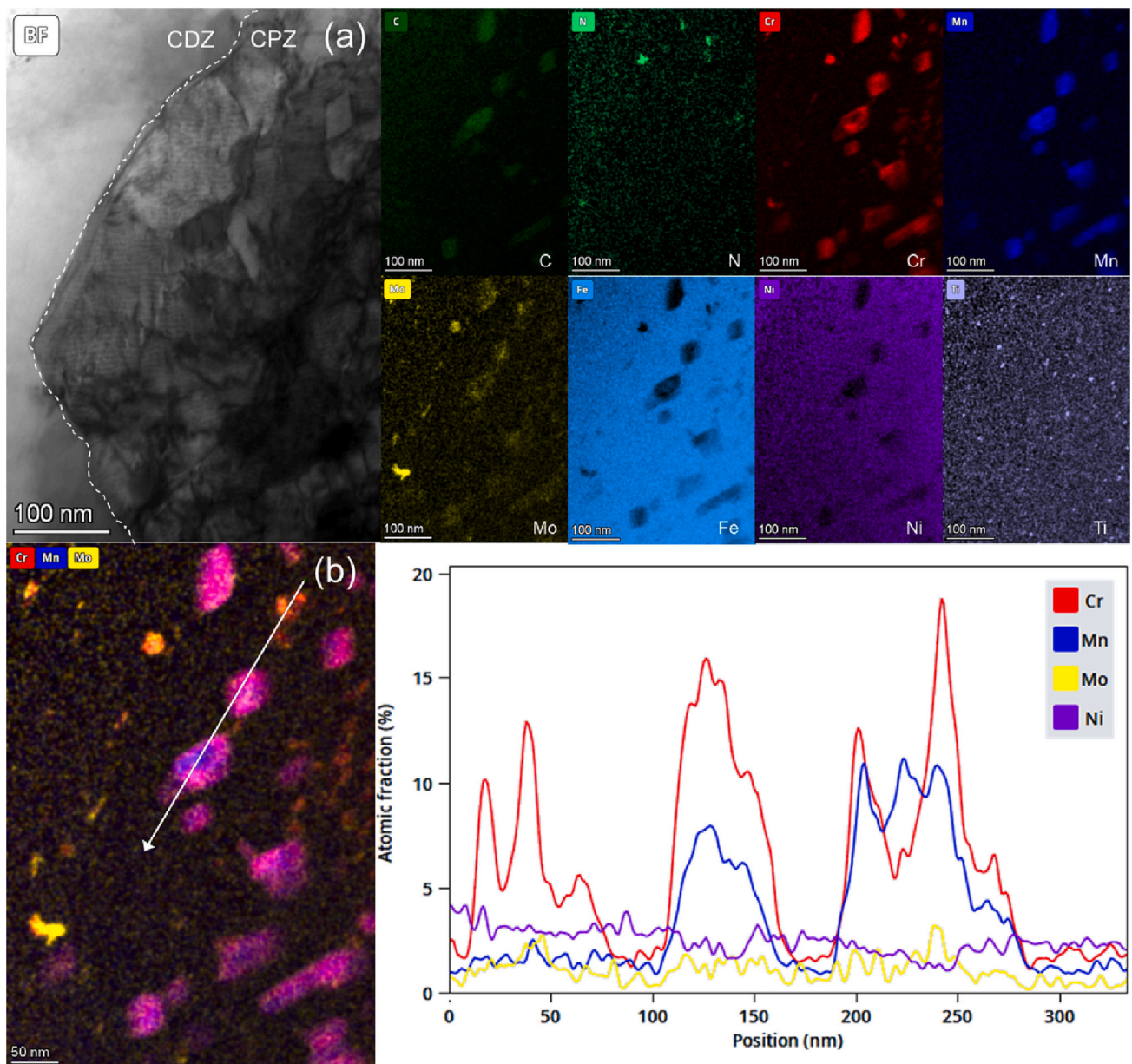


Fig. 6. Carbides at the interface of CPZ and CDZ in the NG AR material. (a) STEM BF image and corresponding elemental EDS map; (b) Combined Cr, Mn and Mo maps and extracted elemental profile from the line marked in the color map.

excess carbides can be found both at grain boundaries and within grains. There are two size groups of carbides, *i.e.*, relatively small carbides and relatively large carbides in the HAZ. The dominant and large-size carbides range from tens to hundreds of nanometers. They have a round or ellipsoidal shape and are found both at grain boundaries and within grains. The elemental maps and the extracted line profile in Fig. 13 reveal that the large carbides are (Fe, Mn, Cr)₃C carbides with the content of Mn being much higher than the Cr content. Only occasionally, carbides with Cr content higher than Mn are observed (few carbides containing high-Cr core particles). The relatively small carbides are Mo-rich carbides. The majority of the Mo carbides are located at grain boundaries and their size is about a few tens of nm. Fig. 13 reveals additionally Al–Si nano-sized particles with a few nm to a few tens of nm in size. The SAED in Fig. 13(b) consists of two phases, the major reflections from BCC along [102] zone axis and the weak spots from Mo₂C along [100] zone axis. A few Mo₂C particles are illustrated in the DF image with Mo₂C 002⁻ reflection.

To investigate the crystal structure of the (Fe, Mn, Cr)₃C carbides in

the NG AR material, one large and isolated particle was tilted along the zone axis [11⁻0], which confirmed the M₃C crystal structure in Fig. 14. The DF image from the reflection of 1⁻1⁻1 reveals a low angle boundary in the particle. The lattice parameters deviated slightly from the lattice of stoichiometric Fe₃C.

The chemical composition of the long fiber-like carbides with a length up to 2 μm in the HAZ of the NG TA material is presented in the TEM EDS mapping in Fig. 15. They are (Fe, Mn, Cr)₃C carbides with a Cr content slightly higher than the matrix. The extracted line profile shows that the width of these carbides is between 50 and 100 nm. Most of the Mo carbides are a few tens of nm in size but a few of them are needle-like and extend over 100 nm. Such needle-like Mo carbides are not observed in the NG AR material.

SAED patterns from two separated carbides in the HAZ of the NG TA sample examined with different zone axes are presented in Fig. 16(a,b). Both zone axis patterns can be indexed with M₃C lattice and the lattice parameters agrees perfectly with stoichiometric Fe₃C. Fig. 16(c) illustrates a high-resolution fringe image of one Mo carbide and its fast

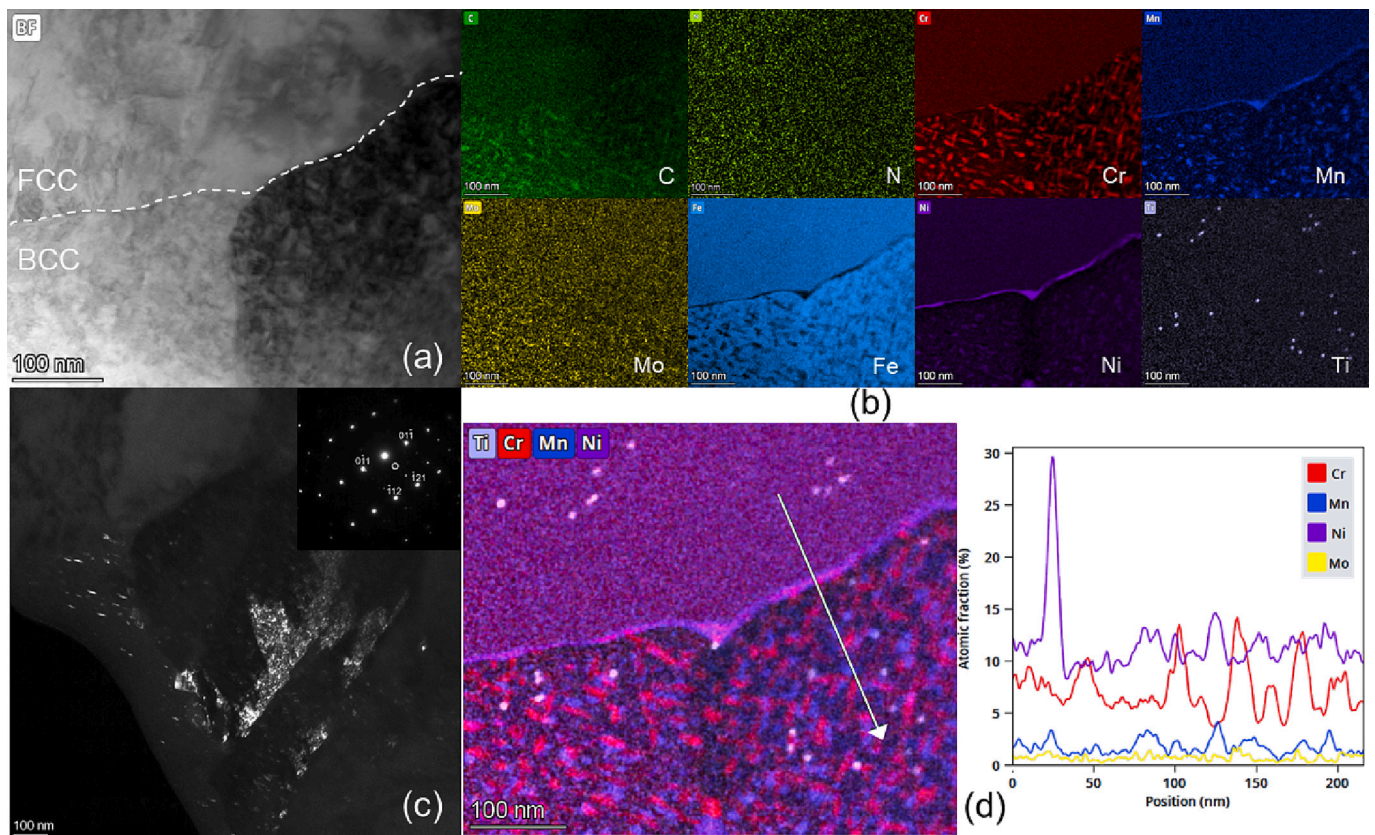


Fig. 7. Nano-carbides at the FB in the NG TA material. (a) STEM-BF image and (b) the corresponding elemental map; (c) TEM DF with nano-carbides' reflection from SAED pattern along zone axis [113]; (d) The color-mixed elemental map and extracted profile with line position indicated in the map.

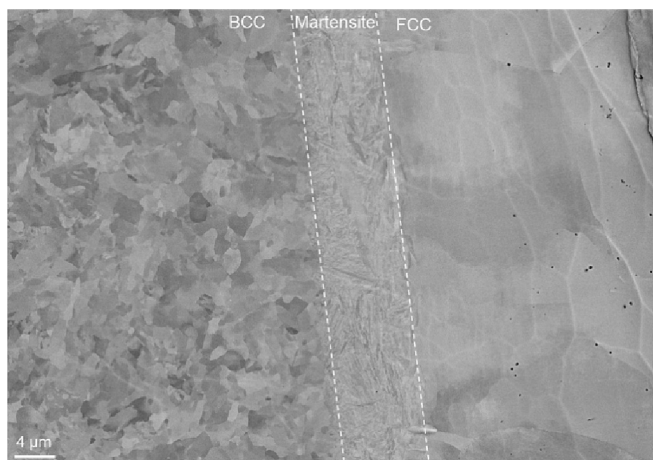


Fig. 8. The NG TA material contains a martensite area between the FCC (right) phase and BCC phase with a width of about 11 μm .

Fourier transform (FFT), which can be indexed with Mo_2C crystal of orthorhombic lattice along the [110] zone axis.

3.5. WAXS of carbides in the HAZ

The Rietveld refinement results of WAXS patterns are presented in Fig. 17. The X-ray diffraction pattern confirms the two types of carbides observed in TEM, M_3C and Mo_2C . The AR and TA patterns are quite similar in general and contain approximately 2% carbides. However, the TA pattern shows slightly larger volume fraction of carbides than the AR pattern. After thermal aging the ratio of M_3C carbides increased in the

NG TA material compared to the NG AR material. In TEM observations of the TA material, there is a higher amount of Mo_2C carbides than in the AR material, but WAXS refinement has shown slightly higher Mo_2C fraction in the AR material. The controversy results are mainly because the nano-sized Mo_2C has weak broad peaks and its fraction is at the detection limit of WAXS.

3.6. APT analysis

The effect of thermal aging on the potential P segregation in the LAS HAZ was studied with APT. Comparing the P content on grain boundaries using APT is a challenging task, as the APT data is very local with a small analysis volume. Analyzing a specific grain boundary is not enough, as different types of grain boundaries often contain different amounts of segregation [28]. Thus, a full characterization of the type of grain boundary (including electron backscatter diffraction and transmission Kikuchi diffraction) would be needed, and a large number of grain boundaries need to be analyzed in order to get a statistically significant result. This approach is thus very time consuming and work intense. In this paper, another path was chosen. This was to compare the average amount of the element concentration in the interior of the HAZ grains from multiple APT samples. If the segregation after thermal aging is strong enough, the bulk P content in the interior of the grains would be lower in the NG TA material than in the NG AR material.

The APT analyses of the HAZ bulk of the AR and TA materials contained no grain boundaries. The average bulk compositions measured from multiple APT analyses can be seen in Table 3. The P contents are low, 50 ± 20 at.ppm and 40 ± 20 at.ppm in the AR and TA materials, respectively. Though the bulk P content in the interior of the HAZ grains are slightly lower in the NG TA material than in the NG AR material, there is no evidence of a significant P segregation to grain boundaries from thermal aging.

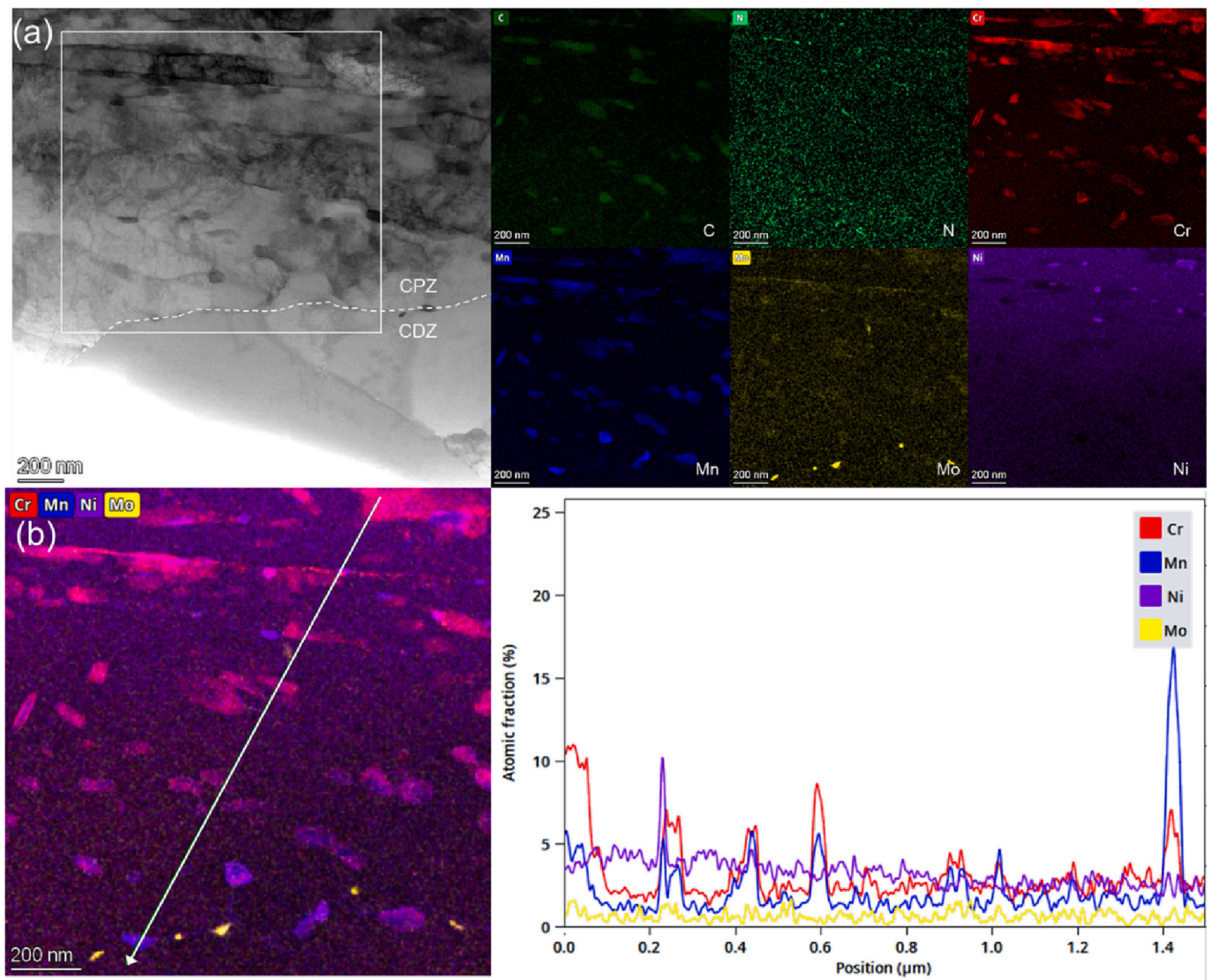


Fig. 9. Carbides at the interface of the CPZ and CDZ in the NG TA material. (a) STEM BF image and corresponding elemental map of framed area in BF image. (b) Combined Cr, Mn, Ni and Mo maps and extracted profile for the line indicated in color-mixed image.

In Fig. 18, representative reconstructions of AR and TA materials are shown. In these analyses, occasional dislocation lines are present. These can be observed by APT due to the enrichment of Mo, Mn and C. Statistically, there is also a small tendency for P to segregate to these dislocation lines. However, no difference in P segregation to dislocation lines between the NG AR and TA materials could be proven by the APT measurements.

In the NG AR material, a part of a carbide was analyzed by APT. The carbide contains mainly Fe (59 at.%) and Mn (14 at.%) as metallic elements. Mo and Cr were also enriched in the carbide (both by <2 at.% each). The C content was measured to be 24 at.%, but might be slightly underestimated due to cascades of C atoms evaporating simultaneously during APT analysis and detector deadtime [29]. In connection to this carbide, a low-angle boundary enriched in C and P is observed. This shows that there is probably a certain level of P segregation on boundaries already before long-term thermal aging. The bulk P content is around 90 at.ppm (50 wt.ppm), see Table 2, so the APT measurements suggest that about half of the P is segregated already before aging.

4. Discussion

The microstructure and carbide size distribution from different

regions in LAS of the NG AR and NG TA materials are summarized in Table 4. At the FB, nanometer-sized precipitates were observed. In the NG TA material these are nano-carbides. However, in the NG AR material, the majority of the nano-precipitates at the FB (tens of nanometers wide zone) are nitrides whereas nano-carbides dominate in regions slightly further away from the FB. These nano-carbides at the FB of the NG TA material have a perfect Bargaryatskii's orientation relationship with the BCC matrix, which is reported for the first time in a DMW, according to the knowledge of the authors. The orientation relationship between nanometer-sized carbides with the BCC matrix indicates that they precipitated directly on the crystal defects of ferrite matrix during PWHT.

Long-term thermal aging triples the width of the CPZ. In the CPZ, the number of carbides is much lower and the size of the carbides is also smaller in the AR material than in the TA material. This is in line with the result that the long-term thermal aging increases the microhardness peak close to the FB. Except nano-sized nitrides/carbides at the FB, the dominant carbides in the CPZ are $(\text{Fe, Cr, Mn})_3\text{C}$ with size about 50–100 and 100–200 nm in the NG AR and NG TA materials, respectively. The CPZ contains the highest density of intergranular and intragranular $(\text{Fe, Cr, Mn})_3\text{C}$ carbides in all regions of the LAS side. Even though $(\text{Fe, Cr, Mn})_3\text{C}$ carbides also contain a small amount of Mo, the Mo_2C carbides

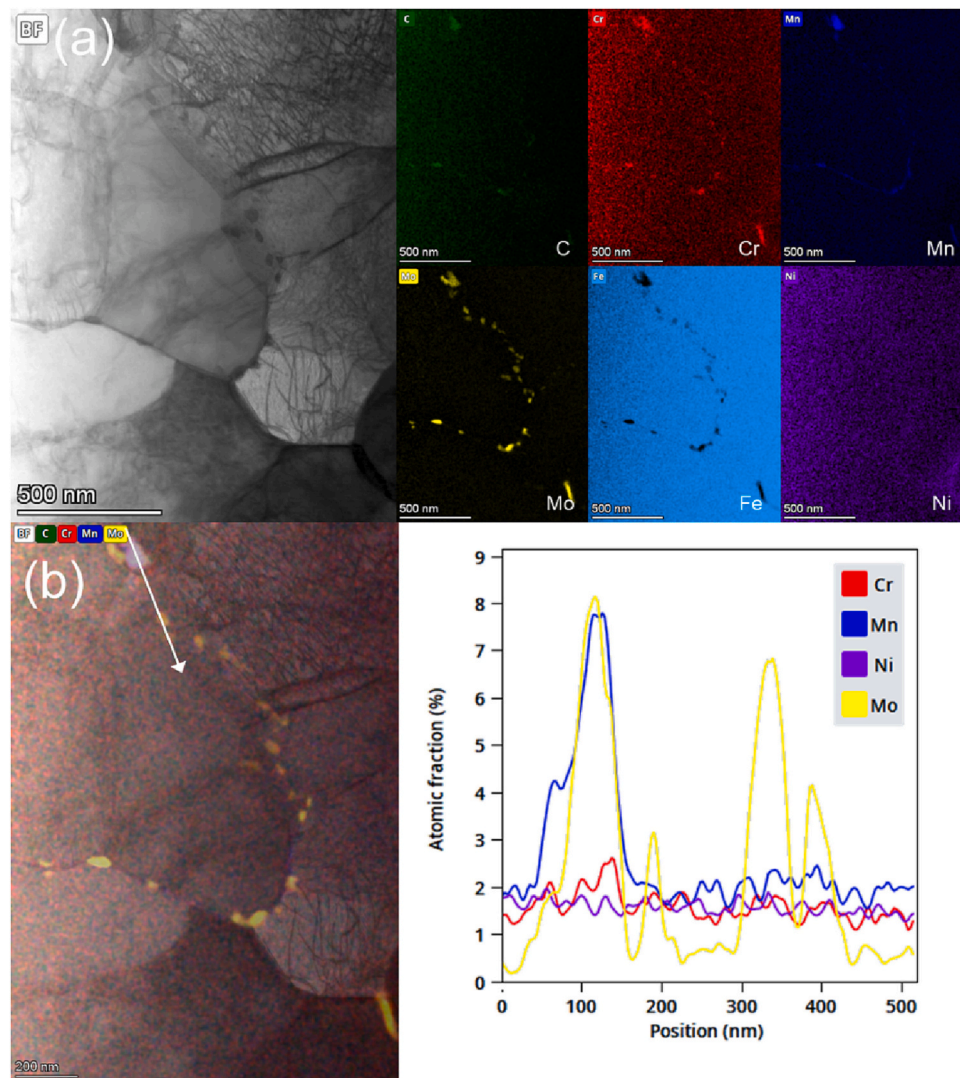


Fig. 10. Carbides in the CDZ in the NG AR material. (a) STEM BF image and corresponding elemental maps; (b) Mixed of BF image and C, Cr, Mn, and Mo elemental maps and the extracted profile from line marked in the mixed image.

population is very small in the CPZ. It is interesting to note that Mo_2C carbides are frequently observed at the interface between the CPZ and CDZ. These features of CPZ are common in both the AR and TA materials even when a wide CPZ was formed associated with a tempered martensite type of FB. The columnar grains in the narrow CPZ are similar to the lath grains in the tempered martensite since they may be formed with the same mechanism resulting from high cooling rate at FB.

Long-term thermal aging slightly reduces the width of the CDZ. This indicates a continuous diffusion of carbon from the CDZ to the CPZ during thermal aging. The grain size is much smaller and the dislocation density is higher in the CPZ than in the CDZ. The carbide population is the smallest in the CDZ compared to the CPZ and the HAZ. Only small-sized Mo_2C carbides decorating mainly the grain boundaries can be found in the CDZ. Occasionally, few $(\text{Fe}, \text{Mn}, \text{Cr})_3\text{C}$ carbides can be found at grain boundaries too. In the CDZ, $(\text{Fe}, \text{Mn}, \text{Cr})_3\text{C}$ carbides contain higher Mn content than Cr, which is different to the CPZ where $(\text{Fe}, \text{Cr}, \text{Mn})_3\text{C}$ were formed with higher Cr content than Mn.

The carbide density in the HAZ is evidently higher than in the CDZ but lower than in the CPZ. In the LAS HAZ, carbides were identified as $(\text{Fe}, \text{Mn}, \text{Cr})_3\text{C}$ and Mo_2C . Long-term thermal aging coarsens the carbides size in the HAZ (up to a magnitude longer), which corresponds well to the WAXS measurement in the HAZ where higher percentage of carbides was observed in the TA than the AR material. The fraction of

carbide-free grains in the HAZ is 2–3 times higher in the NG TA material than in the NG AR material. These grains devoid of visible carbides are formed likely during phase transformation where C partitioning occurred.

The welding technique (e.g., NG or buttering) has a significant effect on the solidification, cooling rate, internal stresses and mixing of metals, impacting the forming solidification microstructure and the carbides at the FB in a DMW [30] [31]. However, the data on the microstructural changes and carbide formation in plant-relevant NG DMW occurring upon post-weld heat treatment and long-term thermal aging is very limited. The microstructure and carbides in the FB and HAZ regions have a direct influence on the local brittle fracture behavior and on the cracking susceptibility of a DMW [13]. During long-term thermal aging in the NG mock-up, more carbon from the LAS side can diffuse from the CDZ to the FB [1]. As shown in this work, long-term thermal aging leads to moderate changes in the microstructure and carbides in the FB, CPZ, CDZ and HAZ regions in the NG DMW. The peak hardness of the NG DMW was reported to coincide with the position of carbon peak values [3] [5], which is in line with the microhardness measurement carried out at two different loads and the quantitative analysis of C concentration across the FB by WDS. In this work higher microhardness peak closer to the FB and wider CPZ/narrower CDZ in the TA material were observed. Ahonen et al. [5] reported a lower microhardness after

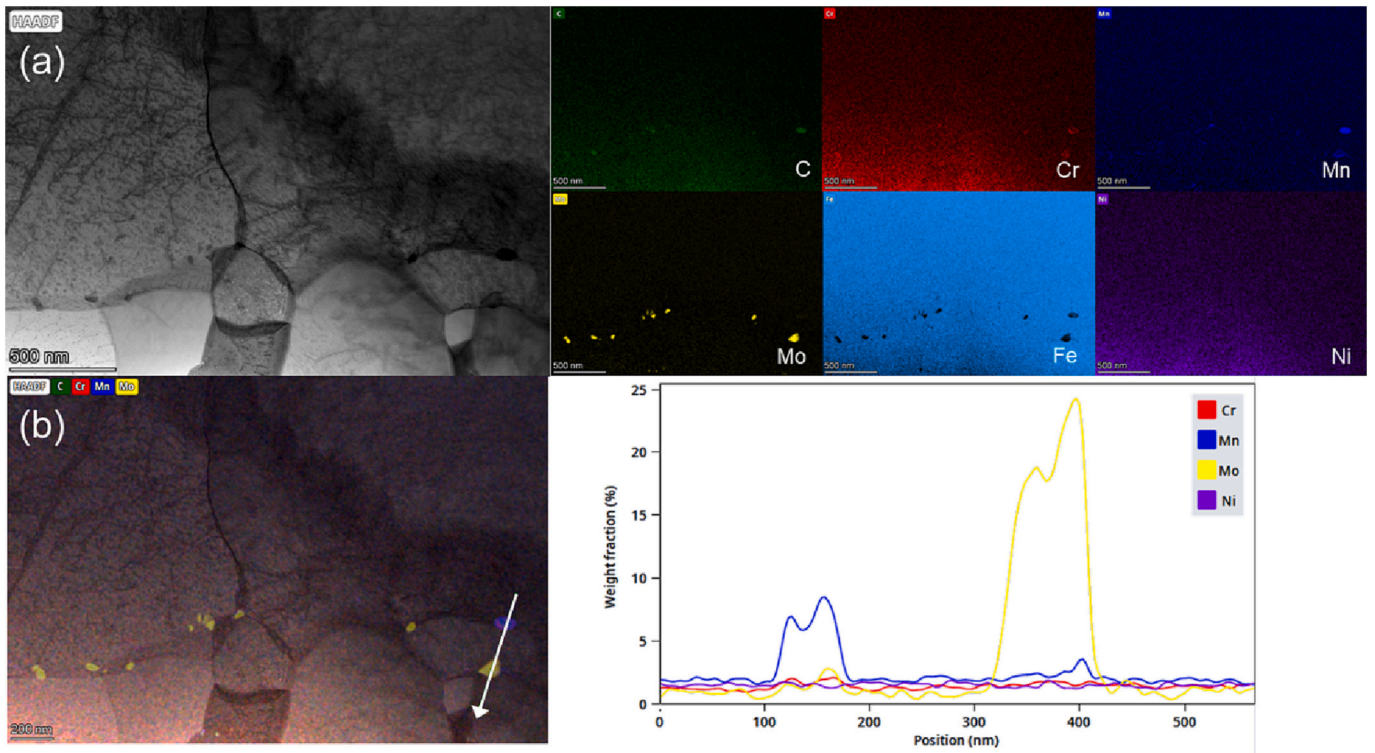


Fig. 11. Carbides in the CDZ of the NG TA material. (a) STEM BF image and corresponding elemental maps; (b) Mix of BF image and C, Cr, Mn, and Mo elemental maps and the line profile from the arrow line in the mixed image.

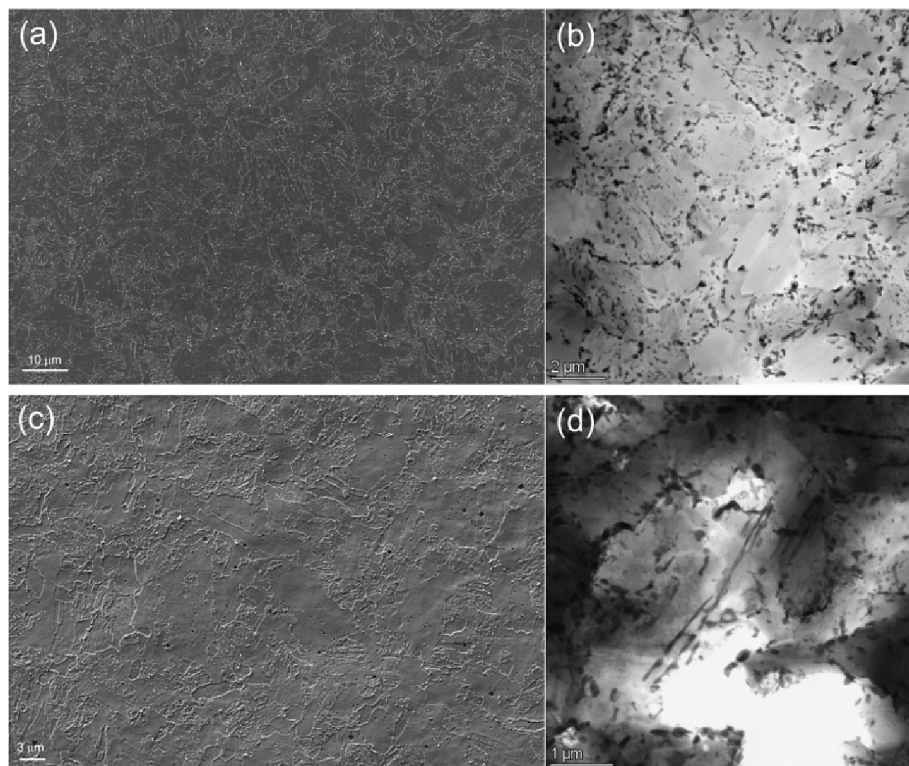


Fig. 12. Microstructure and carbide distribution in the HAZ of (a-b) the NG AR and (c-d) the TA material. (a,c) SEM SE images and (b,d) STEM BF images.

thermal aging. However, the difference in the peak hardness mainly derives from the indentation parameters particular the spacing between the first indents to the FB.

Nevasmaa et al. [32] reported that a decrease in fracture resistance

of DMW can stem from increased metallurgical constraint and crack (growth) driving force accentuated by the high, local mismatch state, coupled with inherent local inhomogeneity of the near-interface regions. Under high local strength mismatch, the inherent strength and

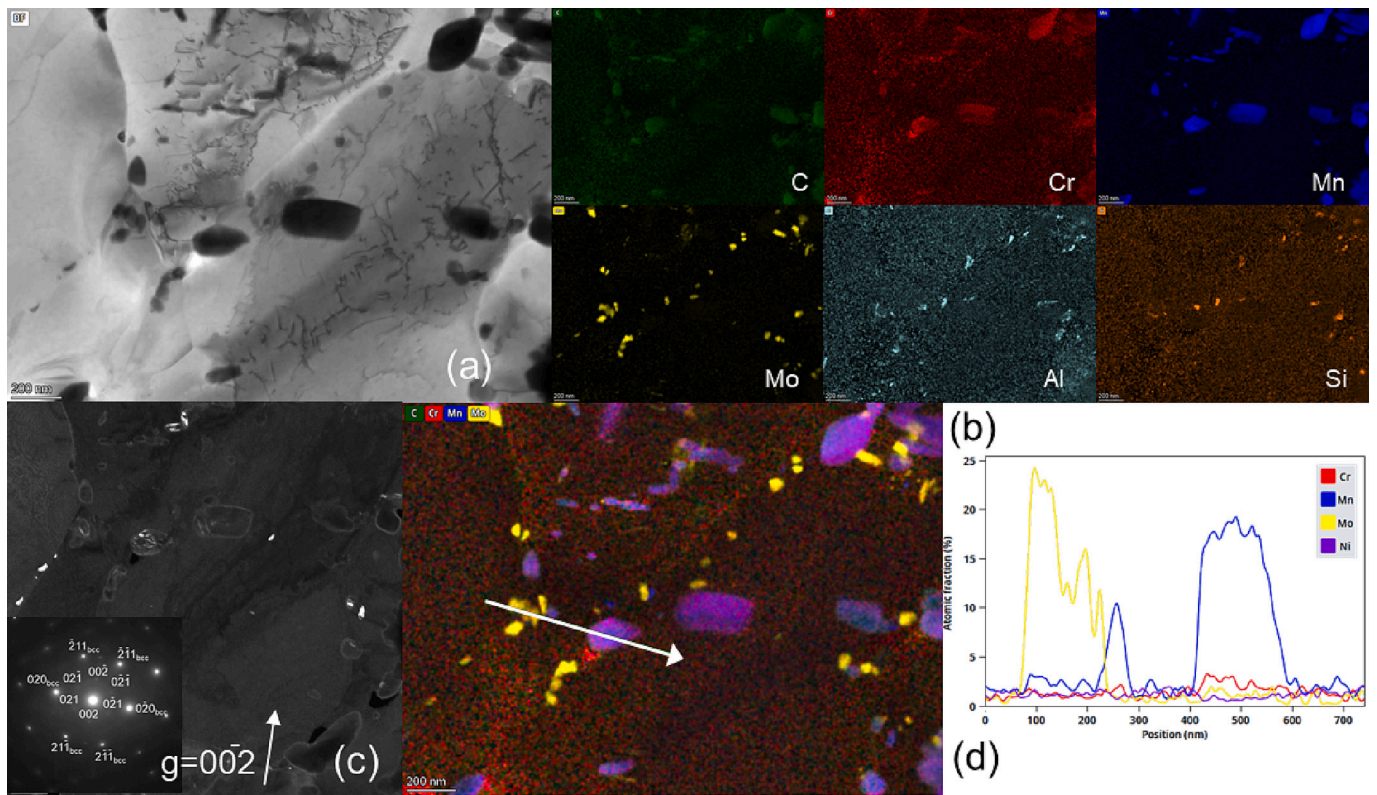


Fig. 13. Carbides in the HAZ of the NG AR material. (a-b) STEM-BF image and selected elemental maps; (c) TEM DF image from Mo_2C 's reflection 002^- with the inset SAED pattern indexed with BCC zone axis $[102]$ and Mo_2C zone axis $[100]$; (d) Mix of selected elemental maps and extracted line profile.

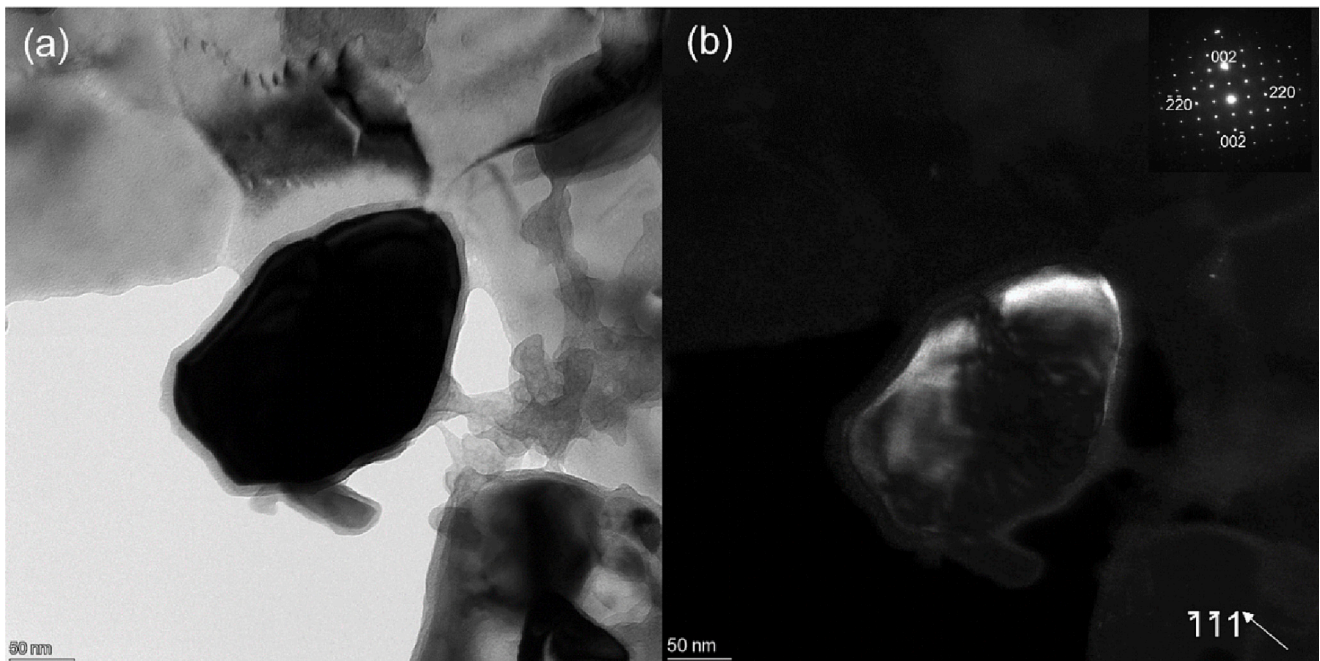


Fig. 14. TEM BF image (a) and DF image (b) along the $[11\bar{0}]$ zone axis in the HAZ of the NG AR sample with the inset being the SAED pattern.

toughness properties of two neighboring, mismatching microstructures become increasingly important, which may, in some cases, dictate the entire fracture behavior of a DMW. As observed in this study, long-term thermal aging results in higher microhardness mismatch at the FB, larger/denser carbides in the CPZ and longer carbides and higher fraction of carbide-free grains in the HAZ, which may lead to the formation

of local brittle zones and can cause low fracture toughness. The brittle fracture behavior of the same mock-up studied in this paper was recently reported by Lindqvist et al. [22]. It was found that for four T_0 fracture toughness specimens aged at 400°C for 15,000 h, the crack initiation and propagation occur only in the HAZ without deviating to the FB, leading to a much lower ($\sim 1/3$) average fracture toughness compared to

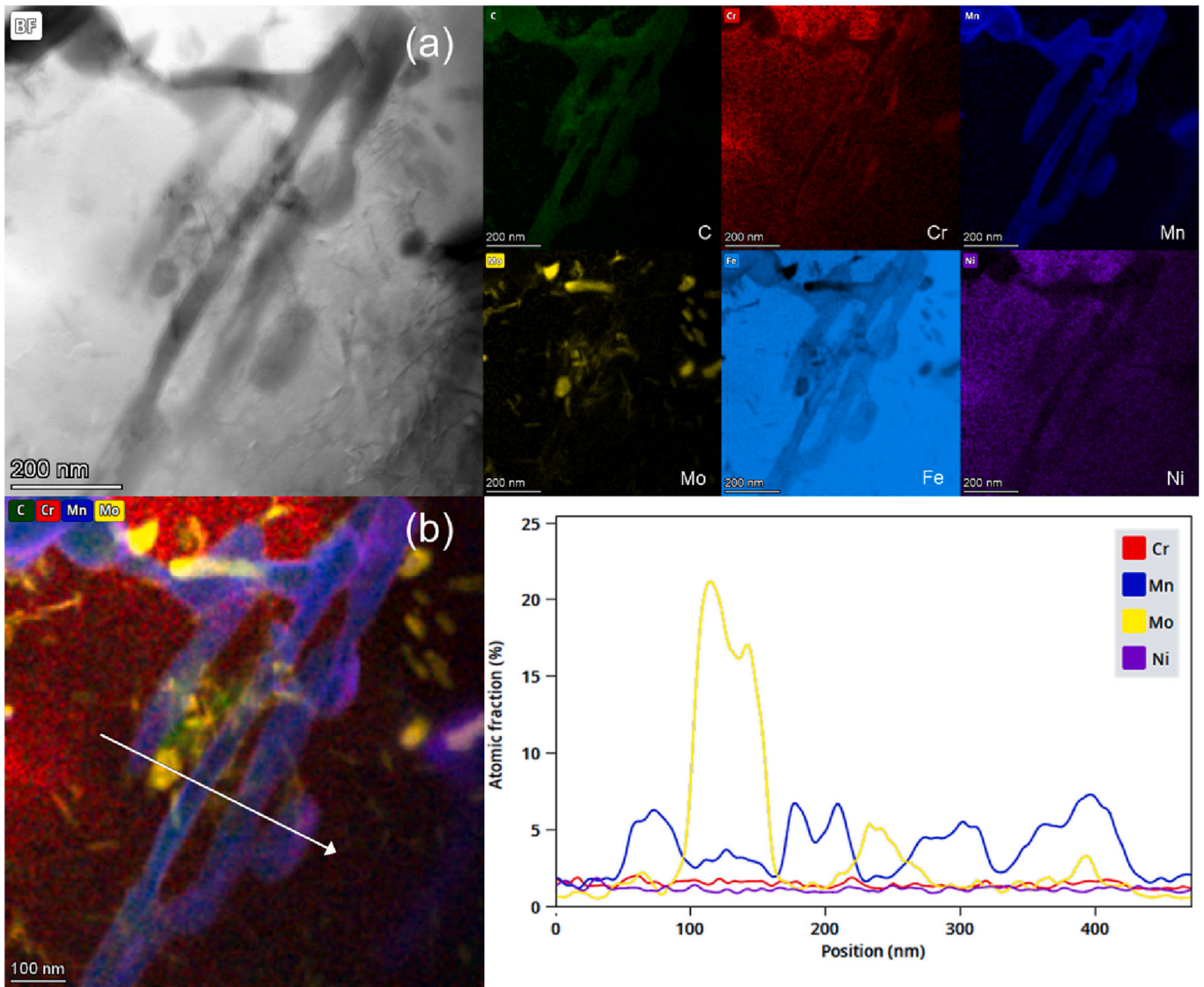


Fig. 15. Carbides in the HAZ of the NG TA material. (a) STEM-BF image of carbides and corresponding selected elemental maps; (b) combined elemental map and extracted line profile from the line position indicated in the image.

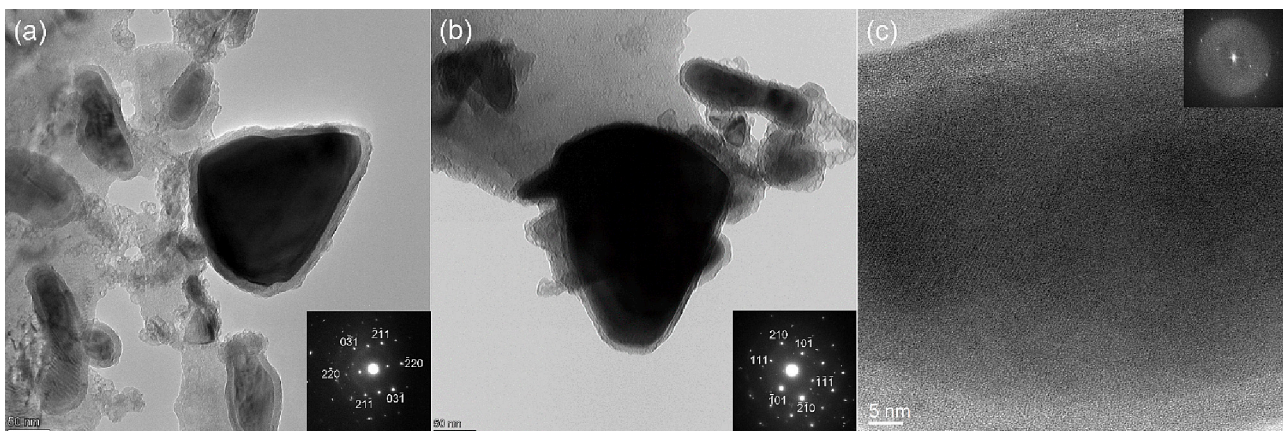


Fig. 16. TEM image of Fe carbides and Mo carbides in the HAZ of the NG TA sample. (a) TEM BF image of Fe carbide along the $[113]$ zone axis; (b) TEM BF image of Fe carbides along $[12\bar{1}]$; (c) HRTEM of a Mo carbide with the inset of its FFT, which fits to zone axis $[110]$.

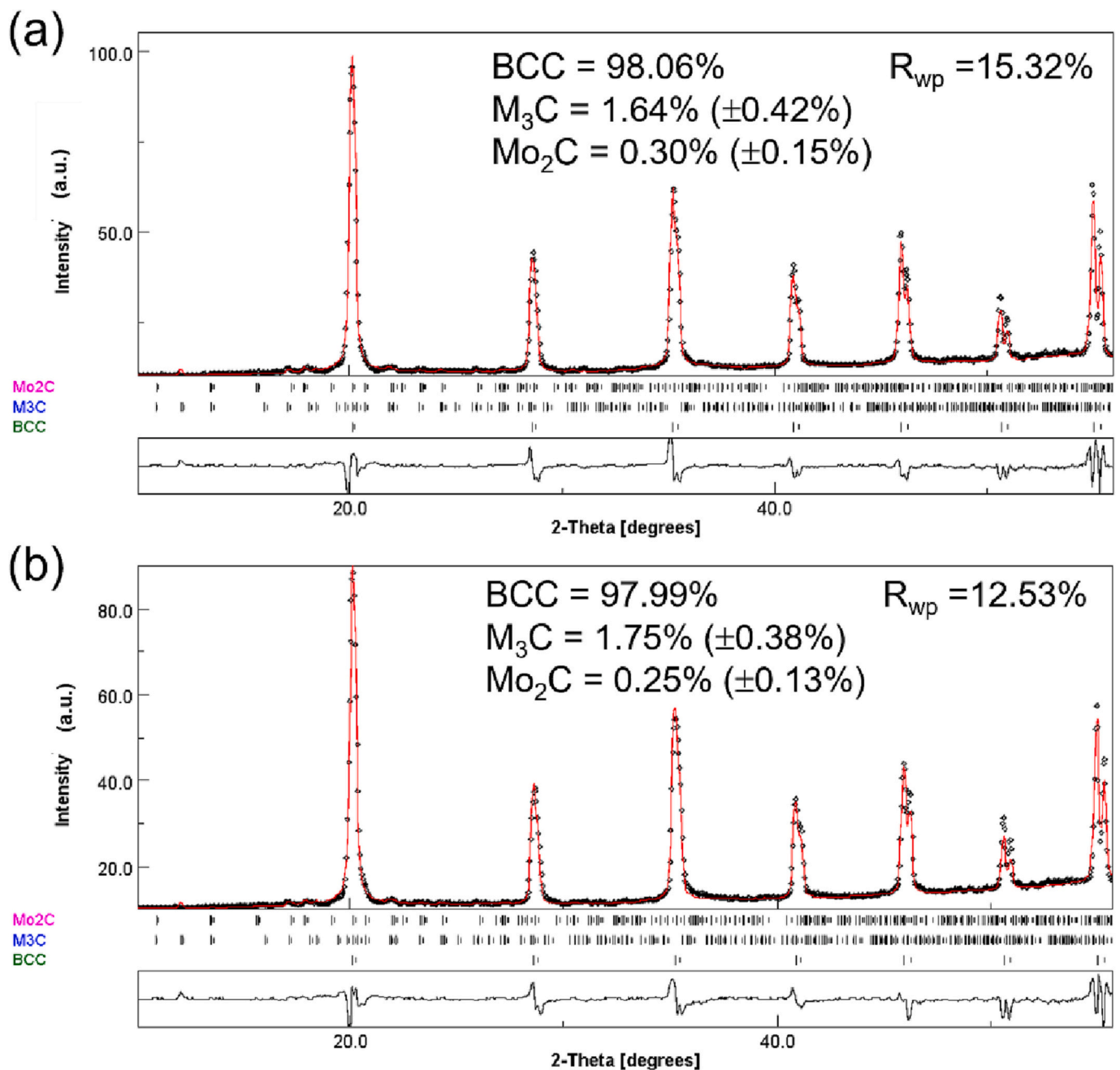


Fig. 17. WAXS patterns of (a) the NG AR material and (b) NG TA material.

the other specimens with the notch crack placed in the CDZ and the crack path deviation to the FB. The thermal aging and the resultant formation of local brittle zones, e.g. coarsening carbides and higher fraction of carbide-free grains in the HAZ may contribute to the observed low fracture toughness.

The APT results suggest that in the studied DMW mock-up with low bulk phosphorus no significant phosphorus segregation was observed and about half of the phosphorus is segregated already before aging. Though a slightly higher amount of grain boundary cracking has been seen in the master curve test specimens after thermal aging, which can be assumed to be due to phosphorus segregation, the amount of phosphorus segregation is not significant, as is the shift in T_0 [22] [23], which is in line with the APT results in this paper. Moreover, the thermal aging at 400 °C for 15,000 h results in a lower shift of T_0 than that of impact toughness. Therefore, the thermal aging and the resultant microstructural changes and carbides formation affect more the crack

arrest and propagation mechanism than the initiation mechanism.

In the majority of the DMW literature, the carbides were referred to as chromium carbide precipitates without detailed information of the chemistry and crystal structure or indexed as $Cr_{23}C_6$ [3] [12] [19] [33]. Choi et al. [12] reported that $Cr_{23}C_6$ precipitated at the FB immediately after DMW welding and the number of $Cr_{23}C_6$ precipitates in the FB regions increased after thermal aging for 1713 h at 400 °C. However, the number of precipitates decreased by the coarsening and coalescence of precipitates with a thermal aging of 3427 h. In this paper, thermal aging at 400 °C for 15,000 h results in both a number increase and coarsening of precipitates at the FB, CPZ and HAZ. This will result in an increase of contact surface between the LAS (anode) and Cr-rich precipitates (cathode) and then cause the increase of the corrosion rate if the DMW is exposed to high-temperature water. In the present study the dominant carbides are M_3C θ carbides verified by index under multiple zone axes and $M_{23}C_6$ was not detected in any of our TEM samples. One possible

Table 3

Compositions of the interior of the grains in the HAZ of the NG AR and TA materials from APT. The error given is the standard deviation between the APT runs used, indicating small local differences in the composition, resolved by APT.

—	TVO AR	TVO TA
	At.%	At.%
Fe	Bal.	Bal.
Mn	1.08 ± 0.24	1.11 ± 0.44
Ni	0.79 ± 0.04	0.76 ± 0.02
Si	0.42 ± 0.02	0.42 ± 0.01
Mo	0.22 ± 0.04	0.19 ± 0.10
Cr	0.23 ± 0.08	0.22 ± 0.04
Cu	0.035 ± 0.003	0.034 ± 0.005
N	0.03 ± 0.04	0.05 ± 0.01
Co	0.02 ± 0.01	0.01 ± 0.01
C	0.16 ± 0.18	0.04 ± 0.04
Al	0.005 ± 0.003	0.020 ± 0.019
P	0.005 ± 0.002	0.004 ± 0.002
V	0.002 ± 0.001	0.002 ± 0.002

reason is that the chemical composition, cooling rate, temperature gradient and PWHT affect the FB carbide type. Another reason can be due to the similarity of a few high index zone axes in electron diffraction patterns with the minor differences in closed pack plane distance between BCC and FCC lattice at the FB, which may have caused mis-indexation in literatures.

5. Conclusions

The microstructure and carbides' crystal structure, chemistry, morphology and size in the FB and the LAS HAZ were analyzed for the NG SA508/Alloy 52 DMW mock-up, which is fully representative of an actual nuclear component. Based on the obtained results, the following conclusions can be drawn:

- The nanometer-sized precipitates at the FB are nano-carbides in the NG TA material and nano-nitrides in the NG AR material. These Cr/Mn-rich carbides at the FB have a fixed Bagaryatskii orientation relationship with the BCC matrix, which is reported for the first time in a DMW.
- Long-term thermal aging increases the microhardness peak (~20 HV) close to the FB and triples the width of the CPZ. In the CPZ, the

number of carbides is much lower and the size of the carbides is smaller in the AR material than in the TA material.

- The dominant carbides are (Fe, Cr, Mn)₃C in the CPZ but (Fe, Mn, Cr)₃C in the CDZ and the HAZ. These carbides are M₃C θ carbides.
- Long-term thermal aging coarsens the carbide size in the HAZ. The length of the carbide can be a magnitude longer after aging. The fraction of grains devoid of visible carbides in the HAZ is 2–3 times higher in the NG TA material than in the NG AR material.
- After thermal aging, the higher microhardness mismatch at the FB, the larger/denser carbides in the CPZ and the coarsened carbides and higher fraction of carbide-free grains in the HAZ may lead to local brittle zones and could cause low fracture toughness.
- There is no evidence of a significant phosphorus segregation to grain boundaries in HAZ due to thermal aging.

Declaration of Competing Interest

The authors declare that they have no known competing financial interests or personal relationships that could have appeared to influence the work reported in this paper.

Table 4

Summary of grain size and carbide distribution in LAS of AR and TA materials.

		CPZ	CDZ	HAZ
Zone width	AR	≤500 nm ≥1500 nm	50 μm	N/A
	TA	Or ~ 11 μm (tempered martensite FB)	40 μm	N/A
Grain size	AR	100–300 nm	4.2 μm	1.2 μm
	TA	100–300 nm	4.0 μm	1.4 μm
Carbide type and size	AR	Nano-sized nitrides: ≤10 nm; (Fe, Cr, Mn) ₃ C: ≤100 nm	Mo ₂ C: ≤40 nm; (Fe, Mn, Cr) ₃ C: ≤150 nm	(Fe, Mn, Cr) ₃ C: ≤300 nm; Mo ₂ C: ≤100 nm
	TA	Nano-sized carbides: ≤20 nm; (Fe, Cr, Mn) ₃ C: ≤200 nm	Mo ₂ C: ≤80 nm; (Fe, Mn, Cr) ₃ C: ≤150 nm	(Fe, Mn, Cr) ₃ C: ≤2 μm (fiber) Or ≤ 300 nm (round); Mo ₂ C: ≤100 nm
Carbide density	AR	Higher than in HAZ	Much lower than in HAZ	Similar to normal reactor pressure vessel steel
	TA	Higher than AR	Similar to AR	Higher than AR

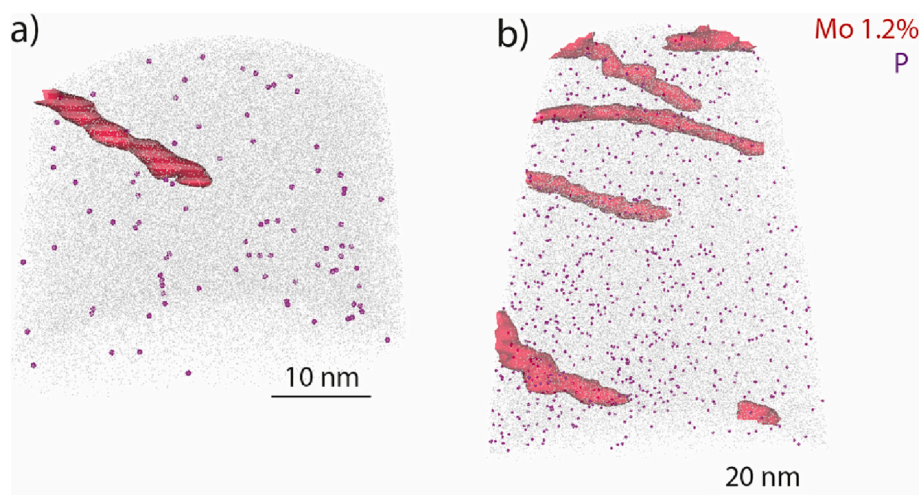


Fig. 18. APT reconstructions of (a) NG AR and (b) NG TA material. Purple dots correspond to P atoms, and red surfaces to 1.2% Mo (isoconcentration surfaces), delineating Mo enrichment at dislocations. Grey shows the extent of the analyses. (For interpretation of the references to color in this figure legend, the reader is referred to the web version of this article.)

Data availability

The data that support the findings of this study are available from the corresponding author upon reasonable request.

Acknowledgements

The authors wish to express their gratitude for the funding and support from Ringhals AB, OKG AB, Teollisuuden Voima Oyj and VTT Technical Research Centre of Finland within the FEMMA (Forum for the Effect of Thermal Aging and Microstructure on Mechanical and EAC Behavior of Ni-based Alloy Dissimilar Metal Welds) research project. The authors also thank NKS for funding the NKS-FEMMA (AFT/NKS-R (22)134/4) project. The authors would like to thank P. Arffman, J. Lydman, J. Lukin and L. Sirkiä for the experimental contributions. The authors would like to thank U. Ehrnstén, P. Efsing, B. Forssgren, H. Reinvald and H. Hänninen for suggestions and discussions. The authors acknowledge the provision of facilities and technical support by Aalto University at OtaNano - Nanomicroscopy Center (Aalto-NMC). The APT experiments were performed at Chalmers Materials Analysis Laboratory (CMAL).

References

- [1] M. Ahonen, S. Lindqvist, T. Sarikka, R. Mougnot, E. Leskelä, J. Lydman, U. Ehrnstén, P. Nevasmaa, T. Seppänen, P. Arffman, H. Hänninen, Thermal ageing and mechanical performance of narrow-gap dissimilar metal welds, *VTT Technol.* 333 (2018).
- [2] W.-C. Chung, J.-Y. Huang, L.-W. Tsay, C. Chen, Microstructure and stress corrosion cracking behaviour of the weld metal in alloy 52-A508 dissimilar welds, *Mater. Trans.* 52 (1) (2011) 12–19.
- [3] A. Akhatova, F. Robaut, M. Verdier, M. Yescas, F. Roch, C. Tassin, H. Landeghem, Microstructural and mechanical investigation of the near fusion boundary region in thermally aged 18MND5 / alloy 52 narrow-gap dissimilar metal weld, *Mater. Sci. & Eng. A* 788 (139592) (2020).
- [4] Z. Chen, Y. Lu, TEM observation of Martensite layer at the weld Interface of an A508III to Inconel 82 dissimilar metal weld joint, *Metall. Mater. Trans. A* 46A (2015) 5494–5498.
- [5] M. Ahonen, R. Mougnot, T. Sarikka, S. Lindqvist, Z. Que, U. Ehrnstén, I. Virkkunen, H. Hänninen, Effect of thermal ageing at 400°C on the microstructure of ferrite-austenite interface of nickel-base alloy narrow-gap dissimilar metal weld, *Metals* 10 (3) (2020) 421.
- [6] J. Parker, G. Stratford, Characterisation of microstructures in nickel based transition joints, *J. Mater. Sci.* 35 (2000) 4099–4107.
- [7] J. Hou, Q. Peng, Y. Takeda, J. Kuniya, T. Shoji, J. Wang, E.-H. Han, W. Ke, Microstructure and mechanical property of the fusion boundary region in an alloy 182-low alloy steel dissimilar weld joint, *J. Mater. Sci.* 45 (2010) 5332–5338.
- [8] P. Efsing, B. Forssgren, R. Kilian, Root cause failure analysis of defected J-groove welds in steam generator drainage nozzles, in: *Proceedings of the Twelfth International Conference on Environmental Degradation of Materials in Nuclear Power Systems-Water Reactors*, 2005.
- [9] A. Janssen, K. Norrgard, J. Lagerstrom, G. Embring, C. Jansson, P. Efsing, Structural assessment of defected nozzle to safe-end welds in Ringhals-3 and -4, in: *Proc. Fontevraud V Intl. Symp.*, 2000.
- [10] P. Efsing, J. Lagerström, Analysis of a defected dissimilar metal weld in a PWR power plant, in: *10th Int Conf Nucl Eng.*, 2002.
- [11] Z. Que, M. Lindroos, J. Lydman, N. Hytönen, S. Lindqvist, P. Efsing, P. Nevasmaa, P. Arffman, Brittle fracture initiation in decommissioned boiling water reactor pressure vessel head weld, *J. Nucl. Mater.* 569 (153925) (2022).
- [12] K. Choi, S. Yoo, S. Kim, T. Kim, J. Ham, J. Lee, J. Kim, Microstructural evolution and corrosion behaviour of thermally aged dissimilar metal welds of low-alloy steel and nickel-based alloy, *Corros. Sci.* 153 (2019) 138–149.
- [13] H. Wang, G. Wang, F. Xuan, C. Liu, S. Tu, Local mechanical properties of a dissimilar metal welded joint in nuclear power systems, *Mater. Sci. & Eng. A* 568 (2013) 108–117.
- [14] S. Yoo, K. Choi, C. Bahn, S. Ki, J. Kim, J. Kim, Effects of thermal aging on the microstructure of type-II boundaries in dissimilar metal weld joints, *J. Nucl. Mater.* 459 (2015) 5–12.
- [15] A. Blouin, S. Chapuliot, S. Marie, C. Niclaeys, J. Bergheau, Brittle fracture analysis of dissimilar metal welds, *Eng. Fract. Mech.* 131 (2014) 58–73.
- [16] J. Gao, J. Tan, M. Jiao, X. Wu, L. Tang, Y. Huang, Role of welding residual strain and ductility dip cracking on corrosion fatigue behavior of alloy 52/52M dissimilar metal weld in borated and lithiated high-temperature water, *J. Mater. Sci. Technol.* 42 (2020) 163–174.
- [17] J. Kim, K. Choi, C. Bahn, K. J.H, In situ Raman spectroscopic analysis of surface oxide films on Ni-base alloy/low alloy steel dissimilar metal weld interfaces in high-temperature water, *J. Nucl. Mater.* 449 (2014) 181–187.
- [18] H. Ming, J. Wang, E. Han, Comparative study of microstructure and properties of low-alloy-steel/nickel-based-alloy interfaces in dissimilar metal weld joints prepared by different GTAW methods, *Mater. Charact.* 139 (2018) 186–196.
- [19] P. Joly, M. Yescas, E. Keim, Fracture toughness in the ductile-brittle transition and thermal ageing behavior of decarburized heat affected zone of Alloy 52 dissimilar metal welds of nuclear components, in: *Proceedings of the ASME-2014 Pressure Vessel and Piping Conference*, Anaheim, California, USA, 2014.
- [20] R. Mougnot, Effect of Thermal Ageing on Alloys 690 and 52 in Pressurized Water Reactor Applications, Doctoral dissertation, Aalto University, 2017.
- [21] H. Wang, G. Wang, F. Xuan, S. Tu, Fracture mechanism of a dissimilar metal welded joint in nuclear power plant, *Eng. Fail. Anal.* 28 (2013) 134–148.
- [22] S. Lindqvist, Z. Que, P. Nevasmaa, N. Hytönen, The effect of thermal aging on fracture properties of a narrow-gap alloy 52 dissimilar metal weld, *Eng. Fract. Mech.* 281 (109056) (2023).
- [23] S. Lindqvist, N. Hytönen, L. Sirkiä, P. Arffman, J. Lydman, Y. Ge, P. Nevasmaa, Z. Que, Fracture in the Ductile-To-Brittle Transition Region of A Narrow-Gap Alloy 52 and Alloy 52 Dissimilar Metal Weld With Buttering, in: *ASME PVP2022–80690*, Las Vegas, USA, 2022.
- [24] N. Hytönen, Y. Ge, Z. Que, S. Lindqvist, P. Nevasmaa, I. Virkkunen, P. Efsing, Study of fusion boundary microstructure and local mismatch of SA508/Alloy 52 dissimilar metal weld, *J. Nucl. Mater.* (2023).
- [25] N. Hytönen, Y. Ge, Z. Que, S. Lindqvist, J. Lydman, U. Ehrnstén, P. Rautala, I. Virkkunen, P. Efsing, Effect of Microstructure on Mechanical Behavior of Ni-base Alloy Dissimilar Metal Welds, in: *The 20th International Conference on Environmental Degradation of Materials in Nuclear Power Systems-Water Reactor Meeting*, Colorado, USA, 2022.
- [26] L. Lutterotti, Maud: a Rietveld analysis program designed for the internet and experiment integration, *Acta Crystallogr. A: Found. Crystallogr.* 56 (s1) (2000) 54.
- [27] Y. Bagaryatskii, Veroyatnue mehanizm raspada martenseeta, *Dokl. Akad. Nauk SSSR* 73 (1950) 1161.
- [28] L. Zhang, B. Radigue, P. Todeschini, C. Domain, Y. Shen, P. Pareige, Investigation of solute segregation behavior using a correlative EBSD/TKD/APT methodology in a 16MND5 weld, *J. Nucl. Mater.* 523 (2019) 434–443.
- [29] M. Thuvander, J. Weidow, J. Angseryd, L. Falk, F. Liu, M. Sonestedt, K. Stiller, H. Andren, Quantitative atom probe analysis of carbides, *Ultramicroscopy* 111 (6) (2011).
- [30] S. Kou, *Welding Metallurgy*, 2nd edition, John Wiley & Sons, Inc., 2003.
- [31] N. Hytönen, Z. Que, S. Lindqvist, J. Lydman, Y. Ge, I. Virkkunen, U. Ehrnstén, P. Rautala, P. Efsing, B. Forssgren, Fusion boundary microstructure and fracture behaviour of a narrow-gap Alloy 52 dissimilar metal weld and an Alloy 52 dissimilar metal weld and an Alloy 52 Dissimilar Metal Weld with Buttering, in: *International Symposium Contribution of Materials Investigations and Operating Experience to LWRs' Safety, Performance and Reliability*, FONTEVRAUD 10, Avignon, France, 2022.
- [32] P. Nevasmaa, P. Holmström, P. Karjalainen-Roikonen, T. Sarikka, M. Ahonen, R. Mougnot, U. Ehrnstén, A. Brederholm, P. Aaltonen, H. Hänninen, Fracture mechanical characterisation of ferrite-austenite dissimilar metal welds (DMWs) for elevated temperature service in view of metallurgical mismatch, in: *International Conference on Life Management and Maintenance for Power Plants*, Helsinki, 2013.
- [33] K. Choi, J. Kim, B. Lee, C. Bahn, J. Kim, Effects of thermal aging on microstructures of low alloy steel-Ni base alloy dissimilar metal weld interfaces, *J. Nucl. Mater.* 441 (2013) 493–502.